Doctoral Dissertation

Bio-based polymer derived heteroatom doped carbons as efficient anode materials for metal-ion batteries

Kottisa Sumala Patnaik

Supervisor: Noriyoshi Matsumi

Division of Advanced Institute of Science and Technology

Japan Advanced Institute of Science and Technology

[Materials Science]

(September 2025)

Abstract

This doctoral thesis centers on the synthesis and application of heteroatom-doped hard carbons derived from bio-based polymers as anode materials for both lithium-ion and sodium-ion batteries.

Chapter 1: Introduction

Energy storage has become increasingly vital in today's world which is highly dependent on technology. Traditionally, fossil fuels have served as the primary energy source for transportation and various systems; however, concerns over resource depletion and environmental impact have accelerated the shift toward cleaner and more sustainable alternatives. In response, a range of energy storage technologies—including fuel cells, batteries, and capacitors—are being actively developed and improved. This chapter provides an overview of key energy storage devices, including capacitors, fuel cells, primary batteries, and rechargeable (secondary) batteries. Sodium-ion batteries, an emerging energy storage technology is also receiving increasing attention owing to the low cost and widespread availability of sodium. This chapter also outlines the fundamental components of batteries—cathode, anode, and electrolyte—with a focus on their roles in both lithium-ion and sodium-ion systems. Finally, the chapter introduces the material design strategies explored in this thesis, setting the foundation for the subsequent chapters.

Chapter 2: Bio-based poly(benzimidazole-co-amide) derived N, O co-doped carbons as fast-charging anodes for lithium-ion batteries

This chapter presents the synthesis and electrochemical evaluation of nitrogen and oxygen co-doped hard carbons (HCs) derived from bio-based copolymers,

specifically poly(benzimidazole-co-amide), as potential anode materials for lithium-ion batteries (LIBs). The study addresses the growing demand for LIBs that support fast charging and deliver high capacity, particularly for electric vehicle applications. To explore the effect of precursor composition on electrochemical performance, poly(benzimidazole-co-amide) copolymers were synthesized with varying ratios of benzimidazole to amide units—8.5:1.5, 7:3, and 5:5. These copolymers were then pyrolyzed under a nitrogen atmosphere to yield nitrogen and oxygen dual-doped hard carbons, referred to as PYPBIPA8.5-1.5, PYPBIPA7-3, and PYPBIPA5-5. The copolymers acted as single-source precursors for carbon, nitrogen, and oxygen, resulting in materials with nitrogen contents ranging from 12.1 to 8.0 atomic percent and oxygen contents between 11.8 and 25.0 atomic percent. Coin cells were fabricated using the obtained carbon materials as anodes, and rate capability tests were conducted to assess their performance. Among the three, PYPBIPA8.5-1.5 exhibited the best rate performance, especially under high current densities. Motivated by these results, extended cycling studies were carried out at a high current density of 4.0 A/g. Remarkably, PYPBIPA8.5-1.5 maintained a delithiation capacity of 135 mAh/g, compared to 100 mAh/g and 60 mAh/g for PYPBIPA7-3 and PYPBIPA5-5, respectively. It also showed excellent cycling stability, retaining 90% of its capacity even after 3000 cycles.

Chapter 3: Bio-based poly(benzothiazole) derived N, S co-doped carbons as fast-charging anodes for sodium-ion batteries

Sodium-ion batteries (SIBs) have gained attention as a promising alternative to lithium-ion batteries (LIBs) for next-generation energy storage, thanks to the abundance and low cost of sodium. However, enabling fast-charging in SIBs remains a key challenge, largely due to the sluggish diffusion kinetics of sodium ions. This

limitation often appears as a pronounced low-potential plateau in the charge-discharge profiles, which hampers high-rate performance. To overcome this, various strategies have been explored, with heteroatom doping emerging as a particularly effective approach. Nitrogen doping is well-known for enhancing electronic conductivity and promoting surface adsorption through pseudocapacitive mechanisms. Sulfur doping, especially relevant for SIB anodes, provides additional benefits due to its larger atomic radius, which increases interlayer spacing and allows for extra sodium-ion storage through non-faradaic interactions. In this study, a nitrogen and sulfur co-doped hard carbon material derived from the bio-based polymer polybenzothiazole is investigated as a potential anode for sodium-ion batteries. The hard carbon samples were synthesized via pyrolysis at two different temperatures to systematically assess the influence of structural and compositional variations on their fast-charging performance.

Chapter 4: Conclusions

This chapter presents a comprehensive summary of the key findings and discussions outlined in the preceding chapters. It revisits the main objectives of the thesis and highlights how each chapter contributed to addressing these goals. A concise overview of the topics explored throughout the study is provided, emphasizing the significance of the results in the context of the broader research field. Additionally, this chapter explores the potential future directions for research involving these materials, outlining possible improvements, extensions, and innovations. It also discusses the wide range of applications these materials could support across various industries, reflecting their promising potential in both current and emerging technologies.

Table of Contents

Preface

Global energy demand has increased significantly in recent decades, primarily due to rapid technological progress. Energy storage devices are essential in addressing this demand by enabling the storage and on-demand use of energy. Lithium-ion batteries have played a pivotal role in this space, thanks to their compact size and lightweight design, making them ideal for a wide range of applications. However, rising costs and limited availability of the raw materials used in lithium-ion batteries have spurred interest in alternative technologies. Sodium-ion batteries have emerged as promising candidates for future energy storage, as sodium is one of the most abundant elements. A key challenge for lithium as well as sodium-ion batteries is improving their fast-charging capability. While various carbon-based anodes have been explored for fast-charging applications, heteroatom-doped hard carbons remain relatively under-investigated. Doping hard carbons with heteroatoms can significantly alter both the morphology and elemental composition of the material, potentially enhancing their electrochemical performance. Motivated by this background, the author under the guidance of Prof. Noriyoshi Matsumi at Graduate School of Advanced Science and Technology, Japan Advanced Institute of Science and Technology started utilizing bio-based polymers for synthesizing heteroatom doped hard carbons. In this thesis titled "Bio-based polymer derived heteroatom doped carbons as efficient anode materials for metal-ion batteries", the author has presented her humble endeavors towards developing and understanding the utilization of heteroatom doped hard carbons obtained from bio-based polymers as anodes for lithium and sodium-ion batteries.

Kottisa Sumala Patnaik

Acknowledgement

This thesis, titled “Bio-based Polymer Derived Heteroatom Doped Carbons as Efficient Anode Materials for Metal-Ion Batteries,” was conducted under the guidance of Professor Noriyoshi Matsumi at the Graduate School of Advanced Science and Technology, Japan Advanced Institute of Science and Technology (JAIST). I express my deepest gratitude to Prof. Noriyoshi Matsumi for his unwavering support, insightful guidance, and encouragement throughout the course of this research. I am also profoundly grateful to Assistant Professor Bharat Srimitra for his valuable insights and scientific expertise, which significantly contributed to the quality and depth of this work. I convey my sincere gratitude to the members of the thesis review committee for their time, effort, and thoughtful evaluation of my thesis. I am truly thankful to Prof. Takuya Tsujiguchi of Kanazawa University for providing the opportunity to pursue my minor research under his supervision. I also extend my gratefulness to Prof. Toshiaki Taniike for reviewing my minor research thesis with care and consideration. I wish to express my heartfelt thankfulness to Technical Specialists Koichi Higashimine and Akio Miyazato, as well as to the entire staff of the Center for Nano Materials and Technology (CNMT), JAIST, for their indispensable technical support, without which this thesis would not have come to fruition. I remain deeply indebted to my parents, extended family, friends, and lab members for their constant encouragement, emotional support, and belief in my abilities throughout this journey. Above all, I dedicate this work to the almighty whose creation continues to inspire my curiosity.

Kottisa Sumala Patnaik

1. Introduction

1.1 Abstract

Energy storage plays a crucial role in today's world due to our increasing reliance on technology. While fossil fuel-based energy has long powered vehicles and most systems, the depletion of these resources and their significant environmental impact have prompted the search for cleaner, more sustainable alternatives. In response, a variety of energy storage technologies are being developed, including fuel cells, batteries, and capacitors. This chapter provides a brief introduction to several types of energy storage devices, such as capacitors, fuel cells, primary batteries, and secondary batteries. Additionally, emerging battery technologies like sodium-ion batteries are discussed, given their growing demand driven by the low cost and widespread availability of sodium. The chapter also offers an overview of key battery components—namely the cathode, anode, and electrolyte—examined in the context of both lithium-ion and sodium-ion batteries along with discussions on the design of materials reported in this thesis.

1.2 General introduction to energy sources

In recent years, there has been a noticeable surge in global energy demand—not only for industrial applications but also for everyday household use[1,2]. and the increasing dependence on digital technologies in daily life. As a result, a wide range of energy storage devices have been developed to cater to the diverse applications which can be broadly classified based on the type of stored energy, such as (i) mechanical energy storage (ii) chemical energy storage (iii) electrochemical energy storage (iv) electrostatic and electromagnetic energy storage and (v) thermal energy storage[3]. Chemical energy storage systems primarily function by converting the energy released from the breaking of chemical bonds. Common fuels such as coal, gasoline, natural gas, and hydrogen are typically transformed into heat and mechanical energy, which are then used to power vehicles and machinery. However, burning these chemical fuels can lead to environmental issues, such as air pollution and greenhouse gas emissions. Additionally, the depletion of fossil fuel resources is becoming an increasing concern. In light of these challenges, electrochemical energy storage systems present a more sustainable alternative. These systems store and produce electricity through chemical processes, which can then be used to power various vehicles and other systems. The details of these alternative electrochemical energy storage systems are outlined below, including fuel cells, capacitors, supercapacitors, and both primary and secondary batteries.

1.2.1 Fuel Cells

Fuel cells convert the chemical energy stored in fuels into electrical energy through controlled chemical reactions. Various fuels, such as hydrogen, natural gas, and methanol, can be used to produce electricity. Unlike batteries, fuel cells require a

continuous supply of both fuel and an oxidant to function[3]. A typical fuel cell generally consists of an anode, a cathode, and an electrolyte that facilitates the movement of ions between the electrodes while forcing electrons to flow through an external circuit—thereby generating electricity. The main components of a typical fuel cell as shown in Fig. 1 include:

(i) **Anode** – The negative electrode where oxidation of the fuel occurs.

(ii) **Cathode** – The positive electrode where reduction takes place.

(iii) **Electrolyte** – A medium that allows the flow of ions between the anode and cathode, while blocking the flow of electrons.

(iv) **Catalyst** – A substance that accelerates the chemical reactions at both the anode and cathode without being consumed in the process.

(v) **Separator** – A membrane or layer that physically separates the anode and cathode, preventing direct mixing of the reactants while still allowing ion flow.

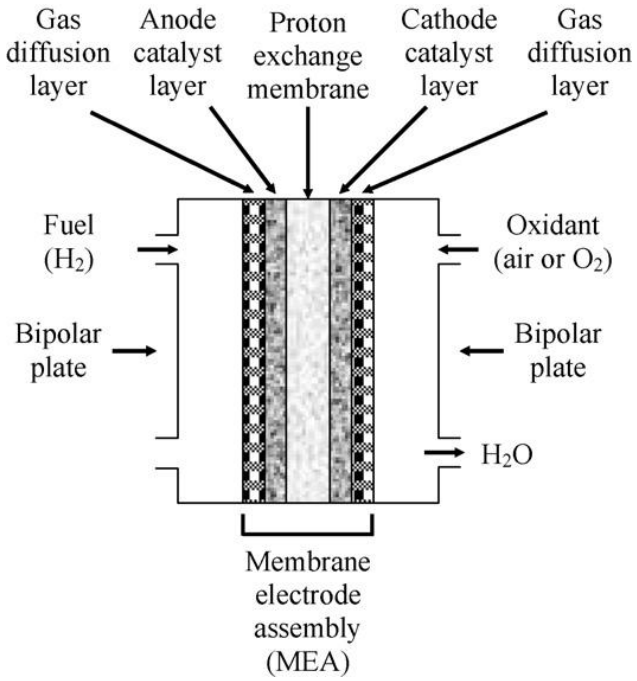

Figure 1: *Typical components of a PEMFC*[4]

Typically, a fuel cell works by oxidation of fuel at the anode which is facilitated by a platinum catalyst leading to release of electrons and ions. The hydrogen ions pass through the electrolyte to reach the cathode, while the electrons are forced to travel through an external circuit, generating an electric current[3].

Various types of fuel cells have their own unique characteristics they can be classified as-

(i) Polymer Electrolyte Membrane Fuel Cells (PEMFCs) use a solid polymer membrane as the electrolyte. Like other fuel cells, PEMFCs generate electricity through electrochemical reactions[4,5]. One of their key advantages is the ability to operate efficiently at relatively low temperatures (typically between 50–100°C)[5]. Additionally, their compact and lightweight design enables higher power density, making them particularly well-suited for mobile and portable applications such as electric vehicles and backup power systems.

(ii) Alkaline Fuel Cells (AFC) utilize a liquid alkaline solution such as potassium hydroxide as the electrolyte which allows for faster oxygen reduction reaction (ORR) kinetics. The energy barrier for ORR is lower in the presence of a basic medium than in an acidic medium leading to faster ORR kinetics in AFCs[6]. The alkaline environment also allows for usage of less expensive non-precious metals such as Ni, Ag as catalysts[7].

(iii) Solid Oxide Fuel Cells (SOFC) use solid ceramic as an electrolyte enabling them to operate at higher temperatures thus allowing the usage of various fuels including natural gas and biogas. The solid electrolyte makes it more mechanically robust, leak proof as weak as less sensitive to orientation[8].

(iv) **Phosphoric Acid Fuel Cell (PAFC)** uses phosphoric acid soaked in a porous matrix as the electrolyte. PAFC's are durable and can operate at moderate temperatures thus enabling their application in stationary power[9].

(v) **Molten Carbonate Fuel Cells (MCFC)** uses molten mixture of carbonate salt (such as lithium carbonate, potassium or sodium carbonate) as the electrolyte. MCFCs operate at higher temperatures allowing the use of non-precious metal catalysts[10].

1.2.2 Capacitors

Capacitors are electrostatic energy storage devices that store energy in the form of an electric field. They consist of two metal plates separated by a non-conductive material called a dielectric. When a capacitor is connected to a power source, electrons accumulate on one plate, making it negatively charged, while electrons are drawn away from the other plate, making it positively charged. This separation of charges creates an electric field across the dielectric[11]. As the capacitor charges, the voltage across its plates increases. Charging continues until the voltage across the capacitor matches the voltage of the power source—at this point, the capacitor is considered fully charged. When a load such as a light bulb is connected across the capacitor, the stored energy is released[11]. Electrons flow from the negatively charged plate, and an equal amount of positive charge flows from the other plate, allowing current to flow through the load and power the device.

1.2.3 Supercapacitors

Supercapacitors are similar to conventional capacitors, but instead of solid dielectric, they use a liquid or polymer electrolyte to store energy. This design allows supercapacitors to store 10 to 100 times more energy than traditional

capacitors. The porosity and surface area of the electrodes play a critical role in enhancing charge storage capacity, leading to higher power and energy density. Supercapacitors are generally classified into three types[12]:

(i) Electric Double-Layer Capacitors (EDLCs):

These involve non-faradaic charge storage, where charges interact electrostatically with carbon-based electrode materials without any chemical reaction.

(ii) Pseudocapacitors:

These rely on faradaic reactions, where charge storage involves redox (electron transfer) processes with materials like metal oxides, sulfides, selenides, and conducting polymers.

(iii) Hybrid Capacitors:

These combine both mechanisms, with faradaic reactions occurring on one electrode and non-faradaic interactions on the other, offering a balance between energy and power density.

1.2.4 Batteries

Batteries are among the most used energy storage systems. They are generally classified into two main types: primary batteries and secondary batteries. Primary batteries are non-rechargeable and are designed for single-use applications while secondary batteries, on the other hand, are rechargeable and can undergo multiple charge and discharge cycles, making them suitable for long-term and repeated use.

(i) Primary batteries

One of the examples of a primary battery is a dry cell which is a zinc-carbon battery in which the positive electrode is a rod made of carbon surrounded by a paste of manganese (IV) oxide, zinc chloride, ammonium chloride, carbon powder and a small amount of water while zinc serves as the container as well as the negative electrode. At the anode, zinc undergoes oxidation as shown below[13];

$$Zn(s) = Zn^{2+}(aq) + 2e^- \qquad E°_{Zn^{2+}/Zn} = -0.7618\ V$$

Whereas at the cathode a series of reactions occur;

$$2MnO_2(s) + 2NH_4Cl(aq) + 2e^- = Mn_2O_3(s) + 2NH_3(aq) + H_2O(l) + 2Cl^-$$

The overall reaction for the dry cell can be written as,

$$2MnO_2(s) + 2NH_4Cl(aq) + Zn(s) \rightarrow Zn^{2+}(aq) + Mn_2O_3(s) + 2NH_3(aq) + H_2O(l) + 2Cl^-$$

with an overall cell potential of 1.5V regardless of the size of the battery whether it is D, C, A, AA or AAA though larger batteries can deliver current for a longer time. As the battery discharges or ages, the electrolyte (ammonium chloride or zinc chloride) can leak which being corrosive and can damage electronic devices. Following this, alkaline batteries were developed wherein the NH_4Cl was replaced with KOH and zinc metal case was replaced with powdered zinc.

Hence the reaction at anode is[14],

$$Zn(s) + 2OH^-(aq) = ZnO(s) + H_2O(l) + 2e^-$$

While the reaction at cathode is,

$$2MnO_2(s) + H_2O(l) + 2e^- = Mn_2O_3(s) + 2OH^-(aq)$$

And overall,

$$Zn(s) + 2MnO_2(s) \rightarrow ZnO(s) + Mn_2O_3(s)$$

(ii) Secondary batteries

Lead acid and Nickel-Cadmium Batteries

These are rechargeable batteries which can be used in devices such as smartphones, electronics and automobiles. Lead acid batteries are the first type of rechargeable batteries ever invented in 1859. It contains lead anode, and a grid of lead packed with lead oxide (PbO_2) as cathode and 38% of sulphuric acid as electrolyte[15].

Anode: $Pb(s) + SO_4^{2-}(aq) = PbSO_4\ (s) + 2e^-$

Cathode: $PbO_2(s) + SO_4^{2-}(aq) + 4H^+(aq) + 2e^- = PbSO_4\ (s) + 2H_2O\ (l)$

Overall reaction: $Pb(s) + PbO_2(s) + 2H_2SO_4(aq) \rightarrow 2PbSO_4(s) + 2H_2O\ (l)$

Lead-acid batteries being cheaper to manufacture make them accessible to a large market. Lead-acid batteries can deliver higher power densities due to simplicity of the chemical reactions which can enable quick charge and discharge. The high conductivity of lead and lead dioxide (PbO_2) enables faster electron movement. Lead is a good conductor, so it allows the battery to discharge quickly without significant internal resistance, leading to higher power output. Lead-acid batteries use porous lead electrodes, which increases the overall size and weight of the battery[15]. Additionally, another significant drawback is the need for regular maintenance, specifically the refilling of water to maintain the electrolyte balance. Following this, various other rechargeable batteries were developed, of which nickel-cadmium batteries have gained significant interest owing to their high durability, ability to provide sudden burst of power as well as reliability in wide range of temperatures. However, the main issue with Ni-Cd batteries is the memory

effect. If the battery is not fully discharged before recharging, only a portion of the electrode material is utilized. Meanwhile, the remaining cadmium metal begins to form large crystals, which reduces the surface area available for reactions and increases the internal resistance of the battery[16]. Apart from lead-acid and nickel-cadmium batteries, a variety of rechargeable batteries such as nickel-metal hydride[17](NiMH), nickel-iron (Ni-Fe)[18] and LIBs have been developed. The characteristic features of these batteries are listed below in Table 1.

Table 1*: Comparison of various secondary batteries based on energy density, weight, memory effect, lifespan, and drawbacks*[15,17]

Battery type	Energy Density	Weight	Memory Effect	Lifespan	Other drawbacks
Ni-Cd[16]	Low	Heavy	Yes	Medium	Environmentally hazard
NiMH[17]	Medium	Medium	Minimal	Medium	Lower cell voltage
Lead-Acid[15]	Very low	Very heavy	No	Low	Requires maintenance
Ni-Fe[18]	Very low	Very heavy	No	Very long	Slow charge, gassing
LIBs[19]	**High**	**Light**	No	**High**	Uneven geographic distribution of lithium metal

Lithium-ion batteries

In today's digital age, the demand for portable power solutions is at an all-time high due to our increasing reliance on technology. In recent years, the need for portable power systems has grown rapidly, driven by rising energy demands across a wide spectrum—from household devices to industrial applications and even large-scale systems like aircraft. The pursuit of higher energy density with minimal battery weight has long driven the search for alternative energy sources- a quest that found a breakthrough with the invention of LIBs[20]. Among all the elements used in rechargeable batteries, lithium stood out due to its unique properties—it is the lightest metal, has the highest electrochemical potential, and delivers the highest voltage. These characteristics sparked significant interest in the development of LIBs. This interest can be traced back to 1958, marked by early advancements and

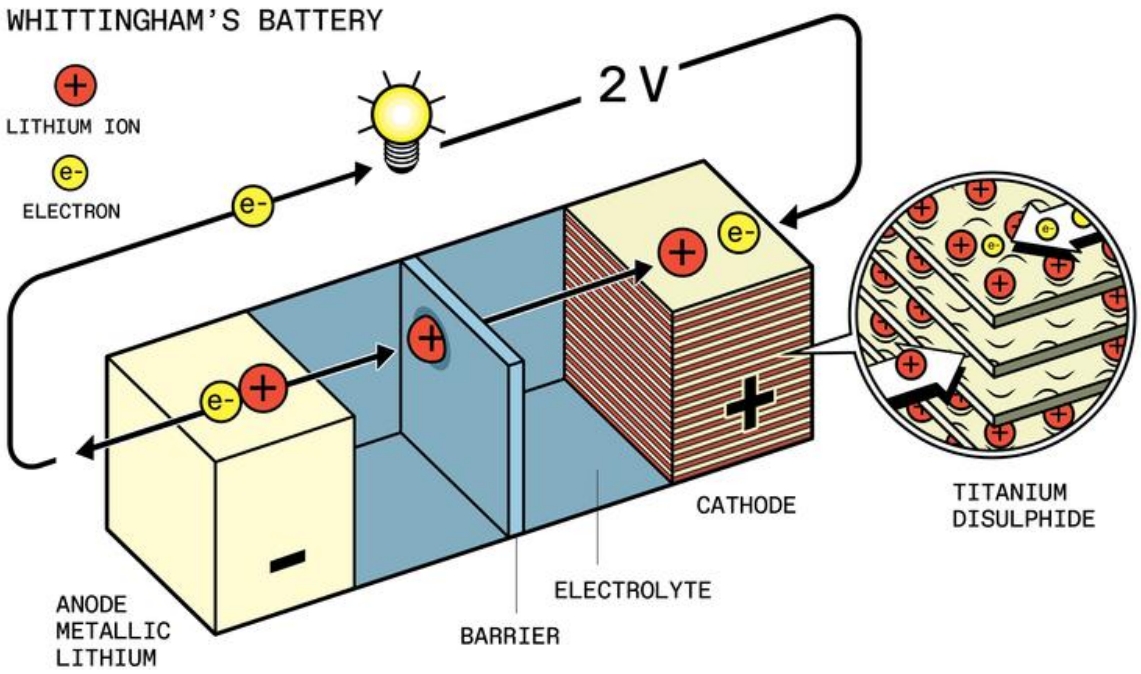

Figure 2: *Battery design of Whittingham's battery*[81]

commercialization of battery systems such as lithium/sulfur dioxide, lithium-thionyl chloride, and lithium-manganese[21].

Further, research demonstrated that solid-state materials could support rapid ion conduction, allowing alkali metal ions to move swiftly through electronically conductive lattices with transition metal atoms in mixed valence states. Building on these insights, Professor Stanley Whittingham developed one of the first rechargeable lithium batteries shown in Fig. 2, utilizing metallic lithium as the positive electrode and a liquid electrolyte containing lithium ions[22]. The first cells appeared when Exxon and Moli Energy first commercialized the Li/TiS_2 and Li/MoS_2 systems with an astonishing 2.4V compared to the state-of-the-art Ni-Cd batteries with a max of 1.3V[20]. However, all the systems researched by Prof. Whittingham utilized metallic lithium anodes thus limiting the commercial application of these batteries. After extensive research, high-voltage metal oxides became widely

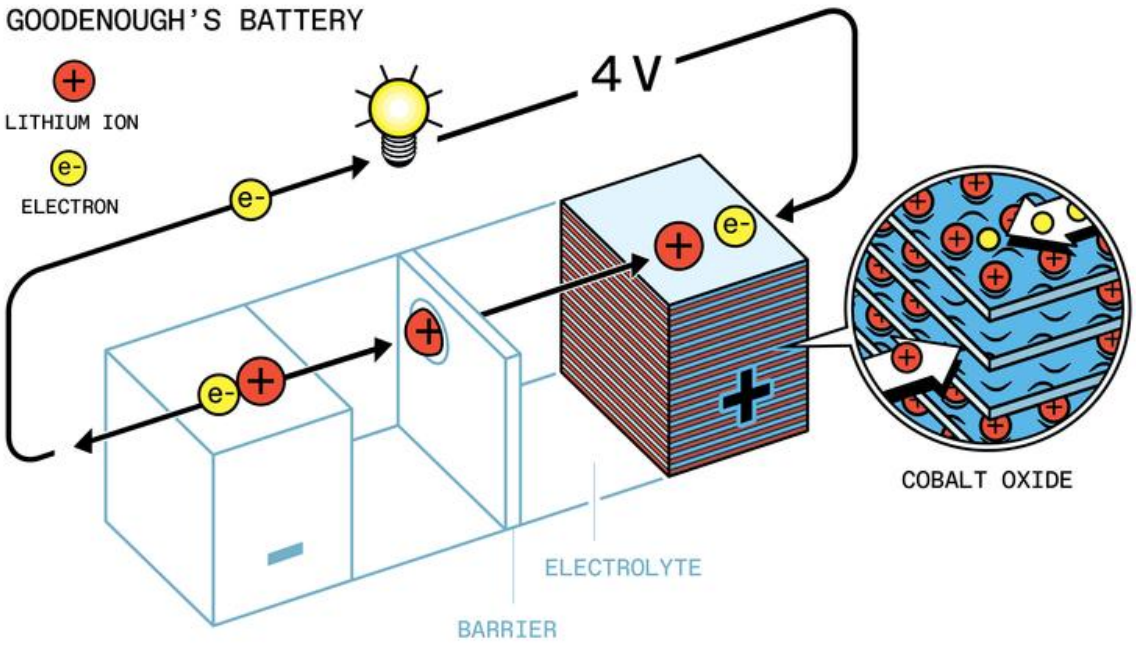

Figure 3: *Battery design of Goodenough's battery*[81]

adopted as cathode materials in commercial LIBs. Around this time, lithium-ion cells were being tested with two insertion electrodes, enabling lithium ions to shuttle back and forth between them. In 1980, Professor John B. Goodenough significantly improved upon Professor M. Stanley Whittingham's original design by replacing titanium disulfide (TiS_2) with lithium cobalt oxide ($LiCoO_2$) as the cathode as shown in Fig. 3. This substitution nearly doubled the battery's voltage, paving the way for significantly higher energy densities. In the following years, attention turned toward the development of a suitable negative electrode. Akira Yoshino, who had been working with polyacetylene, combined his findings with Goodenough's cathode design. He initially constructed a battery using $LiCoO_2$ as the cathode and polyacetylene as the anode. However, this was later replaced with petroleum coke as shown in Fig. 4, a more stable carbon-based material, to enhance safety and performance. This refined prototype was developed at Asahi Kasei, but it was Sony

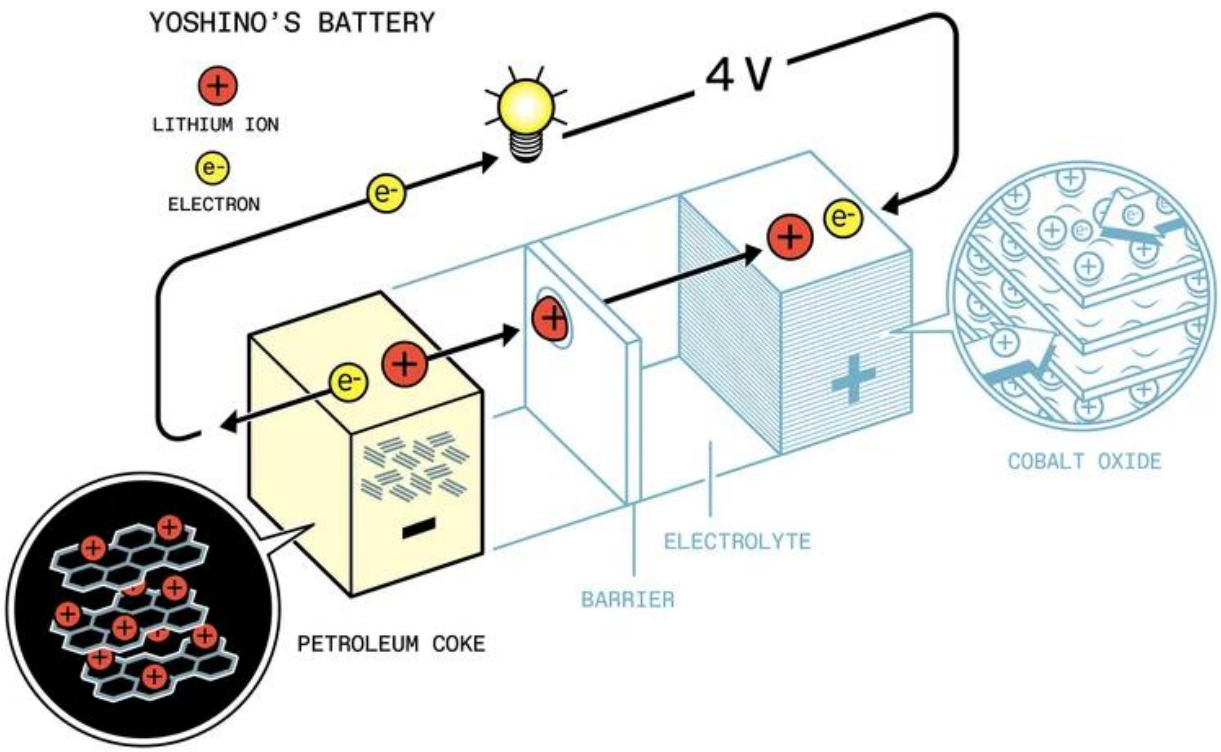

Figure 4: *Battery design of Yoshino's battery*[81]

that first commercialized the technology in the early 1990s—introducing lithium-ion batteries to the consumer market via their handheld camcorders[21].

Working mechanism of a lithium-ion battery

The working mechanism of LIBs relies on the intercalation and deintercalation of lithium ions. In a typical LIB, the cathode—usually composed of lithium transition metal oxides—serves as the lithium source. Commercial LIBs commonly use graphite as the active material in the anode. During charging, lithium ions migrate from the cathode to the anode, where they are intercalated between the graphite layers. The mechanism of charging using graphite as anode and $LiCoO_2$ as cathode can be written as[1],

At the cathode,

$$LiCoO_2 = CoO_2 + Li^+ + e^-$$

At the anode,

$$C_6 + Li^+ + e^- = LiC_6$$

Overall reaction

$$LiCoO_2 + C_6 \rightleftharpoons LiC_6 + CoO_2$$

Sodium-ion batteries

Although LIBs have been widely adopted in portable electronics and industrial applications, their rapid and large-scale use has raised growing concerns over the depletion and uneven distribution of lithium resources[23]. While the short-term impact may be minimal, the long-term consequences of diminishing lithium reserves are becoming increasingly significant. In addition to lithium, the limited

and geographically concentrated supply of cobalt presents another major challenge for the sustainable development of LIB technology. Cobalt's high price further exacerbates market instability[24,25]. In response to these issues, SIBs have emerged as a promising alternative to LIBs. SIBs share a similar working principle but benefit from the widespread abundance and low cost of sodium, which can be easily extracted from commonly available minerals. Moreover, SIBs offer additional economic advantages: key cathode materials often include iron—such as in iron phosphate—and aluminum foil is used in place of copper foil, contributing to a significant reduction in overall production costs[23]. Owing to the resource abundance and widespread availability, low cost, and non-toxicity of these electrode elements, SIBs are being considered for future applications especially those concerning large-scale battery applications. However, since the ionic radius (0.76Å for Na^+ vs the 1.02 Å for Li^+) as well as the electrochemical potential (2.71V vs SHE for Na^+ compared to 3.04V vs SHE for Li^+) acts as a barrier for direct translation of technology from LIBs to SIBs[26]. Especially, the larger ion size of Na^+ compared to Li^+, resents a much bigger challenge for direct translation of technology from LIBs to SIBs.

Working mechanism of a sodium-ion battery

The working mechanisms of LIBs and SIBs are broadly similar, involving the reversible intercalation of alkali metal ions between electrodes during charge and discharge cycles. However, the electrochemical interactions of lithium (Li), sodium (Na), and potassium (K) with graphite vary significantly. In SIBs, graphite is not a suitable anode material because it accommodates only a minimal amount of sodium[27]. This is due to the unstable formation of sodium-graphite intercalation

compounds (Na-GICs), which contrasts with the stable and efficient Li-GICs and K-GICs. The underlying reason lies in the nature of the bonding—Li forms non-negligible covalent bonds with graphite, while K forms strong ionic bonds, both of which are favorable than the weak interaction of Na with graphite[26]. As a result, hard carbons (HCs)—which are disordered, non-graphitizable forms of carbon—are employed as anode materials in SIBs. These materials provide larger interlayer spacing and a more amorphous structure, facilitating the storage of sodium ions through a combination of intercalation and pore filling[28]. Sodium-ion transport involves the migration of Na^+ ions from the cathode to the anode through the electrolyte during charging, followed by their intercalation into the HC anode structure. A typical charging mechanism using $NaFePO_4$ as the cathode and hard carbon as the anode can be represented as[26]:

At the cathode,

$$NaFePO_4 = FePO_4 + Na^+ + e^-$$

At the anode,

$$C + Na^+ + e^- = NaC_x$$

(where C represents hard carbon, and x depends on the material structure)

Overall reaction

$$NaFePO_4 + C \rightleftharpoons FePO_4 + NaC_x$$

The following sections will briefly describe the typical components of a battery such as,

1.3 Components of a battery

1.3.1 Cathode

Lithium-ion batteries: A cathode has more positive potential than the anode and hence is used as the positive electrode in the battery. The commercial LIBs utilize transition metal oxides containing lithium as cathodes. The energy density of a battery is generally increased by increasing the higher potential limit of the cathode as the energy density depends directly on the operating voltage window[29]. The present-day cathodes can be classified into three different types such as (i) layered oxides (ii) spinel oxides and (iii) polyanion oxides. A comparison table for the three types of cathodes is shown below in Table 2[30].

***Table 2**: Comparison of morphological and electrochemical features of different types of cathodes of LIBs[29]*

Features	Layered Oxides	Spinel Oxides	Polyanion oxides
Crystal Structure	Layered	Cubic spinel	Olivine
Li-ion diffusion	2D (in-plane diffusion)	3D (isotropic diffusion)	1D (limited by tunnel structure)
Energy Density	High	Moderate	Moderate
Voltage Range	~ 3.6-4.2V	~ 4.0V	~ 3.2-3.6V
Cost	Co/Ni expensive	Medium	Low
Example	$LiCoO_2$	$LiMn_2O_4$	$LiFePO_4$

Sodium-ion batteries: When selecting cathode materials for SIBs, several key characteristics must be considered to ensure optimal performance. Some of the important features to consider are high specific capacity, a higher redox potential, structural stability during repeated cycling, fast Na^+ diffusion kinetics, electronic conductivity, abundance and environmental friendliness of constituent elements[31]. The redox potential of the transition metal in the cathode plays a critical role. It directly influences the output voltage of the battery. A comparison table for the three types of cathodes is shown below in Table 3.

Table 3: *Comparison of morphological and electrochemical features of different types of cathodes of SIBs*[32]

Features	**Layered Oxides**	**Spinel Oxides**	**Polyanion oxides**	**Prussian Blue Analogues**
Crystal Structure	Layered	Cubic Spinel	Olivine/ NASICON	Open Framework
Na-ion diffusion	2D (in-plane diffusion)	3D (isotropic diffusion)	1D (tunnel) or 3D (NASICON)	3D (open framework)
Energy Density	High	Moderate	Moderate	Moderate
Voltage Range	~3.0 to 3.8 V	~3.8 to 4.1 V	~3.2 to 3.4 V	~3.2 to 3.4 V
Cost	Medium to high	Medium	Low	Low
Example	$NaNi_{1/3}Mn_{1/3}Fe_{1/3}O_2$	$NaMn_2O_4$	$NaFePO_4$	$NaFe[Fe(CN)_6]$

For SIBs, ideal cathode materials should operate within a voltage window of 2.5 to 4.2 V vs. Na^+/Na, balancing energy density with electrolyte stability. Transition metals such as Fe, Mn, Ni, Co, V, and Cr are commonly used, where each influences the redox behavior and structural stability of the cathode in a different way[31]. Such as the Fe^{3+}/Fe^{2+} offers good stability and low cost, while Ni^{3+}/Ni^{2+} or Co^{3+}/Co^{2+} pair contributes to a higher voltage but often at a higher cost and lower sustainability[33]. Currently available cathode materials for SIBs include layered transition metal oxides (e.g., $NaNiMnFeO_2$), polyanionic compounds (e.g., $NaFePO_4$, $Na_3V_2(PO_4)_3$), and Prussian Blue analogues (e.g., $NaFe[Fe(CN)_6]$). Despite their promise, each category faces challenges such as structural degradation in layered oxides due to phase transitions, low electronic conductivity in polyanionic compounds, and water content issues in Prussian Blue analogues. These challenges can be addressed through strategies like doping, surface coating, nano structuring, carbon composites, and moisture-controlled synthesis to improve conductivity, structural integrity, and stability. Currently available cathode materials for SIBs include layered transition metal oxides (e.g., $NaNiMnFeO_2$), polyanionic compounds (e.g., $NaFePO_4$, $Na_3V_2(PO_4)_3$), and Prussian Blue analogues (e.g., $NaFe[Fe(CN)_6]$)[34].

1.3.2 Electrolyte

An electrolyte allows the transfer of ions between anode and cathode within the battery. Currently, a variety of electrolytes such as liquid electrolytes, all-solid-state electrolytes, and gel-type polymer electrolytes are under research. Some of the important features of an electrolyte are its high ionic conductivity, thermal and chemical stability, a wide electrochemical potential window, low reactivity with both the anode and cathode materials and excellent safety characteristics[35].

Lithium-ion batteries: Typically, the electrolyte consists of a lithium salt such as $LiPF_6$ dissolved in a mixture of organic carbonate solvents like ethylene carbonate (EC), dimethyl carbonate (DMC), and diethyl carbonate (DEC). These electrolytes offer high ionic conductivity (10^{-3} S/cm), low viscosity, and good electrochemical stability within the operational voltage range (0 to 4.5 V)[36]. However, conventional LIB electrolytes are flammable and chemically reactive, posing safety risks, especially at elevated temperatures or in the event of mechanical failure.

Electrolytes can be classified as (i) liquid electrolytes (ii) solid electrolytes and (iii) ionic liquids. A comparison of these electrolytes is shown in Table 4,

***Table 4**: Comparison of features of different types of electrolytes in LIBs[37]*

Features	Liquid Electrolyte	Solid electrolyte	Ionic liquids
State	liquid	solid	liquid (highly viscous)
Ionic Conductivity	10^{-3} – 10^{-2} S/cm	10^{-5} – 10^{-3} S/cm	10^{-4} – 10^{-3} S/cm
Temperature stability	Limited (Risk at high temps)	Excellent	Excellent (>100°C)
Electrochemical stability	Moderate approx. 4.2–4.5 V	High (can exceed 5V)	Very high (Up to 5-6 V)
Safety	Low (flammable)	High (non-flammable)	High (non-flammable)
Ease of manufacture	Easy	Difficult	Moderate

Sodium-ion batteries: The most commonly used electrolytes in SIBs are liquid based systems containing sodium salts dissolved in organic solvents. The commonly used salts include sodium hexafluorophosphate ($NaPF_6$)[38], sodium perchlorate ($NaClO_4$), and sodium bis(fluorosulfonyl)imide (NaFSI). These salts are typically dissolved in carbonate solvents such as ethylene carbonate (EC), propylene carbonate (PC), dimethyl carbonate (DMC), and diethyl carbonate (DEC), often used in binary or ternary mixtures to optimize performance[39]. The electrolytes used for

SIBs can be classified as (i) liquid electrolytes (ii) solid electrolytes and (iii) ionic liquids. A comparison of these electrolytes is shown in Table 5.

***Table 5**: Comparison of different types of electrolytes for SIBs[39]*

Features	Liquid Electrolyte	Solid electrolyte	Ionic liquids
State	liquid	solid	liquid (highly viscous)
Ionic Conductivity	High (~10^{-3} S/cm)	10^{-4} – 10^{-2} S/cm	10^{-4} – 10^{-2} S/cm
Temperature stability	Moderate (flammable, degrades at >60 °C)	Excellent (can tolerate >1000°C)	Excellent (stable up to ~300°C)
Electrochemical stability	~ 3.5-4.5 V	Wide (can exceed 5V)	Wide
Safety	Low (flammable)	High (non-flammable)	High (non-flammable)
Ease of manufacture	Easy	Difficult	Moderate

1.3.3 Separator

A separator is generally a porous material that separates cathode from anode in the battery and allows flow of ions while blocking the flow of electrons. A few examples include polyethylene, polypropylene etc. In addition to the conventional polyolefin-based separators (such as polyethylene (PE) and polypropylene (PP), glass fiber membranes are widely used as separators in SIBs. Since GF based separators offer high thermal stability, excellent electrolyte wettability and mechanical robustness, they are highly suitable for SIBs.

1.3.4 Anode

Lithium-ion batteries: The anode is the electrode where oxidation takes place, releasing electrons to the external circuit. Lithium metal has long been regarded as one of the most promising anode materials for rechargeable batteries, owing to its extremely low anode potential of –3.045 V vs SHE (Standard Hydrogen Electrode) and an exceptionally high specific capacity of 3860 mAh/g[1]. It was widely used as the anode in primary lithium cells for more than two decades. However, its high reactivity with organic electrolytes presented significant challenges, including the formation of a non-uniform passivation layer and continuous lithium deposition and dissolution, which encourage the growth of dendrites—needle-like structures that can cause short circuits and pose serious safety risks[40]. While lithium metal remains the ultimate goal in battery research, alternative anode materials have been explored. In the late 1980s, researchers discovered that certain carbon-based materials could intercalate lithium ions, offering similar negative potential, reduced reactivity, and good cycling stability[41]. These carbon anodes paved the way for the development of the “rocking-chair” mechanism and have since become the

standard in commercial LIBs[42,43]. The promising potential of LIBs for a wide range of applications has driven extensive research into developing and optimizing various anode materials. Over time, researchers have explored different classes of materials to enhance performance, safety, and longevity.

Sodium-ion batteries: In the case of SIBs, their early development focused on graphite which has been commercially successful in LIBs. However, graphite showed poor sodium storage capability due to the difficulty of sodium-ion intercalation as discussed in previous section. Hard carbon emerged as a breakthrough which could accommodate Na^+-ions due to the disordered structure of the hard carbon alongside its wider interlayer spacing[44]. HCs remain as one of the most researched anode materials for SIBs offering a high capacity of approx. 300 to 350 mAh/g[45], good cycling stability and low operational potential wrt. Na/Na^+.

Currently, the anodic materials used in LIBs or SIBs can be broadly categorized into the following types:

a) Conversion-type anodes

b) Alloy-type anodes

c) Intercalation-type anodes

(i) Conversion Type Anodes:

Lithium-ion batteries: This class of anodes undergo conversion reactions with ions, forming metallic compounds and leading to the generation of new phases during cycling. Common examples include transition metal oxides such as Fe_2O_3, Fe_3O_4, CoO, Co_3O_4, and TiO_2[46]. These anodes offer high theoretical capacities, typically ranging from 500 to 1000 mAh/g[46]. However, they generally experience significant

volumetric changes during sodiation and de-sodiation processes. As a result, the cycling stability of these anodes is often moderate, largely due to the mechanical stress from repeated expansion and contraction. Additionally, these materials tend to exhibit low initial coulombic efficiency (ICE), because a substantial amount of ions is irreversibly consumed during the first charge cycle. Lithium-ion storage in these types of anodes (particularly metal oxides) occurs by mechanism as following[47],

$$MO + Li + 2e^- = Li_2O + M \ (M = Fe_2, Fe_3, Co, Co_3, Mn, Mn_3 \text{ etc.})$$

Sodium-ion batteries: Conversion-type anodes in SIBs operate through a mechanism similar to LIBs, where Na^+ ions react with the anode material to form metallic compounds, involving the breaking and reformation of chemical bonds during the sodiation and de-sodiation processes[48]. Common examples of conversion-type materials include transition metal oxides such as Fe_2O_3[49], Co_3O_4[50], NiO, metal sulfides like MoS_2, and metal phosphides such as FeP and CoP[51]. Similar to LIBs, these anodes experience significant volume changes during cycling, which can cause mechanical degradation, moderate cycling stability, and low initial coulombic efficiency (ICE), primarily due to irreversible reactions and the consumption of sodium ions during the first sodiation cycle[48].

(ii) Alloy Type Anodes:

Lithium-ion batteries: Alloy type anodes are especially attractive for their high theoretical specific capacities. These mainly involving elements from group IVA and VA i.e. Sn, Sb, Bi and Si, Ge[52] respectively deliver high specific capacities by forming Li_nM compounds (M represents metal) wherein n has a value greater

than one. The alloy type anodes generally operate in a voltage of 0.3-0.6V[53] vs Li/Li^+. Since many cathode materials used in LIBs have operating voltages that align well with the 0.3-0.6 V range, balanced cell potentials and efficient energy transfer can be obtained in full cells. However, the limited intrinsic conductivity of silicon, which is approximately 1.56×10^{-3} Scm^{-2}, along with challenges like continuous fracturing and pulverization of silicon particles caused by significant volume changes during cycling, hinder the long cycling performance of silicon-

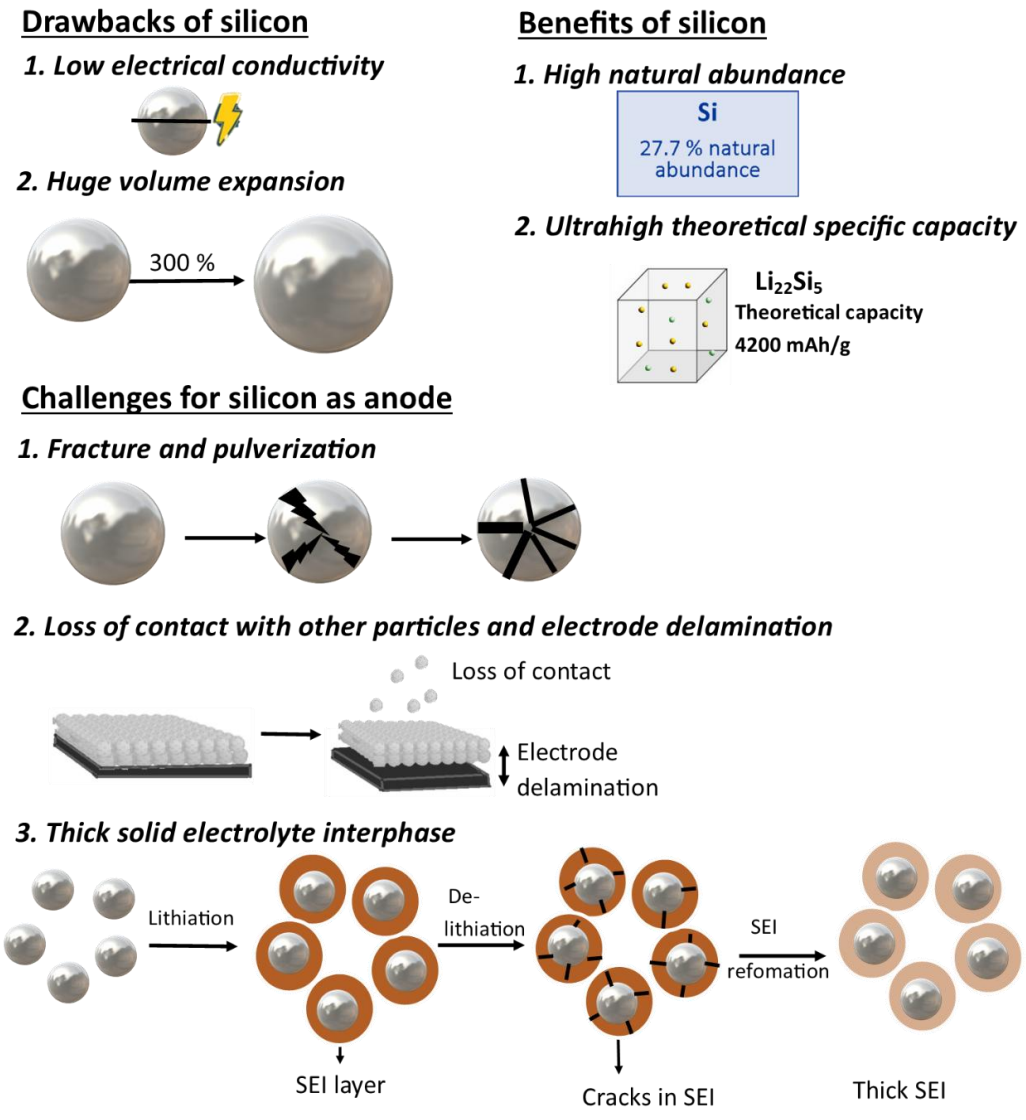

***Figure 5**: Challenges of using silicon as anode in LIBs[65]*

based anodes[54]. A vast majority of studies have identified $Li_{15}Si_4$ as the most highly lithiated phase at room temperature. In the $Li_{15}Si_4$ structure, all the Si atoms occupy the crystallographic sites with each Si atom surrounded by 12Li atoms between 2.61 to 2.87 Å[55]. The insertion of Li into Si breaks the Si-Si bonds. This in turn leads to a huge increase in the crystal volume i.e. 20 Å/Si atom in crystalline Si to 76 Å/Si in $Li_{15}Si_4$ resulting in a volume expansion of ~280 %[56]. The $Li_{15}Si_4$ sets a maximum deliverable capacity of 3578 mAh/g for Si[57]. However, the repeated expansion and contraction of silicon (Si) particles during lithiation and delithiation processes generate significant mechanical stress, leading to particle pulverization and electrode swelling. This swelling can result in electrode cracking, peeling, and loss of electrical contact within the Si particles, as well as detachment from the current copper collector, leading to the formation of nonactive Si and reduced electrical conductivity as shown in Fig. 5. Additionally, the unstable SEI poses another challenge for practical Si anode applications. Due to particle pulverization, fresh Si surfaces are exposed to the electrolyte in each cycle, leading to the formation of a new SEI layer and eventually resulting in a thick SEI film[58]. The thick SEI film causes excessive consumption of Li-ions, poor contact between Si particles, and increased impedance for diffusion of Li-ions.

Sodium-ion batteries: Alloy-type anodes in SIBs involve the formation of Na-rich alloys during the sodiation process. Elements such as tin (Sn), antimony (Sb), bismuth (Bi), phosphorus (P), and lead (Pb) are widely explored due to their ability to form stable sodium alloys like $Na_{15}Sn_4$, Na_3Sb, and Na_3P[59]. These anodes exhibit high theoretical capacities, often exceeding 400–1000 mAh/g, significantly outperforming typical intercalation-type anodes[60]. However, a major challenge associated with alloy-type anodes is the extensive volume expansion—up to

400%—which leads to particle cracking and electrode delamination during repeated cycling. Although strategies such as nanostructuring, composite formation with carbon materials[61], and the design of yolk-shell structures[62] have been developed to mitigate these issues, many challenges remain to be fully addressed for their practical application.

(iii) Intercalation Type Anodes:

These types of anodes are mainly made up of materials where the ions can insert themselves into the structure of the anode material without causing changes to its crystal structure. The host shows low to moderate volume change of <10 % as a result of which these materials are extremely stable over many charge-discharge cycles. They are highly reversible and stable for energy storage[41]. They exhibit high initial coulombic efficiency (~80–90%). Carbonaceous anodes and titanium-based anodes are the most common intercalation type of anodes.

In the case of SIBs as well, the intercalation-based anodes function by inserting Na^+-ions into the layered structure of HCs. HCs were utilized as negative electrodes in SIBs and various storage mechanisms such as insertion of Na^+-ions between the layers, pore filling, defect adsorption as well as adsorption on the layers have been identified. Other intercalation-based anodes used for SIBs includes titanium-based oxides[63] such as $Na_2Ti_3O_7$ and TiO_2, which provide better structural stability however operate at higher potentials such as ~0.3 to 0.8 V vs Na/Na^+ thus improving the safety and reducing the risk of sodium metal plating at the cost of low stability and low ICE.

(a) Graphite

Lithium-ion batteries: Although various carbon allotropes—ranging from crystalline forms to highly disordered structures—have been investigated as anode materials for LIBs, graphite remains the most widely adopted. This preference is attributed to its high specific capacity of 372 mAh/g, low irreversible capacity, and excellent cycling stability. Among the diverse forms of carbon, graphite and disordered carbon are the most utilized in practical LIB applications. Graphite's crystal structure is composed of sp^2-hybridized carbon atoms

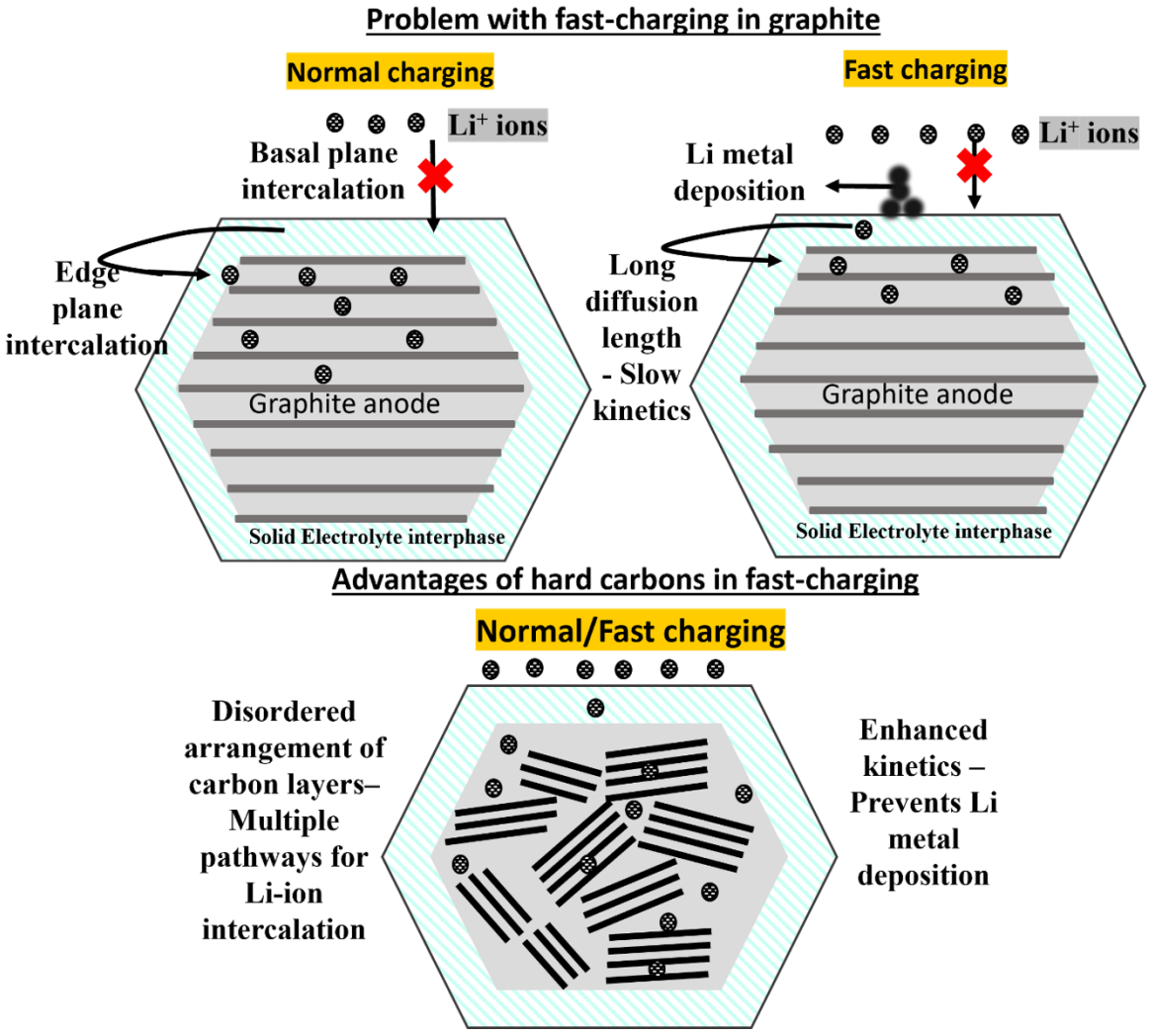

***Figure 6**: Illustration of the challenges associated with fast charging in graphite*

interconnected through strong covalent bonds[64]. Each carbon atom bonds with three neighboring carbon atoms in a planar hexagonal lattice, while π-bonds overlap parallel to the plane, enabling electron delocalization within the graphitic layers. These layers stack via van der Waals interactions between the π orbitals, forming the well-known layered structure of graphite. Thus, the structure of graphite consists of two types of characteristic surfaces such as normal and those parallel to the c-axis. However, due to the anisotropic nature of graphite, lithium-ion intercalation occurs primarily through the edge planes, rather than the basal planes, as depicted in Fig. 6. A schematic illustration of lithium-ion intercalation in graphite is shown in Fig. 7[65]. The intercalation process involves several key steps:

(i) Diffusion of solvated Li-ions through the electrolyte

(ii) Desolvation, where the solvation shell is stripped from the Li-ions

(iii) Diffusion of desolvated Li-ions through the solid electrolyte interphase (SEI)

(iv) Electron transport within the anode and across the anode–current collector interface

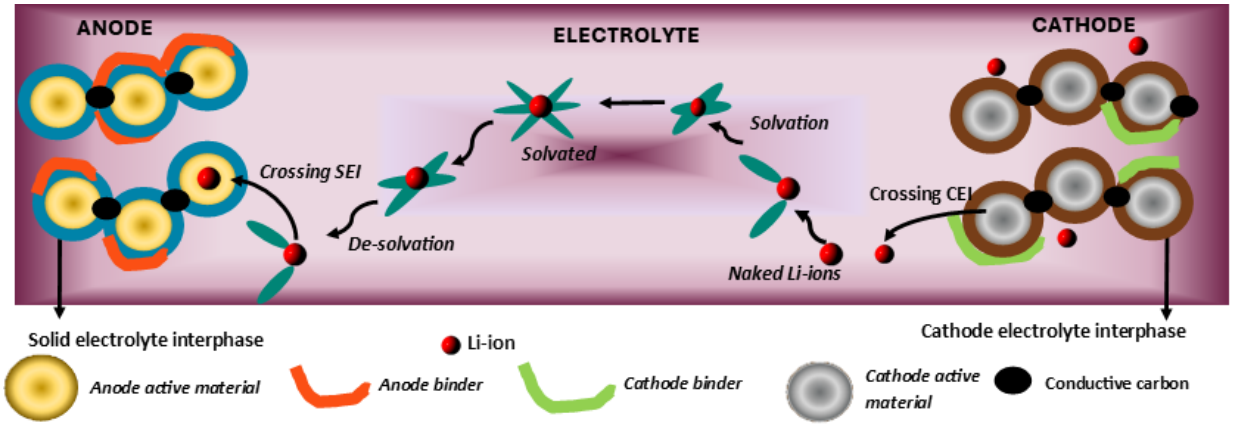

***Figure 7**: Lithium-ion movement from cathode to anode[65]*

(v) Intercalation of desolvated Li-ions between graphitic layers via the edge planes (as illustrated in Fig. 6)

This process ultimately results in the formation of LiC_6, the fully intercalated compound of lithium in graphite as shown in Fig. 8. The intercalation of lithium into graphite results in the formation of lithium-graphite intercalation compounds (Li-GICs). The Li-GICs are generally formed by staging phenomenon[66]. These stage structures are shown in terms of stage index "n" which refers to the number of graphene sheets between the intercalated lithium layers. Apart from this, another important feature of Li-GIC is the in-plane ordering of the intercalated lithium with the graphene layers called the "superlattice structure"[67]. The phase diagram for Li-GIC is shown in Fig. 8. Generally, four different stages are seen during Li-GIC formation, these stages are n= 1 to 4. The mechanism of Li-GICs is generally studied using X-ray diffraction (XRD) or Raman Spectroscopy. The lithium intercalation changes the structure from a higher to a lower stage. During the process of charging, the potential of the graphite drops rapidly until 0.8V wherein the intercalation and deintercalation takes place at potentials <0.25V vs Li/Li^+ showing three plateaus corresponding to various Li-GIC stages. Apart from n=1, four other binary phases are possible i.e n=4, 3, 2 and 2L. The stage at n=2 and 2L is two different stages when Li_xC_6, x=0.5 and x=0.33 respectively[68]. The stage structure changes successively from a higher stage to a lower stage,

Dilute Stage -1 to Stage 4 (ca 210 mV)

Stage 2L to Stage 2 (ca 120 mV)

Stage-2 to Stage 1 (ca 90 mV)

Wherein the dilute stage-1 denotes a phase where Li-ions are intercalated randomly between layers of graphite followed by stage-2L wherein 'L' denotes that Li-ions are organized in a rather liquid-like manner and are not perfectly ordered within the layers. The single layers of graphene slide against each other thus changing the stacking order from ABABA stacking to AIAIA stacking when fully lithiated stage is reached (LiC_6 ; wherein I is the intercalant layer)[67]. The interlayer distance between the graphene layers increases by 10.4% reaching 3.70 for LiC_6. The intercalation of lithium into graphite enables the formation of LiC_6, which defines the theoretical maximum specific capacity of graphite at 372 mAh/g[69]. These phase transitions can be well monitored by appearance of a sequence of potential plateaus in the galvanostatic charge-discharge profiles. However, a major limitation of graphite

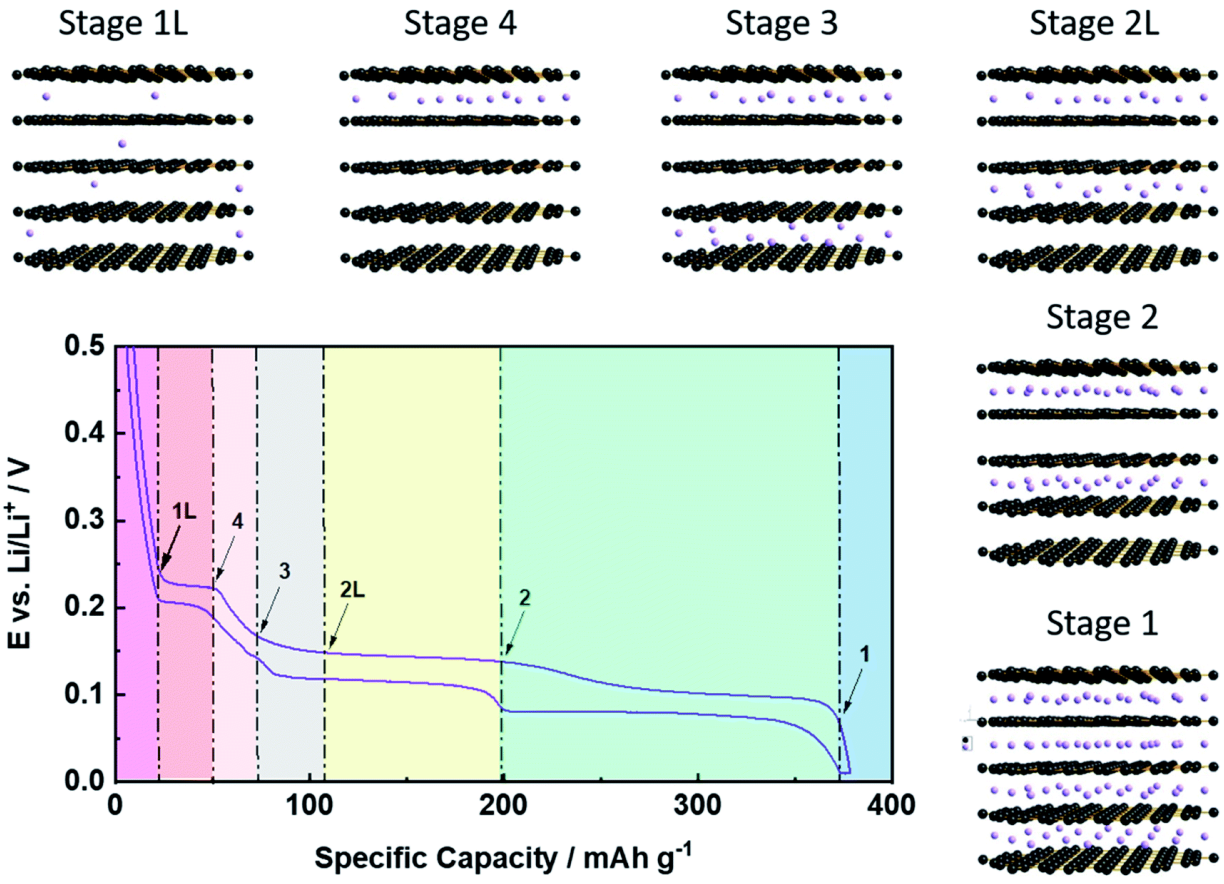

Figure 8: *Stages involved during lithium-ion storage in graphite*[66]

arises during high-rate (fast) charging. Under such conditions, the influx of lithium ions increases substantially, requiring the ions to travel longer lateral distances along the graphite surface before reaching active intercalation sites[65]. This is due to the structural anisotropy of graphite, wherein intercalation is permitted only through edge planes, while the basal planes are impermeable to lithium ions (as illustrated in Fig. 6). Consequently, during fast charging, lithium ions may fail to intercalate efficiently, leading to their accumulation on the anode surface. This condition can trigger the nucleation and growth of lithium dendrites, which pose serious safety hazards and performance degradation, especially under aggressive charging regimes.

In addition to graphite, both soft carbons and hard carbons have demonstrated higher specific capacities than the theoretical capacity of graphite. Soft carbons, also referred to as graphitizable carbons, belong to a class of disordered carbon materials that can be transformed into graphite upon exposure to high-temperature heat treatment—typically around 2500 °C[70]. During this process, the disordered structure of soft carbon undergoes structural reordering, progressively converting into a more crystalline and ordered graphitic form. These soft carbons show a large hysteresis in the charge and discharge profiles indicating the loss of some amount of energy in the form of heat. When cycling for longer duration, poor cyclability is observed. Various theories concerning the Li-ion storage have been proposed for the soft carbons such as LiC_2 formation with lithium-ion insertion between graphitic layers, lithium doping into nanoscopic cavities, formation of ionic complexes, or chemical reactions between lithium-ions and edges of carbon fragments[71]. However, the mechanism is still controversial.

(b) *Hard carbons*

These are carbon-based materials that are also known as non-graphitizable carbons with disordered arrangement of the carbon layers. The spacing between these carbon layers is generally >3.5Å with a large number of nanovoids, pores as well as edges. Unlike graphite's long-range ordered graphitic planes, hard carbons resist graphitization even at extremely high temperatures up to 3000 °C[65]. Their inability to graphitize was proposed to be related to the high extent of interlayer crosslinking. It is generally assumed that the covalent C-O-C bonds play a major role in the precursors' inability to graphitize. In fact, HCs were one of the pioneer materials to be applied as anodes in LIBs by Sony Corporation's second-generation LIBs which were later replaced by graphite in the third generation. The "falling cards" model of hard carbons (HCs), proposed by Dahn et al., is the most widely accepted structural model[72]. It describes HCs as having small graphitic sheets, amorphous regions, defect sites, and numerous nanopores. In this model, the small graphene sheets in HCs typically exhibit limited stacking, with a maximum of 2-6 layers but currently it is widely accepted that the number of stacked layers depends on the precursor. The (002) interlayer spacing between graphitic layers in HCs is usually determined using Bragg's law based on X-ray diffraction results and is generally larger than graphite. The nanopores in HCs can be either open or closed[73]. Open pores generally increase the surface area but can lead to a lower initial coulombic efficiency (ICE). In contrast, closed pores are considered preferable as active sites for lithium-ion storage. Additionally, HCs contain defect sites and edges. Defect sites arise from the presence of pentagonal or heptagonal rings instead of the usual hexagonal carbon rings within the graphitic planes. Moreover, introducing heteroatoms can also create additional

defect sites within the HC structure. The presence of a large number of nanovoids, pores, defect sites and edges give HCs a higher specific capacity than graphite. The charge-discharge profiles of hard carbons typically exhibit sloping curves, whereas graphite shows a well-defined plateau in its charge-discharge profile. This plateau corresponds to lithium-ion intercalation in graphite around 0.2V whereas the sloping profile in HCs corresponds to Li-ion storage[65,74] mechanism which involves several processes such as (i) adsorption of Li-ions at the surface, edges, and defect sites (ii) Li-ion adsorption within nanovoids and pores, and (iii) intercalation of Li-ions between the carbon layers. However, what is typically considered a benefit can also become a drawback. For instance, while the high number of defect sites and micropores in HCs can be advantageous, they can also lead to issues such as lithium-ion trapping. This trapping effect can result in a low initial coulombic efficiency (ICE), causing significant irreversible capacity loss in the full-cell performance[65]. Hard carbons are generally obtained by thermally annealing pure organic compounds or biomass-derived precursors. Upon carbonization of the precursors, small molecules such as H_2O, CO_2 and N_2 are released leading to materials with high porosity and low material density. The nature of pores is not always “open” particularly if the annealing is conducted at temperatures >1200 °C[65]. Carbonization involves dehydrogenation, condensation, hydrogen transfer, and isomerization.

The sodium storage mechanism in HCs remains a highly debated and controversial topic, largely because it varies significantly with the choice of carbon precursors. During sodiation, four major processes are generally observed: adsorption, pore filling, intercalation, and electrolyte decomposition. Adsorption of sodium ions occurs on the surface of HC, particularly at defect sites

or regions containing heteroatoms. Intercalation happens between graphitic-like carbon layers, enabling sodium-ions to insert without major structural disruption. Pore filling involves the formation of quasi-metallic sodium clusters within both open and closed pores[26]. Electrolyte decomposition arises because the lowest unoccupied molecular orbital (LUMO) of the organic solvent is lower than the highest occupied molecular orbital (HOMO) of the anode material, leading to electron transfer from the anode to the electrolyte—an event that mainly occurs during the first sodiation cycle, causing irreversible capacity loss. Sodium ion storage in HCs can proceed through adsorption or pore filling[75]. In the case of open porosity, sodium ions are mainly stored through surface adsorption, which exhibits a capacitive-dominated behavior, typically reflected as a sloping voltage profile during sodiation. In contrast, closed pore filling is a diffusion-controlled process, leading to the formation of quasi-metallic sodium clusters and resulting in a low-voltage plateau in the sodiation profile. Since sodium storage in open pores is controlled by the surface, it is classified as capacitive adsorption, whereas sodium storage in closed pores requires bulk diffusion of sodium ions[76]. Despite significant progress, there is still considerable debate within the research community regarding whether sodium is ultimately stored in the form of ions or as metallic clusters.

1.4 Issues with fast charging

The ion intercalation in anodes generally involves (1) diffusion of solvated ions in the electrolyte (2) stripping-off of the solvation sphere surrounding the ions known as desolvation (3) diffusion of naked ions through the SEI (4) electron transport in the anode as well as anode-current collector interface (5)

intercalation of naked ions in between the graphitic layers. However, at faster charging currents, slower movement of ions in any one of these components can lead to overpotential which can be classified as (1) ohmic polarization (2) concentration polarization and (3) charge transfer overpotential. Ohmic polarization generally causes a voltage drop across the electrodes within the electrolyte, which might make the battery reach its cut-off voltage earlier than expected, leading to a decrease in its specific capacity. In addition to this, low ion transference within the electrolyte can also lead to concentration gradients appearing as concentration polarization, especially during fast charging. Enhancing the ionic conductivity of the electrolyte and improving the ion transference number can aid in reducing both ohmic and concentration polarizations. Apart from these, the sluggish kinetics for diffusion of ions as in the case of graphite, particularly from its surface to its interior, can also lead to concentration polarization. The limited availability of active sites for intercalation creates concentration gradients contributing to concentration polarization and the subsequent accumulation of ions, which can result in plating. The third type of overpotential, charge transfer overpotential is generally observed at the electrode-electrolyte interface. At the interface, ion transfer to the anode material occurs through (1) de-solvation of the ions, followed by (2) movement of naked ions through the SEI and (3) transfer of ions to the anode material. The energy required for de-solvation at the interphase can be quantified as activation energy for de-solvation $\boldsymbol{E_a}$, which is calculated using the Arrhenius equation (eq.2),

$$\frac{\mathbf{1}}{\boldsymbol{R_{ct}}} = \boldsymbol{A exp}\left(-\frac{\boldsymbol{E_a}}{\boldsymbol{RT}}\right) \qquad \text{----------(2)}$$

R represents gas constant, A represents Arrhenius factor and R_{ct} is charge-transfer overpotential. The activation energy E_a is generally observed to be very small <1kJ/mol for electron transfer to graphite anode whereas the energy required for desolvation during transfer at the interphase is largest, typically requiring around 50-70 kJ/mol. Hence, de-solvation is observed to be the most energy consuming process amongst others during ion movement. The charge transfer overpotential at this stage can occur due to either high energy barriers for desolvation, challenges in the movement of bare ions through SEI or reduced electronic conductivity of the electrode—whether individually or collectively—can all contribute to charge transfer overpotential. Thus, in general, overpotentials play a significant role in impeding the fast-charging performance of the battery. Due to various types of overpotentials, when the overpotential at the anode η_{anode} becomes excessively and anode potential E_{anode} becomes lower metal deposition becomes inevitable. In case of SIBs, the overpotentials are even more significant due to larger size of the ion which may lead to sluggish diffusion kinetics.

1.5 Motivation and Outline of this Thesis

Recent advancements have expanded the use of batteries across diverse fields, from powering electric vehicles (EVs) to enable large-scale energy storage and enhance portable electronics, making them a key player in the transition to a greener future. EVs have made significant progress, yet they continue to fall behind the traditional fuel-based cars due to limitations in current battery technology, particularly in terms of energy density and charging speed. To effectively compete with traditional fuel-based cars, EVs still need to achieve a

minimum driving range of 800 kms on a single charge. For a typical LIB, the energy density of a battery is given by electrochemical voltage ***(V)*** of the utilized cathode/anode ($\boldsymbol{C_c}$ / $\boldsymbol{C_a}$)and the specific capacity ***(C),***

$$\boldsymbol{E} = \frac{\boldsymbol{C_c} \times \boldsymbol{C_a}}{\boldsymbol{C_c} + \boldsymbol{C_a}} \times (\boldsymbol{V_c} - \boldsymbol{V_a})$$

Where C_c/C_a is the specific capacity of cathode/anode and V_c/V_a is the nominal or average voltage of cathode/anode. Therefore, it is clear from equation that the energy density of the battery can be enhanced by elevating the operating voltage, increasing the specific capacity or boosting the mass loading of the electrodes, and so forth. Utilizing high-capacity anodes such as silicon-carbon composites can be an interesting approach as well. However, currently none of the high-capacity anodes can match the cycle life of the carbon-based anodes. The electrode's mass loading is another critical factor in determining the energy density of the batteries, since the specific capacity of the battery depends on the mass of the active material as well. Increasing mass loadings in electrodes can indeed lead to higher gravimetric capacities, allowing batteries to store more energy per unit area. However, excessively thick electrodes can face challenges such as fractures and delamination from the current collector and increased internal resistance, compromising the overall performance and durability of the battery. Enhancing the energy density of anodes can be effectively achieved by increasing the density of active sites for ion storage. Utilizing HCs with a disordered arrangement of carbon planes serves as a promising approach, as their structural irregularities introduce numerous defects and pores that act as additional ion storage sites. Moreover, heteroatom doping—introducing elements such as nitrogen (N), phosphorus (P), sulfur (S), oxygen (O), or fluorine (F) into the carbon matrix—has

emerged as a compelling strategy to tailor the physical and chemical properties of carbon materials. These heteroatoms can expand interlayer spacing, enhance electronic conductivity, and create more active sites, thereby facilitating faster ion diffusion and improved charge transfer kinetics.

1.6 Objective of this Thesis

Lithium-ion batteries (LIBs) were first commercialized in 1991 by Sony Corporation in Japan. As EVs become increasingly vital to the global shift toward sustainable transportation, one of the most critical challenges facing LIB technology is enabling ultra-fast charging. To compete with the convenience provided by the fuel-based cars, next-generation LIBs must achieve charging times under 15 minutes while delivering a range of up to 800 kilometers on a single charge[77]. Meeting this demanding performance target requires fundamental improvements in battery materials, particularly the anode. Graphite's rigid structure hampers lithium-ion diffusion and increases the risk of lithium plating under fast-charging conditions, making it a major obstacle to achieving rapid charging performance[77,78]. To address this, numerous strategies—such as creating multichannel architectures, introducing nanoscale porosity, or coating with turbostratic carbon—have been employed to enhance graphite's rate capabilities by reducing ion diffusion lengths and increasing active storage sites. Rather than further optimizing graphite material with inherent structural rigidity, this research proposes an alternative strategy: the use of hard carbon with disordered structures, enlarged interlayer spacings, abundant nanovoids, and a high density of defect sites[28]. These structural features are highly favorable for rapid ion transport and offer increased active sites for lithium storage, making

hard carbons a promising class of materials for fast-charging LIBs. Various precursors have been employed in the synthesis of hard carbons to date, including synthetic resins and biomass-derived residues. However, synthetic resins lack environmental sustainability, while biomass-derived materials offer limited control over chemical composition, particularly with respect to the incorporation of specific heteroatoms. In contrast, bio-based polymers represent a highly promising alternative, as they combine environmental friendliness with synthetic tunability. Heteroatom doping of hard carbons can be an even more interesting approach as it can increase the active sites for ion storage as well as provide additional advantages such as introducing defect sites or enlarging the interlayer spacing[79]. These polymers can be deliberately designed to incorporate desired heteroatoms, enabling a more controlled approach towards tailoring the properties of the resulting hard carbon. Previously, we reported a heavily nitrogen doped HC endowed with a nitrogen doping of approx. 17wt% as an extremely fast charging anode for LIB. It exhibited an extreme fast charging capability at 18.6 A/g by delivering a discharge capacity twice that of graphite with a capacity retention as high as 90% even after 3000 cycles[80]. These results encouraged our group to further explore the effect of dual heteroatom doping in HCs for fast charging applications. Therefore, Chapter 2 of this thesis explores the utilization of bio-based poly(benzimidazole-co-amide) as a single-source precursor for the synthesis of nitrogen and oxygen co-doped hard carbon (N,O co-doped HC). Although oxygen doping is generally unavoidable, it is often neglected in analysis, and its role in influencing fast-charging performance in batteries remains inadequately understood. To bridge this gap, co-polymers with varying polybenzimidazole to polyamide (PBI:PA) ratios—namely 8.5:1.5, 7:3, and

5:5—were pyrolyzed at 800 °C to produce hard carbons with differing levels of nitrogen and oxygen doping. This strategy was used not only to demonstrate the effective use of a bio-based polymer as a single-source for N,O co-doped HC anodes, but also to facilitate a deeper understanding of the optimal nitrogen and oxygen doping level required for enhanced fast-charging battery performance.

While sodium-ion batteries (SIBs) have shown promising potential as future energy storage solutions, achieving fast-charging performance remains a significant challenge. Although hard carbons have been widely used as anodes in these batteries, heteroatom doping appears to be a crucial factor in enhancing their fast-charging capabilities. Nitrogen doping is known to improve electronic conductivity, create defect sites that facilitate ion movement, and enable ion storage through pseudo capacitance. On the other hand, sulfur doping has been found to increase the d-spacing and provide additional active sites for ion storage. Chapter 3 thus explores nitrogen and sulfur co-doped hard carbon (N,S co-doped HC) synthesized from the bio-based poly(benzothiazole) and used as an anode material for SIBs. The N, S co-doped HC were prepared at two different pyrolysis temperatures to assess the influence of morphological features on their electrochemical performance.

Chapter 4 of this thesis presents a summary of the structure–activity relationships observed in both N,O co-doped and N,S co-doped hard carbon materials for LIBs and SIBs, respectively, emphasizing their distinct impacts on battery performance.

References

1 M. Wakihara and O. Yamamoto, *Lithium-ion batteries- Fundamentals and Performance*, Kodansha Ltd., Tokyo (Japan) and Wiley-VCH GmbH, Weinheim (Federal republic of Germany), 1998.

2 M. Kandhasamy, B. K. Duvaragan, S. Kamaraj and G. Shanmugam, in *ACS Symposium Series*, American Chemical Society, 2024, vol. 1484, pp. 1–25.

3 V. Karol, P. Sharma, A. Singh, D. Goel and S. Kaur, in *ACS Symposium Series*, American Chemical Society, 2024, vol. 1488, pp. 1–15.

4 X. Cheng, Z. Shi, N. Glass, L. Zhang, J. Zhang, D. Song, Z. S. Liu, H. Wang and J. Shen, 2007, preprint, DOI: 10.1016/j.jpowsour.2006.12.012.

5 X. Cheng, J. Zhang, Y. Tang, C. Song, J. Shen, D. Song and J. Zhang, *J Power Sources*, 2007, **167**, 25–31.

6 S. Li, L. Shi, Y. Guo, J. Wang, D. Liu and S. Zhao, *Chem Sci*, 2024, **15**, 11188–11228.

7 T. B. Ferriday and P. H. Middleton, *Int J Hydrogen Energy*, 2021, **46**, 18489–18510.

8 Z. Wu, P. Zhu, Y. Huang, J. Yao, F. Yang, Z. Zhang and M. Ni, *Chem Rev*, DOI:10.1021/ACS.CHEMREV.4C00614/ASSET/IMAGES/LARGE/CR4C00614_0026.JPEG.

9 X. Gang, H. A. Hjuler, C. Olsen, R. W. Berg and N. J. Bjerrum, *J Electrochem Soc*, 1993, **140**, 896–902.

10 M. Bischoff, *J Power Sources*, 2006, **160**, 842–845.

11 J. Sun, B. Luo and H. Li, *Advanced Energy and Sustainability Research*, 2022, **3**, 2100191.

12 J. Zhang, M. Gu and X. Chen, *Micro and Nano Engineering*, 2023, **21**, 100229.

13 J. Thakur, P. Phogat, N. Shreya, R. Jha and S. Singh, *Physical Chemistry Chemical Physics*, 2025, **27**, 4045–4077.

14 N. Wang, H. Wan, J. Duan, X. Wang, L. Tao, J. Zhang and H. Wang, *Mater Today Adv*, 2021, **11**, 100149.

15 D. U. Sauer, *Encyclopedia of Electrochemical Power Sources*, 2009, 805–815.

16 J. McDowall, 2008, 303–308.

17 B. Hariprakash, A. K. Shukla and S. Venugoplan, *Encyclopedia of Electrochemical Power Sources*, 2009, 494–501.

18 A. K. Shukla, M. K. Ravikumar and T. S. Balasubramanian, *J Power Sources*, 1994, **51**, 29–36.

19 L. Ion, *Lithium ion batteries-Fundamentals and Performance*, 1998.

20 Y. Nishi, *Electrochemical Society Interface*, 2016, **25**, 71–74.

21 A. Yoshino, 2012, preprint, DOI: 10.1002/anie.201105006.

22 T. Wulandari, D. Fawcett, S. B. Majumder and G. E. J. Poinern, *Battery Energy*, 2023, **2**, 20230030.

23 A. N. Singh, M. Islam, A. Meena, M. Faizan, D. Han, C. Bathula, A. Hajibabaei, R. Anand and K. Nam, *Adv Funct Mater*, DOI:10.1002/ADFM.202304617.

24 M. Yuan, B. Cao, H. Liu, C. Meng, J. Wu, S. Zhang, A. Li, X. Chen and H. Song, *Chemistry of Materials*, 2022, **34**, 3489–3500.

25 C. Wang, H. Cai, S. Zheng, B. Wang and S. Wang, *Electrochim Acta*, 2024, **504**, 144956.

26 N. Yabuuchi, K. Kubota, M. Dahbi and S. Komaba, *Chem Rev*, 2014, **114**, 11636–11682.

27 Y. Liu, B. V Merinov and W. A. Goddard, 2016, **113**, 3735–3739.

28 X. Dou, I. Hasa, D. Saurel, C. Vaalma, L. Wu, D. Buchholz, D. Bresser, S. Komaba and S. Passerini, *Materials Today*, 2019, **23**, 87–104.

29 R. V. Chebiam, A. M. Kannan, F. Prado and A. Manthiram, *Electrochem commun*, 2001, **3**, 624–627.

30 A. Manthiram, *Nat Commun*, 2020, **11**, 1–9.

31 P. Gupta, S. Pushpakanth, M. A. Haider and S. Basu, *ACS Omega*, 2022, **7**, 5605–5614.

32 M. He, S. Liu, J. Wu and J. Zhu, *Progress in Solid State Chemistry*, 2024, **74**, 100452.

33 J. Xiao, X. Li, K. Tang, D. Wang, M. Long, H. Gao, W. Chen, C. Liu, H. Liu and G. Wang, *Mater Chem Front*, 2021, **5**, 3735–3764.

34 X. Xiang, K. Zhang and J. Chen, *Advanced Materials*, 2015, **27**, 5343–5364.

35 S. Kainat, J. Anwer, A. Hamid, N. Gull and S. M. Khan, *Mater Chem Phys*, 2024, **313**, 128796.

36 J. Kalhoff, G. G. Eshetu, D. Bresser and S. Passerini, *ChemSusChem*, 2015, **8**, 2154–2175.

37 M. Li, C. Wang, Z. Chen, K. Xu and J. Lu, *Chem Rev*, 2020, **120**, 6783–6819.

38 F. Cheng, M. Cao, Q. Li, C. Fang, J. Han and Y. Huang, *ACS Nano*, 2023, **17**, 18608–18615.

39 H. Darjazi, M. Falco, F. Colò, L. Balducci, G. Piana, F. Bella, G. Meligrana, F. Nobili, G. A. Elia and C. Gerbaldi, *Advanced Materials*, 2024, **36**, 2313572.

40 K. N. Wood, E. Kazyak, A. F. Chadwick, K. H. Chen, J. G. Zhang, K. Thornton and N. P. Dasgupta, *ACS Cent Sci*, 2016, **2**, 790–801.

41 M. P. Bondarde, R. Jain, J. S. Sohn, K. D. Lokhande, M. A. Bhakare, P. S. Dhumal and S. Some, *Lithium-Sulfur Batteries: Materials, Challenges and Applications*, 2022, 521–545.

42 U. Kumar Sen, A. Shaligram and S. Mitra, *ACS Appl Mater Interfaces*, 2014, **6**, 14311–14319.

43 S. Li, K. Wang, G. Zhang, S. Li, Y. Xu, X. Zhang, X. Zhang, S. Zheng, X. Sun, Y. Ma, S. Q. Li, K. Wang, G. F. Zhang, S. N. Li, Y. N. Xu, X. D. Zhang, X. Zhang, X. Z. Sun, Y. W. Ma and S. H. Zheng, DOI:10.1002/adfm.202200796.

44 M. Wahid, D. Puthusseri, Y. Gawli, N. Sharma and S. Ogale, *ChemSusChem*, 2018, **11**, 506–526.

45 S. Komaba, W. Murata, T. Ishikawa, N. Yabuuchi, T. Ozeki, T. Nakayama, A. Ogata, K. Gotoh and K. Fujiwara, 2011, preprint, DOI: 10.1002/adfm.201100854.

46 Y. Lu, L. Yu and X. W. (David) Lou, *Elsevier Inc.*, 2018, preprint, DOI: 10.1016/j.chempr.2018.01.003.

47 J. Nanda and V. Augustyn, .

48 L. Wang, J. Światowska, S. Dai, M. Cao, Z. Zhong, Y. Shen and M. Wang, *Mater Today Energy*, 2019, **11**, 46–60.

49 L. Cui, C. Tan, Y. Li, Q. Pan, L. Zhang, M. Zhang, Z. Chen, F. Zheng, H. Wang and Q. Li, *ACS Appl Energy Mater*, 2021, **4**, 3757–3765.

50 M. Vincent, S. Sajeev, M. Srivastava, E. Kowalska, S. Srinivasan and D. Kowalski, *Electrochim Acta*, 2025, **509**, 145309.

51 H. Xu, H. Li and X. Wang, *ChemElectroChem*, 2023, **10**, e202201151.

52 Z. Yang, M. Jiang, X. Wang, Y. Wang and M. Cao, *ACS Applied Materials & Interfaces*, 2021, **13**, 52636–52646.

53 E. Feyzi, A. K. M R, X. Li, S. Deng, J. Nanda and K. Zaghib, *Next Energy*, 2024, **5**, 100176.

54 Y. Cui, *Nature Energy 2021 6:10*, 2021, **6**, 995–996.

55 M. Zeilinger, V. Baran, L. Van Wüllen, U. Häussermann and T. F. Fässler, *Chemistry of Materials*, 2013, **25**, 4113–4121.

56 C. Ban and K. Xu, *Lithium-ion Batteries Enabled by Silicon Anodes*, .

57 M. H. Braga, A. Dębski and W. Gąsior, *J Alloys Compd*, 2014, **616**, 581–593.

58 K. Guo, R. Kumar, X. Xiao, B. W. Sheldon and H. Gao, *Nano Energy*, 2020, **68**, 104257.

59 S. M. Zheng, Y. R. Tian, Y. X. Liu, S. Wang, C. Q. Hu, B. Wang and K. M. Wang, *Rare Metals*, 2021, **40**, 272–289.

60 X. Wang, X. Zhao and L. Wang, *Batter Supercaps*, 2025, **8**, e202400551.

61 G. Nava, J. Schwan, M. G. Boebinger, M. T. McDowell and L. Mangolini, *Nano Lett*, 2019, **19**, 7236–7245.

62 N. Liu, H. Wu, M. T. McDowell, Y. Yao, C. Wang and Y. Cui, *Nano Lett*, 2012, **12**, 3315–3321.

63 Y. Mei, Y. Huang and X. Hu, *J Mater Chem A Mater*, 2016, **4**, 12001–12013.

64 J. Xu, X. Wang, N. Yuan, B. Hu, J. Ding and S. Ge, *J Power Sources*, 2019, **430**, 74–79.

65 K. S. Patnaik, B. S. Mantripragada, S. Punyasloka and N. Matsumi, *Chemical Communications*, DOI:10.1039/D4CC04776A.

66 Z. Chen, D. Bresser, J. Asenbauer, T. Eisenmann, M. Kuenzel and A. Kazzazi, *Sustainable Energy & Fuels Interdisciplinary research for the development of sustainable energy technologies*, 2020, **4**, 5363–5870.

67 T. Astles, J. G. McHugh, R. Zhang, Q. Guo, M. Howe, Z. Wu, K. Indykiewicz, A. Summerfield, Z. A. H. Goodwin, S. Slizovskiy, D. Domaretskiy, A. K. Geim, V. Falko and I. V. Grigorieva, *Nature Communications 2024 15:1*, 2024, **15**, 1–11.

68 S. Weng, S. Wu, Z. Liu, G. Yang, X. Liu, X. Zhang, C. Zhang, Q. Liu, Y. Huang, Y. Li, M. N. Ateş, D. Su, L. Gu, H. Li, L. Chen, R. Xiao, Z. Wang and X. Wang, *Carbon Energy*, 2023, **5**, e224.

69 H. Zhang, Y. Yang, D. Ren, L. Wang and X. He, *Energy Storage Mater*, 2021, **36**, 147–170.

70 Y. Liu, Y. X. Lu, Y. S. Xu, Q. S. Meng, J. C. Gao, Y. G. Sun, Y. S. Hu, B. B. Chang, C. T. Liu and A. M. Cao, *Advanced Materials*, 2020, **32**, 1–8.

71 L. Li, D. Zhang, J. Deng, Y. Gou, J. Fang, H. Cui, Y. Zhao and M. Cao, *Carbon N Y*, 2021, **183**, 721–734.

72 J. R. Dahn, W. Xing and Y. Gao, *Carbon N Y*, 1997, **35**, 825–830.

73 Q. Meng, Y. Lu, F. Ding, Q. Zhang, L. Chen and Y.-S. Hu, *ACS Energy Lett*, 2019, **4**, 2608–2612.

74 L. Kraft, J. B. Habedank, A. Frank, A. Rheinfeld and A. Jossen, *J Electrochem Soc*, 2020, **167**, 013506.

75 H. Alptekin, H. Au, A. C. Jensen, E. Olsson, M. Goktas, T. F. Headen, P. Adelhelm, Q. Cai, A. J. Drew and M.-M. Titirici, DOI:10.1021/acsaem.0c01614.

76 M. Yuan, B. Cao, H. Liu, C. Meng, J. Wu, S. Zhang, A. Li, X. Chen and H. Song, *Chemistry of Materials*, 2022, **34**, 3489–3500.

77 Y. Liu, Y. Zhu and Y. Cui, *Nat Energy*, 2019, **4**, 540–550.

78 J. Xu, X. Wang, N. Yuan, B. Hu, J. Ding and S. Ge, *J Power Sources*, 2019, **430**, 74–79.

79 H. Wang, Y. Shao, S. Mei, Y. Lu, M. Zhang, J. K. Sun, K. Matyjaszewski, M. Antonietti and J. Yuan, *Chem Rev*, 2020, **120**, 9363–9419.

80 K. S. Patnaik, R. Badam, Y. Peng, K. Higashimine, T. Kaneko and N. Matsumi, *Chemical Communications*, 2021, **57**, 13704–13707.

81 A. M. Theodore, *J Chem Res*, DOI:10.1177/17475198231183349.

2. Bio-based poly(benzimidazole-co-amide) derived N, O co-doped carbons as fast-charging anodes for lithium-ion batteries

2.1 Abstract

Lithium-ion batteries (LIBs) that can be charged faster while delivering high capacity are currently under significant demand, especially for electric vehicle applications. In this context, this study introduces a less-explored subject: nitrogen and oxygen dual-doped carbons derived from bio-based copolymers, specifically poly(benzimidazole-co-amide). The synthesis involves varying proportions of benzimidazole to amide, namely 8.5:1.5, 7:3, and 5:5. The copolymers were pyrolyzed under nitrogen atmosphere to obtain co-doped carbons wherein the copolymers acted as single sources of carbon, nitrogen, and oxygen with a nitrogen content ranging between 12.1 and 8.0 at% and oxygen doping between 11.8 and 25.0 at% named as pyrolysed polybenzimidazole-co-amide 8.5-1.5, 7-3 and 5-5. Coin cells were fabricated, and rate studies were conducted for all three samples wherein PYPBIPA8.5-1.5 outperformed all others especially at higher current densities. Intrigued by these interesting results when long cycling studies were performed at a high current density of 4.0 A/g, pyrolysed polybenzimidazole-co-amide 8.5-1.5 showed a delithiation capacity of 135 mAh/g compared to 100 mAh/g and 60 mAh/g by pyrolysed polybenzimidazole-co-amide 7-3 and 5-5, with a capacity retention of 90% even after 3000 cycles. Furthermore, full cell (2025-coin cell) was also fabricated using PYPBIPA8.5-1.5 anode and $LiNi_{0.80}$ $Co_{0.15}Al_{0.05}O_2$ (LiNCAO) cathode.

2.2 Introduction

Ever since LIBs were first discovered in the 1990s, their applications have expanded tremendously. Especially, the recent past has witnessed implementation of LIB in every other device ranging from earphones to electric vehicles (EVs)[1]. EVs are currently the most environmentally friendly means of transport available in the market. However, the state-of-the art EVs are still unable to completely satisfy the customers with respect to driving range as well as time for charging. Batteries which can be charged in less time afford only a few miles, whereas batteries which can sustain a long distance take more time for charging, thus arising a tradeoff between long distance and fast charging[2]. To overcome these problems, various types of anode materials are currently being investigated across the world. Of all these materials, carbonaceous materials seem to be the best choice owing to their non-toxicity, low cost and simplicity in synthetic procedures[3,4]. Amongst the various carbon-based materials, graphite seems to be one of the preferred anode materials, nevertheless its slow Li-ion kinetics inside the bulk material limits its fast-charging applications. Hence, there is an urgent need to discover novel carbon materials that can afford faster Li-ion kinetics. In light of this, hard carbons (HCs) seem to be an excellent choice as anode materials for fast charging[5]. HCs are materials with short range graphitized domains arranged in a disordered manner, with a large number of nanovoids and defect sites[6]. Unlike graphite, due to their unique structure they can store Li-ions not only through intercalation between carbon planes but also through surface adsorption at defect sites, edges and nanovoids thus contributing to faster Li-ion kinetics. Alongside, heteroatom doping using elements such as N, O, S, P etc. can also contribute to faster kinetics owing to surface based redox reactions between heteroatoms and Li-ions. The introduction of heteroatoms can

also induce defect sites that promote perpendicular movement of ions from one plane to another plane, boost electrical conductivity and reduce charge transfer impedance that are helpful during fast charging. Hence, heteroatom doped HCs having combined benefits of both counterparts can be the perfect choice of carbon-based anode materials for fast charging batteries[7]. Previously, our group reported a heavily nitrogen doped HC endowed with a nitrogen doping of approx. 17wt% as an extremely fast charging anode for LIB. Due to the synergistic effects of heavy nitrogen doping using a polymer source, large number of defect sites, enlarged d-spacing, it exhibited an extreme fast charging (XFC) capability at 18.6 A/g and ultralong cyclability of 3000 cycles with 90% capacity retention[8]. These results encouraged our group to further explore the effect of dual heteroatom doping in HCs for fast charging applications. Though O doping is inevitable in most carbon materials due to its widespread and unavoidable presence in most of the precursors, its role is generally ignored, and the effect of oxygen co-doping is not discussed. Hence, the aim of present work is to understand the effect of O-doping along with N-doping especially in terms of fast charging performance of the batteries. Furthermore, anodes such as lithium titanate (LTO) and TiO_2 have attracted significant attention for fast charging applications. However, there are notable concerns about their limitations, specifically the challenge of low energy density, which has been thoroughly emphasized. Despite the implementation of various innovative approaches to enhance the energy density of TiO_2, such as incorporating crystalline $Ti_2O_{1.3}(PO_4)_{1.6}$ as a hybrid material with TiO_2 and carbon or utilizing 2D $Ti_2(PO_4)_2F$ nanosheets[9,10], the lower operating voltage and substantial cost still remain as significant concerns. On the other hand, graphite, derived from petroleum, has long been considered an ecologically friendly material. However,

concerns about its sustainability raise questions about its viability for the future. With these concerns, hard carbon materials derived from various biomaterials such as sucrose[11], glucose, cellulose[12], lignocellulose etc. are being actively investigated by researchers. However, achieving precise control over the specific proportions of heteroatoms in such compounds proves challenging due to their bio-derived nature. Also, these compounds being non-aromatic cause low char yields. Hence, the objective of the present work was to utilize a bio-based polymer poly(benzimidazole-co-amide) as the single source of carbon, nitrogen and oxygen for obtaining N, O co-doped HCs. Further, in order to understand the optimum nitrogen and oxygen doping balance in carbon materials suitable for fast charging, we synthesized co-polymers at varying proportions of polybenzimidazole: polyamide (PBI-PA) of 8.5:1.5, 7:3 and 5:5 and pyrolyzed them at 800°C to obtain N, O co-doped HCs. The objective of this research was twofold: first, to employ a bio-based polymer-derived heteroatom-doped hard carbon as an anode material for lithium-ion batteries; and second, to optimize the nitrogen and oxygen doping levels in order to investigate their impact on the fast-charging performance of the lithium-ion batteries. Electrochemical studies revealed that pyrolyzed polybenzimidazole-co-amide 8.5-1.5 exhibits a maximum de-lithiation capacity of 135 mAh/g at a current density of 4.0 A/g. This underscores its suitability as the most favorable material for applications requiring fast charging, surpassing their counterparts. The detailed synthetic procedure, electrochemical studies and discussions pertaining to it are presented in the following sections.

2.3 Experimental Section

Materials

1.0 M $LiPF_6$ in EC/DEC= 50/50 (v/v), battery grade, was purchased from Sigma Aldrich. Battery grade acetylene black was purchased from Denka Japan Private Co. Ltd. for usage as conductive material in the anode, Poly(vinylidene) fluoride was purchased from Sigma Aldrich. N-Methyl 2-pyrrolidone (NMP), was purchased from FUJIFILM Wako Pure Chemical Corporation (Wako, Japan).

Synthesis

The detailed synthetic procedure of the polymers was reported by Kaneko et.al[13]. Briefly, the polymers were synthesized using 3,4-diaminobenzoic acid (3,4-DABA) and 4-aminobenzoic acid as precursors. The polymers were synthesized using 3,4-diaminobenzoic acid (3,4-DABA) and 4-aminobenzoic acid (4-ABA) as precursors (Scheme 1). The polymers were synthesized by maintaining precursor ratios of 9-1, 8.5-1.5, 7-3, 6-4 and 5-5 for obtaining co-polymers PBI-PA in the ratios 9-1, 8.5-1.5, 7-3, 6-4 and 5-5 respectively. The ratios of polymers were chosen such that there was a difference of ~10% amide content in each polymer with the aim of

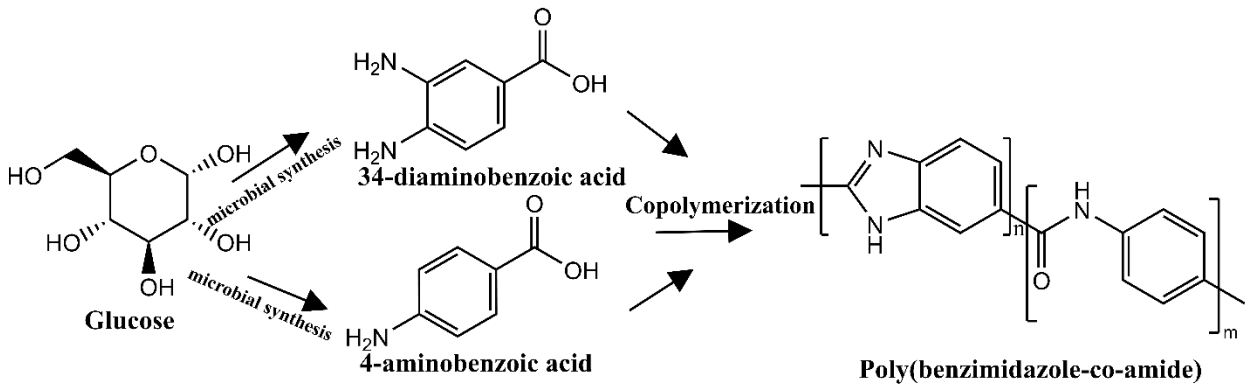

Synthetic scheme 1: *Synthetic procedure for poly(benzimidazole-co-amide)*[13]

obtaining varying oxygen doping contents. Wherein in case of PBIPA10-0(PBI), the homopolymer was synthesized using only 3,4 DABA as monomer[8]. The homopolymer polyamide 0-10 was synthesized using only 4-ABA. For both the homopolymer and co-polymer the same synthetic route was followed i.e., initially the solvent (PPA) was heated at 100°C for removing any moisture followed by addition of precursors and copolymerization at 200°C for 14 h in nitrogen atmosphere. The obtained polymers were cooled to room temperature and stirred in a beaker containing distilled water to wash off the unreacted precursors. The polymers were then crushed and dispersed in 10% KOH aq., solution and the mixture was continuously stirred at room temperature overnight before filtering and washing with water until neutral pH. The resulting polymer powders were dried under vacuum at 80°C for 8h. The polymers were then pyrolyzed at 800°C for obtaining carbon materials which were named PYPBIPA9-1,8.5-1.5, 7-3, 6-4, 5-5 respectively. The pyrolysis was conducted in two different steps. Initially the temperature was raised to 750°C at 5°C/min which took 2 hours 20 minutes and later it increased to 800°C at 1°C/min which took 50 minutes. Further, the temperature was maintained to 800°C for 1 hour, hence the total time for pyrolysis was 4 hours 10 minutes. The pyrolyzed materials were ultrasonicated in 10% HCl solution to remove any amorphous carbon or carbonate impurities in the samples. The ultrasonication was followed by drying at 80°C under vacuum for about 12 hours to remove water. X-ray photoelectron spectroscopy (XPS) measurements were conducted on a Fissons instrument S-probe TM 2803 instrument. High resolution transmission electron microscopy (HR-TEM) images were acquired by scanning the transmission electron microscope, JEM-ARM200F from JEOL Co. Ltd at an acceleration voltage of 200 kV. Powder X-ray diffraction (XRD) studies were

conducted on Smart Lab X-Ray Diffractometer, Rigaku with Cu Kα radiation (λ = 0.154 nm, over the 2θ range of 2°- 45°with a step size of 0.02°). Nitrogen adsorption-desorption experiments were performed using a BELSORP-mini II -HS-1 instrument.

Electrode preparation and cell fabrication

The respective carbon materials, PVDF, and acetylene black was mixed in 8:1:1 ratio and rotated in Kakuhunter ball mill for preparing a uniform slurry. The obtained slurry was coated on copper foils using a doctor blade while maintaining a thickness of 0.1 mm. The electrodes were then kept in vacuum oven at 80°C for about 12 hours. The dried electrodes were calendared to 0.06 mm thickness at 80°C. Electrodes of 17 mm diameter was punched out of the calendared sheets. Before performing full cell studies, high loading anodic half cells studies were performed. The high loading anodic half cells with~6.8 mg/cm^2 loading were initially precycled for 2 cycles at 0.25 A/g followed by rate studies. After that, the high loading anodic half cells were decrimped, and reassembled into a full cell. Similarly, for full cell fabrication, LiNCAO as cathode was precycled at 0.25 A/g followed by reassembling into full cell. CR2025 type coin cells were fabricated inside an argon filled glove box (O_2, H_2O < 0.5 ppm) using PYPBIPA8.5-1.5, 7-3, and 5-5 based anodes, lithium foil as counter and reference electrode, polypropylene separator (25 µm, Celgard) and 1.0M $LiPF_6$ (50:50) ethylene carbonate: diethyl carbonate (EC: DEC) as electrolyte. For fabrication of symmetric cells, anodic half-cells were prepared and cycled at 50 mA/g for three cycles and the cells were decrimped in Ar-filled glovebox while anode is in lithiated state. The lithiated electrode and an electrode with same composition in unlithiated state were used to prepare symmetric cell. Symmetric

cells were rested for 12 hours before starting charge-discharge studies. After 12 hours, symmetric cells were cycled at 50 mA/g current density.

Electrochemical measurements:

All electrochemical measurements were performed in the potential range of 0.01V to 2.1V (vs Li/Li^+) at 25°C. Cyclic voltammetry was performed in biologic VSP workstation at 0.1, 0.2, 0.4, 0.6, 0.8 and 1.0 mV/s scan rates. Potentiostaic electrochemical impedance spectroscopy (PEIS) was performed in a frequency range of 10 MHz to 0.1 Hz. Galvanostatic charge-discharge (GCD) measurements were conducted in biologic battery cycling system at various current densities.

2.4 Characterization and Electrochemical Studies

Previously, our group reported a heavily nitrogen doped HC endowed with a nitrogen doping of approx. 17wt% as an extremely fast charging anode for LIB[8]. Due

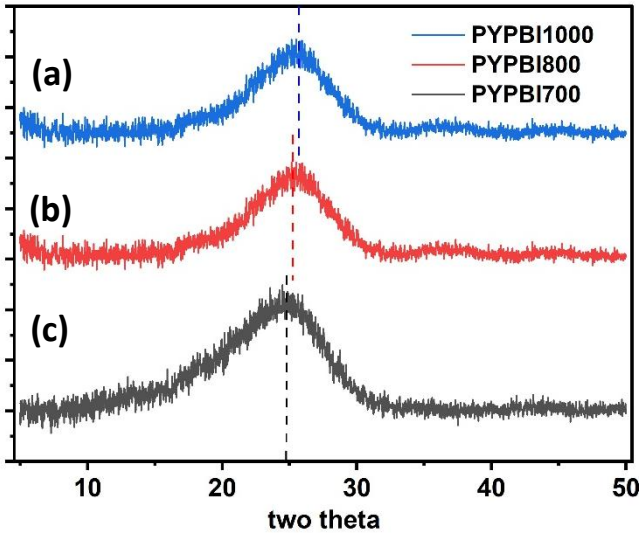

***Figure 9**: XRD of (a)PYPBI1000 (b)PYPBI800 and(c) PYPBI700*

to the synergistic effects of heavy nitrogen doping using a polymer source, large number of defect sites, enlarged d-spacing, it exhibited an extreme fast charging (XFC) capability at 18.6 A/g and ultralong cyclability of 3000 cycles with 90%

*T**able 6:** Comparison of Elemental Analysis by EDS of PYPBI700, 800 and 1000*

Element	PYPBI700 wt%	PYPBI800 wt%	PYPBI1000 wt%
C	75.25	77.25	87.66
N	**20.34**	**17.51**	**7.06**
O	4.41	5.24	5.08
Total	100.00	100.00	100.00

capacity retention. We initially obtained the carbon materials at three different carbonization temperatures of 700°C, 800°C, and 1000°C hereafter referred to as PYPBI700, PYPBI800 and PYPBI1000. The XRD plots of obtained carbon materials is presented for PYPBI1000, PYPBI800 and PYPBI700 in Fig. 9(a)(b)and(c) respectively. The d-spacing was observed to decrease with increasing pyrolysis temperature from 3.60 to 3.5 to 3.4 Å. The full width at half maximum calculated from the XRD plot was observed to be 7.68°, 5.45° and 2.56° indicating a decrease in the amorphous nature of the carbons and increase in crystalline nature. The elemental analysis obtained from EDX analysis also indicated a decrease in nitrogen content as shown in Table 6. Following this, electrochemical performance was evaluated at various current densities: 0.04, 0.07, 0.20, 0.37, 0.74, 1.85, and again at 0.04 A/g. The discharge capacities for PYPBI700, PYPBI800, and PYPBI1000 are summarized in Table 7. Although PYPBI700 had a higher nitrogen content, its greater amorphous nature likely resulted in lower performance compared to PYPBI800. In contrast, the reduced nitrogen content in PYPBI1000 contributed to its lowest discharge capacity among all samples. Among the samples, PYPBI800 demonstrated the best electrochemical performance, achieving a maximum discharge capacity of 127

***Table 7**: Comparison of discharge capacities of PYPBI700, 800 and 1000*

Current Density(A/g)	Discharge Capacity (mAh/g)		
	PYPBI700	PYPBI800	PYPBI1000
0.04	320	**375**	240
0.07	256	**331**	199
0.20	194	**254**	170
0.37	149	**206**	148
0.74	130	**168**	130
1.85	99	**127**	95
0.04	338	**405**	228

mAh/g even at the high current density of 1.85 A/g (Fig. 10). This superior performance can be attributed to the optimized d-spacing, amorphous carbon fraction and favorable nitrogen doping levels in the carbon material. Consequently, all subsequent studies involving the copolymer PBIPA were carried out using a pyrolysis temperature of 800°C. Based on these results, 800°C was identified as the optimal pyrolysis temperature for synthesizing hard carbons from bio-based polymers.

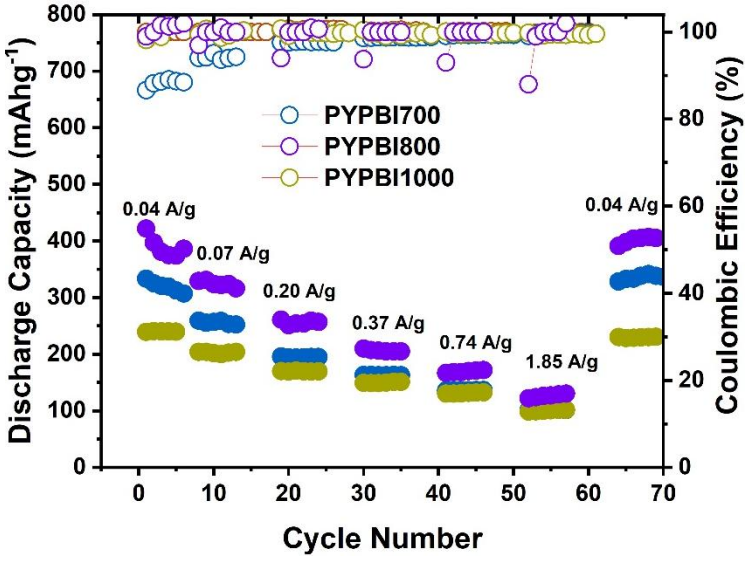

***Figure 10**: Comparison of rate studies of PYPBI700, 800 and 1000*

The XRD plots for PYPBIPA8.5-1.5, 7-3 and 5-5 as shown in Fig.11(a)(b)(c) respectively indicated a broad peak at 23.42,

23.71, 23.80° corresponding to 002 reflection. The d-spacing of the samples was calculated using Bragg's law which was found to be 3.80, 3.75 and 3.74 Å for

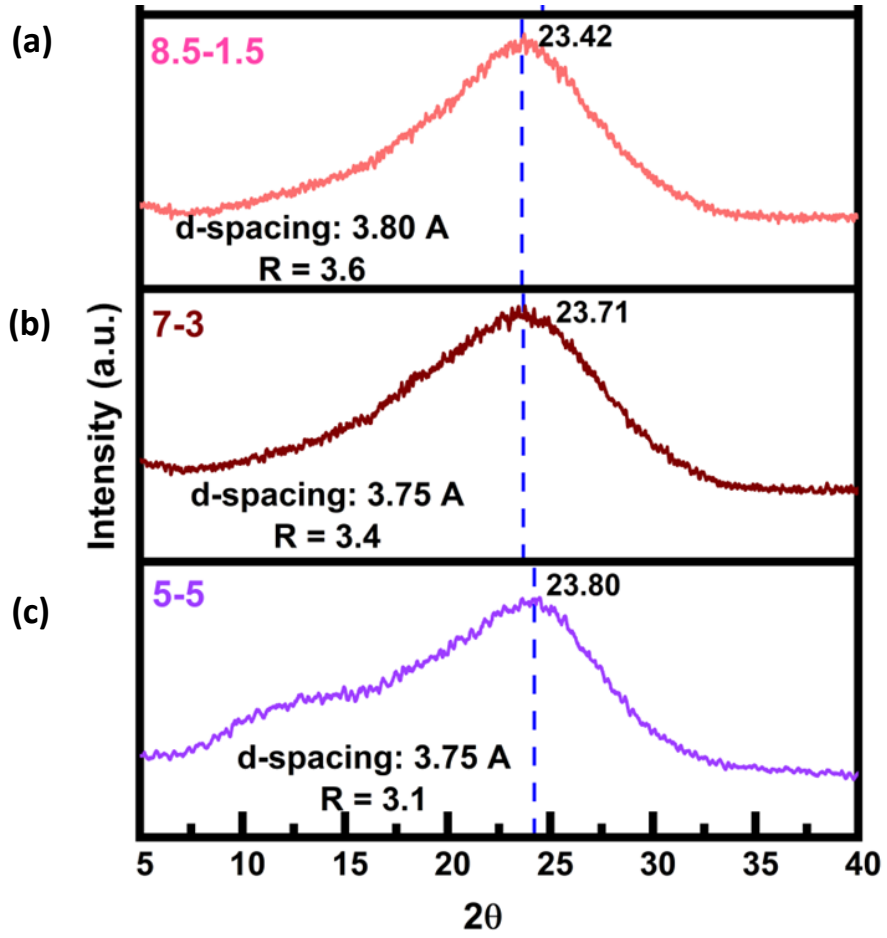

Figure 11: *Comparison of XRD of (a) PYPBIPA8.5-1.5 (b) PYPBIPA7-3 (c) PYPBIPA5-5*

PYPBIPA8.5-1.5, 7-3 and 5-5 in comparison to 3.6 Å for PYPBI800[8] as reported in our previous research work. PYPBI800 will be henceforth referred to as PYPBIPA10-0 as it was obtained by pyrolyzing pure polybenzimidazole without any polyamide group. Hence, these results clearly indicated that inclusion of oxygen alongside nitrogen led to increased d-spacing due to larger size of O atoms. Further, R-factor was also deduced using XRD plots which is an indicator of the relative number of carbon sheets arranged parallelly in a given crystal. R factor was calculated by dividing the ratio of background to ratio of signal which was found to be 3.2 in case of 10-0 and

in the order PYPBIPA8.5-1.5>7-3>5-5>10-0 (Fig. 11), thus indicating relatively more stacking of carbon sheets in case of PYPBI8.5-1.5 than others. This can be explained based on H-bonding strength between the adjacent chains of the polymers used for

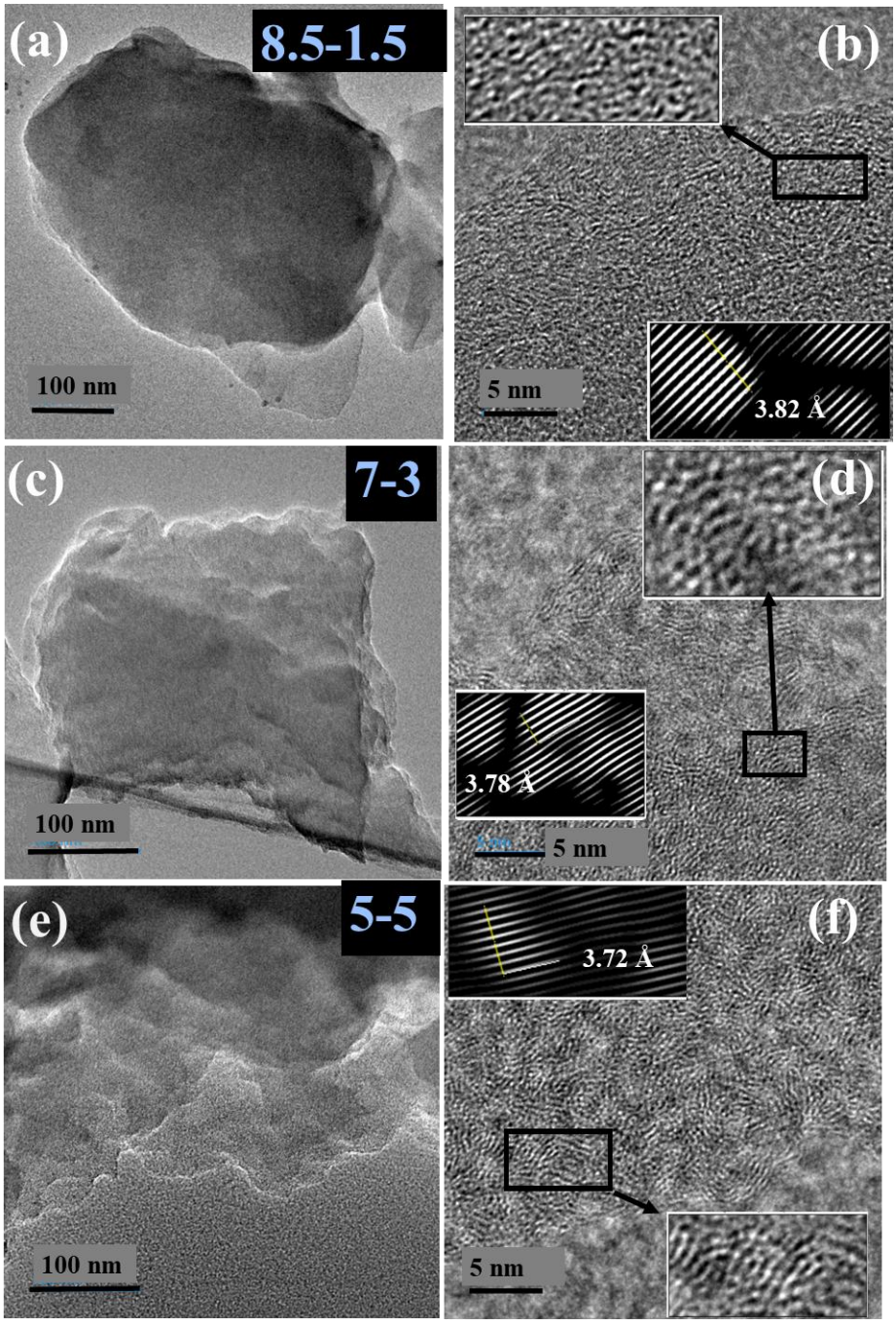

***Figure 12**: HR-TEM images of (a)100 nm (b) 5 nm of PYPBIPA 8.5-1.5 (c)100nm (d)5 nm of PYPBIPA7-3 (e)100nm (f) 5nm of PYPBIPA5-5*

synthesis of HCs. As reported by Kaneko et.al, incorporation of small amounts of amide groups to polybenzimidazole backbone enhanced interchain H-bonding strength between the adjacent chains[13]. This signified relatively weaker H-bonding in case of pure polybenzimidazole than the co-polymers. Also, according to their

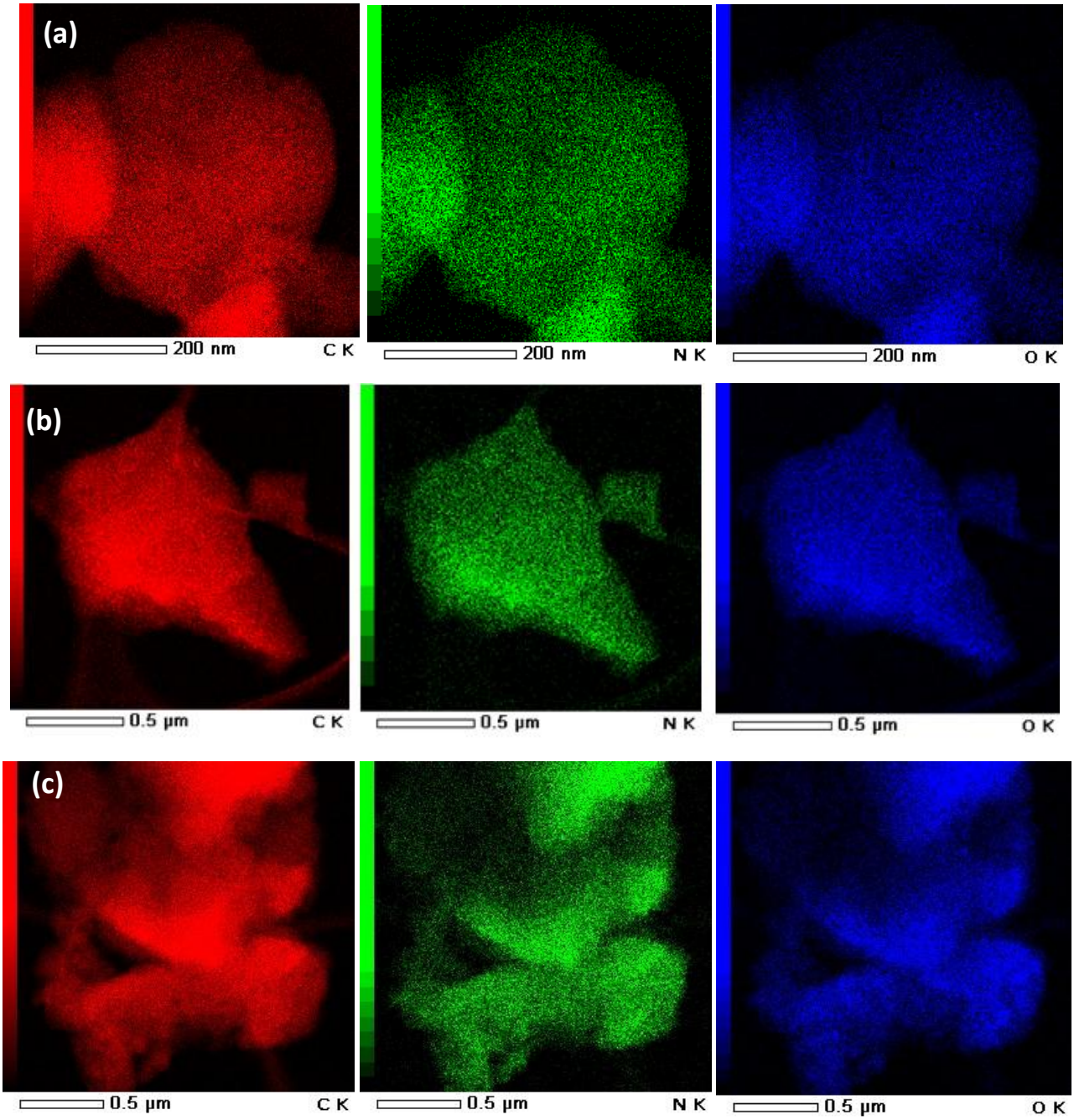

Figure 13: *TEM-EDX elemental mapping of (a) PYPBIPA8.5-1.5 (b) PYPBIPA7-3 (c) PYPBIPA5-5*

report, amide incorporation beyond a particular limit i.e., 20%, weakened the interchain H-bonding due to excessive amide groups that led to too many amide-imidazole and amide-amide interactions. This summarized the H-bonding strength of the co-polymers to be in the order PBIPA8.5-1.5>7-3>5-5. Thereafter upon pyrolysis, polymers with stronger H-bonding resulted in higher stacking of carbon planes which further led to greater R-factors. This explains the possible reason for similar trend of both R factor of carbon materials and H-bonding strength of the polymers. The higher stacking of carbon planes in the case of PYPBIPA8.5-1.5 can be another advantage for less hindered movement of Li-ion within the carbon material. The morphological analysis of PBIPA derived carbon materials was initially performed using HRTEM images. The HRTEM images at low magnification of 100nm indicated layered morphology in the case of all three samples as shown in Fig.12(a), (c) and (e). The high-magnification HR-TEM images at 5nm (zoomed inset of Fig. 12 (b) (d)and (f) indicated disordered arrangement of carbon planes for all three samples. To shed some more light on the spacing between the carbon planes, the associated HRTEM images were subjected to Fourier transform (FT) and inverse FT

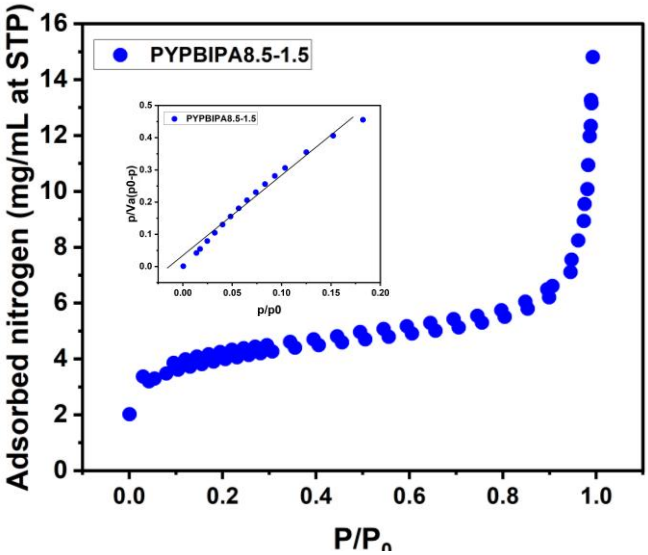

***Figure 14**: Adsorption-Desorption isotherm of PYPBIPA8.5-1.5*

(IFT) studies for determining the interplanar spacing, which was found to be 3.82, 3.78, 3.72 Å for PYPBIPA8.5-15, 7-3 and 5-5 respectively as shown in Fig. 15, which were in close agreement with the d-spacing determined using XRD. Further, TEM-EDX mapping of all three samples indicated uniform distribution of carbon, nitrogen and oxygen as indicated in Fig. 13 for PYPBIPA8.5-1.5,7-3 and 5-5 respectively. Nitrogen adsorption-desorption was conducted for PYPBIPA8.5-1.5 (Fig. 14) to evaluate the surface area and other physical parameters of the hard carbons. The surface area obtained by anlysing the BET plot of the isotherm was found to be 13.13 m^2/g. The isotherm was observed to be Type II indicating a relatively strong interaction between the sample surface and the adsorbate. To gain understanding of the defects present in both the materials, Raman spectroscopy was conducted

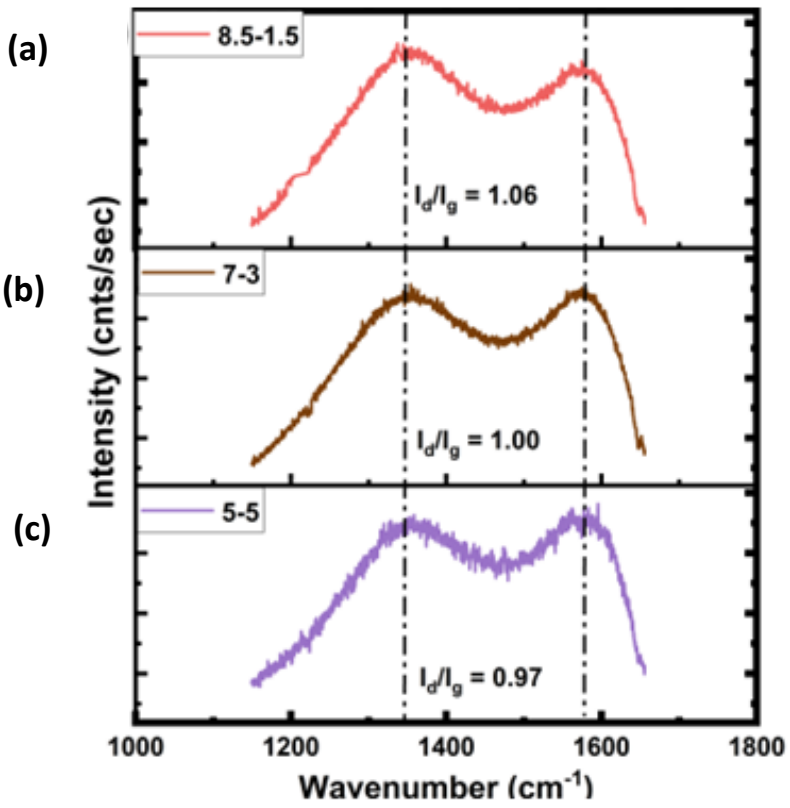

Figure 15: *Comparison of Raman spectra of PYPBIPA (a)8.5-1.5(b)7-3 (c)5-5*

(Fig. 15). The Raman spectra of all three samples exhibited two conventional peaks at similar Raman shifts of ~1350 cm^{-1} and ~1570 cm^{-1}, which can be identified as

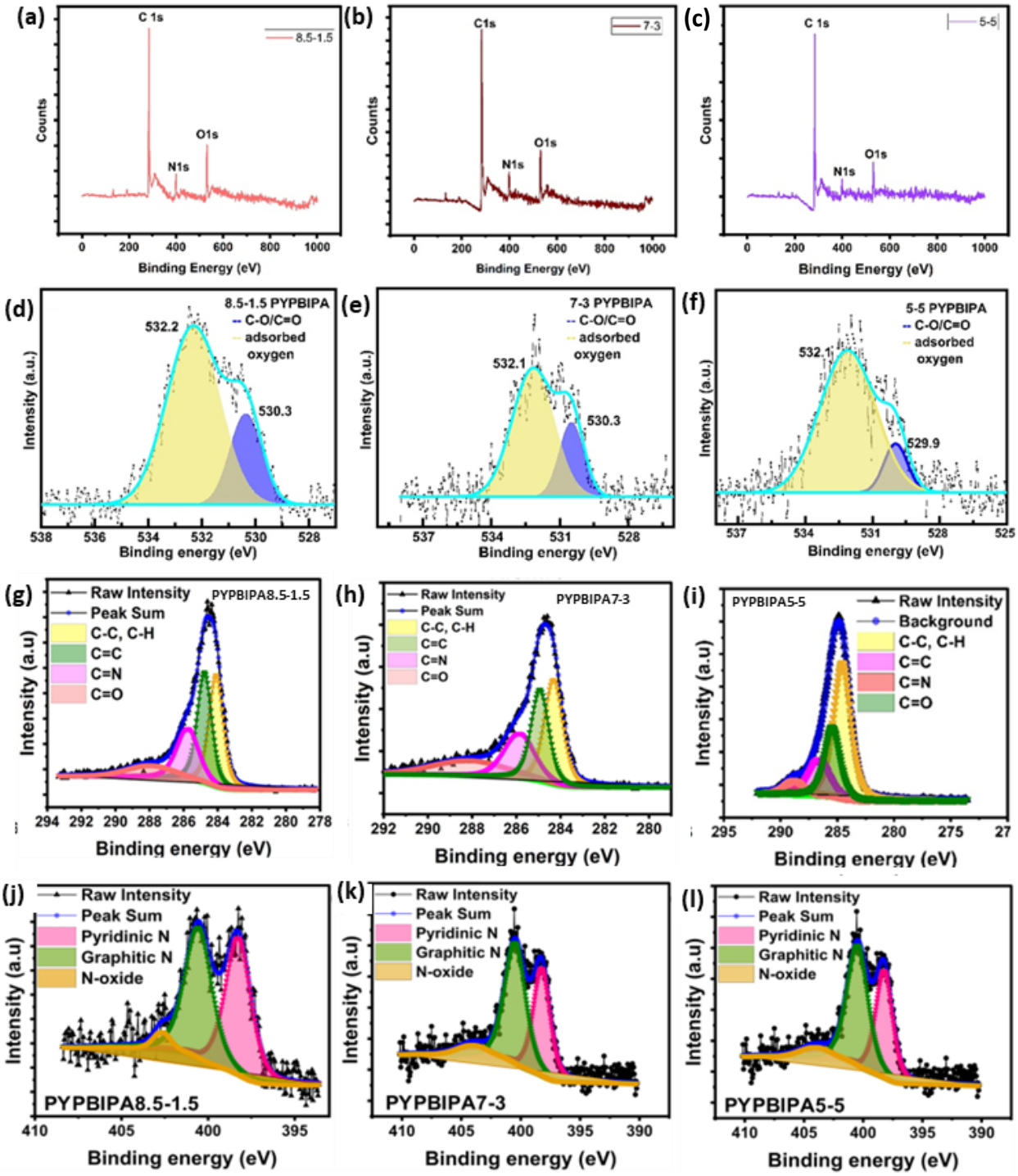

Figure 16: *Comparison of (a,b,c) XPS survey spectrum and deconvoluted (d,e,f) O1s (g,h,i) C1s (j,k,l) N1s XPS spectrum of PYPBIPA8.5-1.5, 7-3 and 5-5 respectively*

the D-band (defect-induced mode) and G-band (E_2g mode), respectively. The ratio of the D band to G band i.e., I_d/I_g ratio was found by dividing the integrated area under D peak to integrated area under G peak. The I_d/I_g ratios were found to be 1.06, 1.00 and 0.97 for PYPBIPA8.5-1.5, 7-3 and 5-5 respectively hence indicating a large number of defect sites in all three materials. The higher number of defect sites can be another advantage for PYPBI8.5-1.5 during fast charge-discharge as Li-ions can easily move from one plane to another plane in the perpendicular direction. Also, these defect sites can act as active sites for Li-ion adsorption. Elemental analysis was conducted using XPS which indicated the presence of carbon, nitrogen and oxygen in all three samples (Fig. 16). The content of nitrogen was determined to be 11.2, 9.9, 8.0 at% while the oxygen contents were found to be 13.1, 20.0, and 25.0 at% in PYPBIPA8.5-1.5, 7-3, and 5-5 respectively (Table 8). The nitrogen and oxygen contents in 10-0 were reported to be 14.8 at% and 0.6 at% respectively. The findings illustrated that the nitrogen content diminishes as the proportion of the polybenzimidazole group decreases, while the oxygen content rises with an increasing proportion of the polyamide group. Also, the poly(benzimidazole-co-amide) co-polymers acted as a single source of carbon, nitrogen as well as oxygen. The benzimidazole unit contains a benzene ring and an imidazole ring wherein the imidazole ring with covalently bonded nitrogen atoms can contribute towards nitrogen doping. The presence of these nitrogen-containing aromatic units confers polybenzimidazole backbone a high thermal resistance thereby leading to high nitrogen doping in the obtained carbon materials when pyrolyzed under inert atmosphere. Whereas polyamide with amide (NH-CO) functional group in its backbone can decompose more easily and most of the nitrogen is lost during carbonization resulting in oxygen doping in the remaining

***Table 8**: Nitrogen and oxygen doping contents in various carbon materials*

Carbon material	N at%	O at%
PYPBIPA10-0[8]	14.6	0.6
PYPBIPA 9-1	12.1	11.8
PYPBIPA8.5-1.5	11.2	13.1
PYPBIPA7-3	9.9	20.0
PYPBIPA6-4	9.2	21.8
PYPBIPA5-5	8.0	25.0
PYPBIPA0-10	2.6	31.3

carbon material. To substantiate the contributions of benzimidazole and amide units to the resultant carbon material, a homopolymer polyamide (PA) was synthesized and consequently subjected to pyrolysis henceforth referred to as PYPBIPA0-10. XPS analysis of PYPBIPA0-10 (Fig. 16c) indicated the content of nitrogen to be merely 2.6 at% and content of oxygen to be as high as 31.3 at%. These results clearly indicated that the benzimidazole unit primarily contributed to nitrogen doping, while the amide unit played a major role in oxygen doping. The benefits of nitrogen doping on fast charging performance of LIBs have been already discussed in our previous research work[8]. This study has been undertaken with the primary objective of elucidating the impact of oxygen doping in conjunction with nitrogen doping, particularly with respect to the fast-charging performance of the batteries. Compared to single heteroatom doping, co-doping makes significant contribution to electrical conductivity, interlayer spacing, and ion storage capacity due to the synergistic effects of both the elements. N doping can induce defect sites, introduce active sites for surface redox reactions, and facilitate electronic conductivity whereas O-doping creates oxygen based functional groups such as -C=O which can reversibly convert to -C-O upon lithiation thus increasing the gravimetric capacity through surface redox reactions[14]. Also, N and O doping can induce defect sites which can bind strongly with inserted Li-ions. Further, they can

be electron donors to the carbon planes thus inducing a strong bonding between the Li-ions and the graphene sheet. Indeed, both nitrogen (N) doping and the combined nitrogen and oxygen (N, O)-doping contribute to the enlargement of the d-spacing in carbon materials. This expanded d-spacing can facilitate the swift movement of Li-ions for insertion between the layers. To gain detailed understanding on the functional groups present in the carbon materials, the N1s, O1s and C1s spectra were deconvoluted for all three samples. Upon deconvolution, nitrogen was detected in three different forms shown in Fig. 16(j)(k)(l), i.e., pyridinic nitrogen, graphitic nitrogen, and N-oxide at 398±0.3eV, 400±0.3eV, and 402±0.3eV[15] which were in similar lines as 10-0 except for a minute content of pyrrolic nitrogen (0.50 at%)[8]. The deconvolution of O1s spectra indicated the presence of C-O/C=O, absorbed oxygen at 530±0.3, 532±0.3 eV respectively for all the samples as shown in Figure 16(d)(e)(f). The polarity of the C=O bond significantly enhances the Li-ion storage capacity by facilitating reversible redox reactions during lithiation and delithiation cycles. The redox process involving the carbonyl group and lithium ions can be summarized as $-C=O + Li^+ + e^- = -C-O-Li$[16]. Previous studies have investigated the interaction of C=O with Li-ions. One such study by Sun et.al demonstrated this using Density Functional Theory (DFT) to study lithiation and delithiation cycles in a modified covalent organic framework (COF) with azo and carbonyl groups. Their analysis, based on energy differences between the pristine and lithiated COF structures, revealed a preferential interaction of Li^+ ions with the C=O groups[17]. Additionally, they used in-situ Fourier Transform Infrared (FT-IR) spectroscopy which indicated an increase in C=O peak intensity with increasing state-of-discharge, suggesting Li-O bond formation. Furthermore, XPS measurements also indicated a new peak corresponding to Li-O bond formation in

addition to the existing C=O. While many studies have shown the effectiveness of oxygen-based functional groups in lithium storage applications, the high steric hindrance and reduced conductivity due to excessive O-doping can be a major drawback. Hence this research work has mainly focused on determining the optimal amount of oxygen in the anodic active materials suitable for fast charging of LIBs. Electrochemical studies were conducted using CR2025 type coin cells fabricated under Ar atmosphere (O_2 and H_2O < 0.5ppm). Initially, the batteries were subjected to cyclic voltammetry at a scan rate of 0.1mV/s as shown in Fig. 17(a)(b) and (c). The cyclic voltammograms of all three anodic half-cells indicated broad peaks which could be due to lithiation and delithiation of the disorderedly arranged carbon planes at wide range of potentials. Further, potentiostaic electrochemical impedance spectroscopy (PEIS) was conducted before and after cyclic voltammetry in order to compare the resistance[18] as shown in Fig. 17(d)(e) and (f). After cyclic

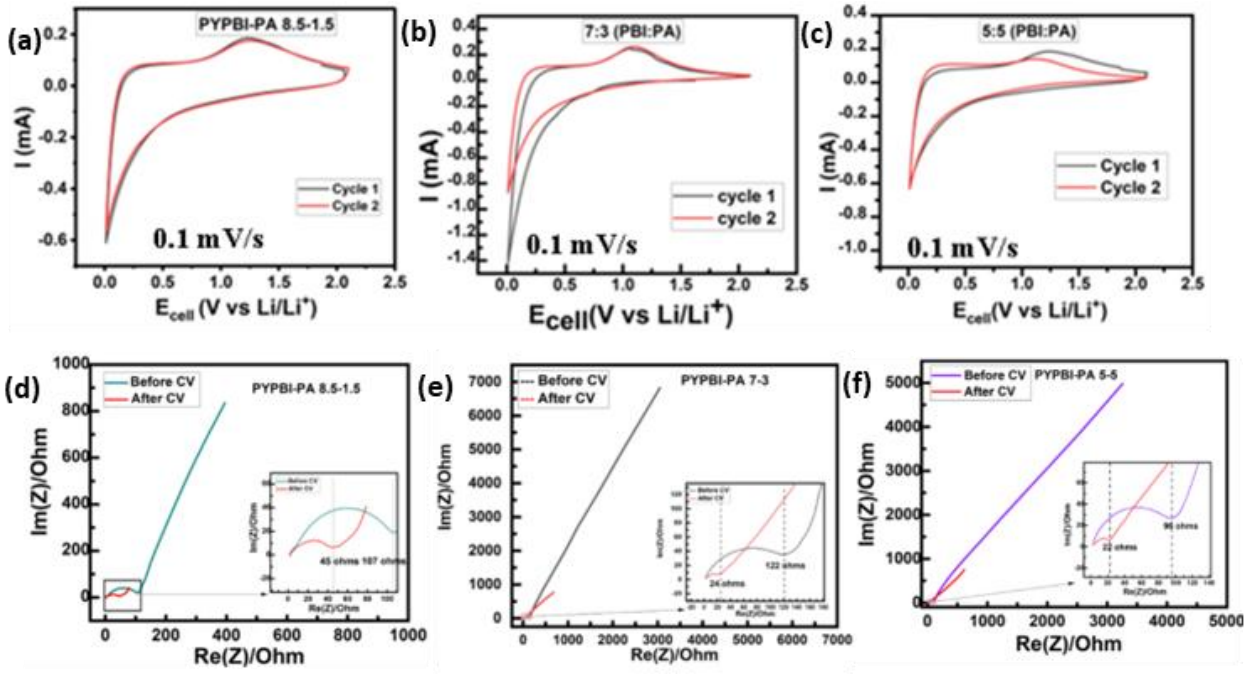

***Figure 17**: Cyclic voltammograms of (a)8.5-1.5 (b)7-3 (c)5-5 and electrochemical impedance spectrum of (d) 8.5-1.5 (e) 7-3 (f) 5-5*

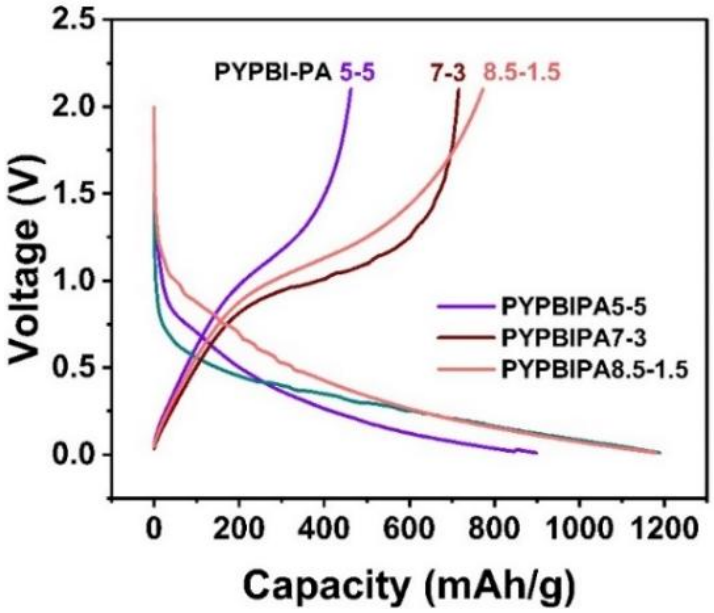

***Figure 18**: Initial charge-discharge plot for PYPBIPA8.5-1.5, 7-3, 5-5*

voltammetry, the resistance decreased drastically from 107 ohms to 45 ohms, 122 ohms to 24 ohms, and 96 ohms to 22 ohms in the case of PYPBIPA8.5-1.5, 7-3 and 5-5 respectively. The decrease in resistance observed after cyclic voltammetry (CV) can be ascribed to the development of a solid electrolyte interphase (SEI) at the electrode/electrolyte interface during cycling. This SEI formation facilitates more efficient charge transfer and enhances electrical conductivity[19]. The SEI formation consumes active lithium leading to overall loss of lithium. The first cycle discharge(lithiation)/charge(delithiation) capacities also clearly indicated SEI formation[20]. When cycled at a current density of 0.25 A/g as shown in Fig. 18, an initial coulombic efficiency (ICE) of 61, 60, and 51 % were obtained for PYPBIPA8.5-1.5, 7-3 and 5-5 respectively, which were comparatively lower than 68% ICE of 10-0. The lower ICE in the case of PYPBIPA derived carbons could be due to the presence of C-O bonds which react with Li-ions irreversibly[14], however the difference is quite low i.e. only 8%. Thereafter, galvanostatic charge discharge studies were performed for all three samples to obtain detailed understanding of

their electrochemical performance. All charge-discharge studies were conducted by maintaining same current densities during both lithiation and delithiation. As shown in Fig. 19(a), initially rate studies were performed and delithiation capacities of 600 mAh/g, 256 mAh/g, 199 mAh/g, 180 mAh/g, 140 mAh/g, 100 mAh/g were observed at 0.05 A/g, 0.40 A/g, 0.75 A/g, 1.00 A/g, 2.00 A/g and 4.00 A/g current densities for PYPBIPA8.5-1.5. Further, in case of PYPBIPA7-3, delithiation capacities of 500 mAh/g, 325 mAh/g, 204 mAh/g, 171 mAh/g, 90 mAh/g, 38 mAh/g were obtained at 0.05 A/g, 0.40 A/g, 0.75 A/g, 1.00 A/g, 2.00 A/g and 4.00 A/g respectively and in case of PYPBIPA5-5, delithiation capacities of 211 mAh/g, 147 mAh/g, 123 mAh/g, 64 mAh/g, 39 mAh/g were obtained at 0.05 A/g, 0.40 A/g, 0.75 A/g, 1.00 A/g, 2.00 A/g and 4.00 A/g current densities. At lower current densities of

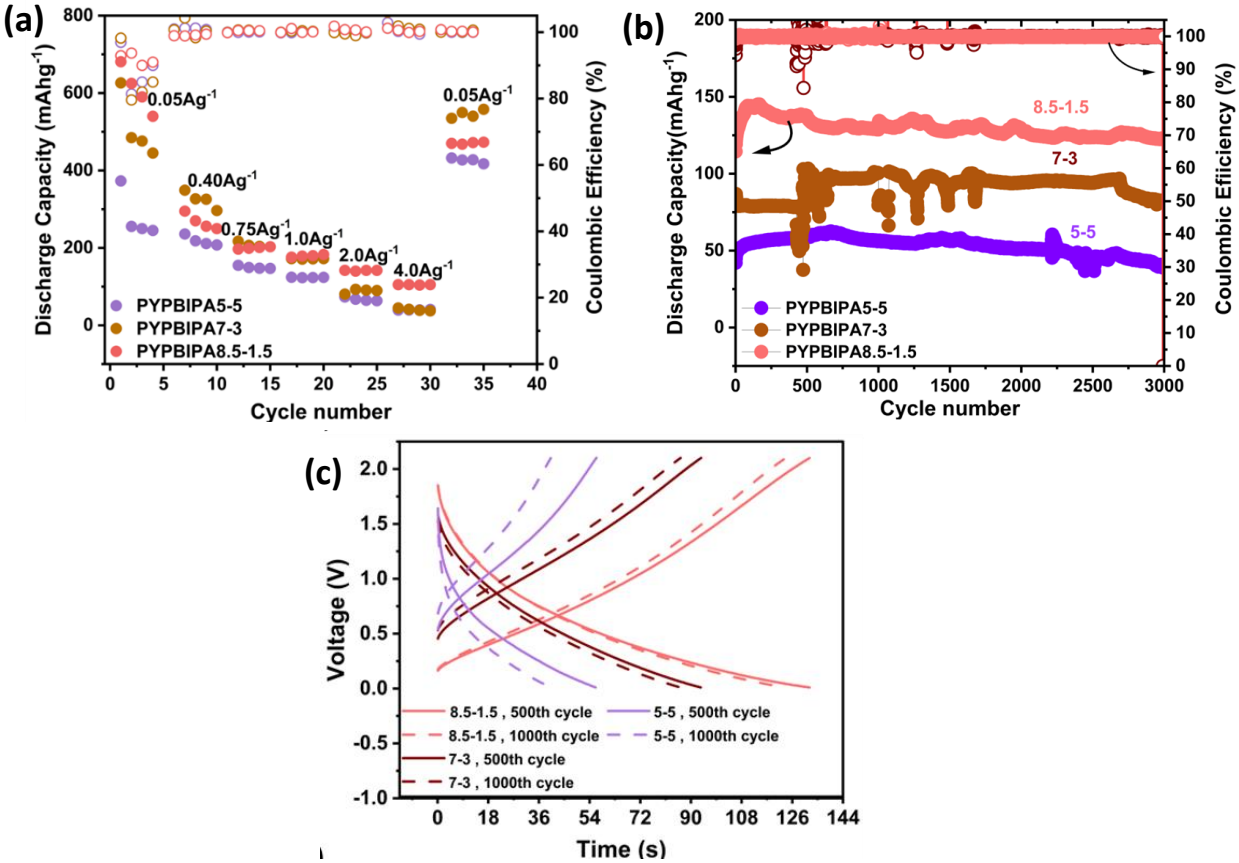

***Figure 19**: Comparison of (a) rate studies (b) long cycling (c) charge-discharge plots of PYPBIPA8.5-1.5, 7-3 and 5-5*

0.40, 0.75 A/g both PYPBIPA7-3 and PYPBIPA8.5-1.5 showed similar discharge capacities however at higher current densities of 2.0 and 4.0 A/g, PYPBIPA8.5-1.5 showed better performance. Furthermore, PYPBIPA8.5-1.5 outmatched 10-0[8] which showed discharge capacities of 206 mAh/g, 168 mAh/g, 125 mAh/g at 0.37 A/g, 0.74 A/g, 1.86 A/g respectively. Subsequently, to understand whether PYPBIPA8.5-1.5 can retain its high delithiation capability even during long cycling, charge discharge studies were conducted at 4.00 A/g for 3000 cycles as shown in Fig. 19(b). Even during long cycling, PYPBIPA8.5-1.5 showed much higher

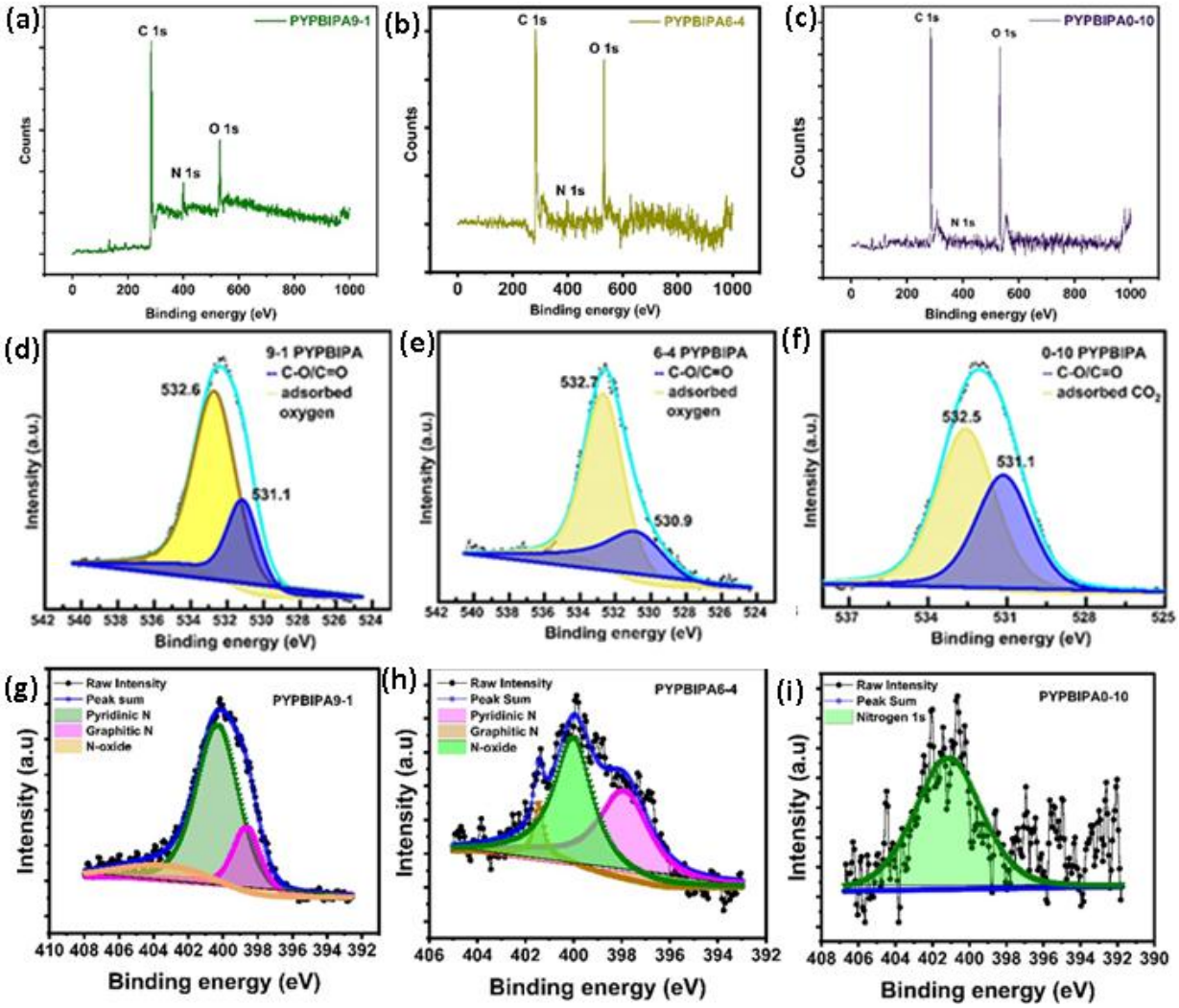

***Figure 20**: Comparison of (a) XPS survey spectrum (b) deconvoluted O1s spectrum (c)deconvoluted N1s XPS spectrum of PYPBIPA9-1, 6-4 and 0-10 respectively*

delithiation capacity of 135 mAh/g in comparison to 86mAh/g, 100 mAh/g, 60 mAh/g for PYPBIPA10-0, 7-3, 5-5 respectively. The GCD plots during cycling are shown in Fig. 19c. The charge-discharge plots of these materials as shown in Fig. 19c clearly indicate a sloping region throughout the voltage window. Therefore, an adsorption-type Li-ion storage mechanism can be proposed for these materials which is very common in case of heteroatom doped hard-carbons[21]. Even in terms of capacity retention, PYPBIPA8.5-1.5 surpassed others. The capacity retention of PYPBIPA8.5-1.5 after 1000 cycles was found to be 95%, after 2000 cycles was 93% and after 3000 cycles it was 90% which is commendable whereas the capacity retention in case of 7-3 was 83.3%, for 5-5 it was 65.5% after 3000 cycles. PYPBIPA8.5-1.5 with an optimum balance of nitrogen and oxygen contents outperforms all others during rate studies as well as long cycling. From the long cycling studies, in terms of rate capability, reversible capacity and capacity retention, following trend was observed 8.5-1.5>7-3>5-5. To further validate this decreasing trend of parameters with increasing polyamide composition, carbon materials from intermediate polyamide compositions such as 9-1 (intermediate to 100-0 and 8.5-1.5) and 6-4 (intermediate to 7-3 and 5-5) were synthesised and applied as anodic

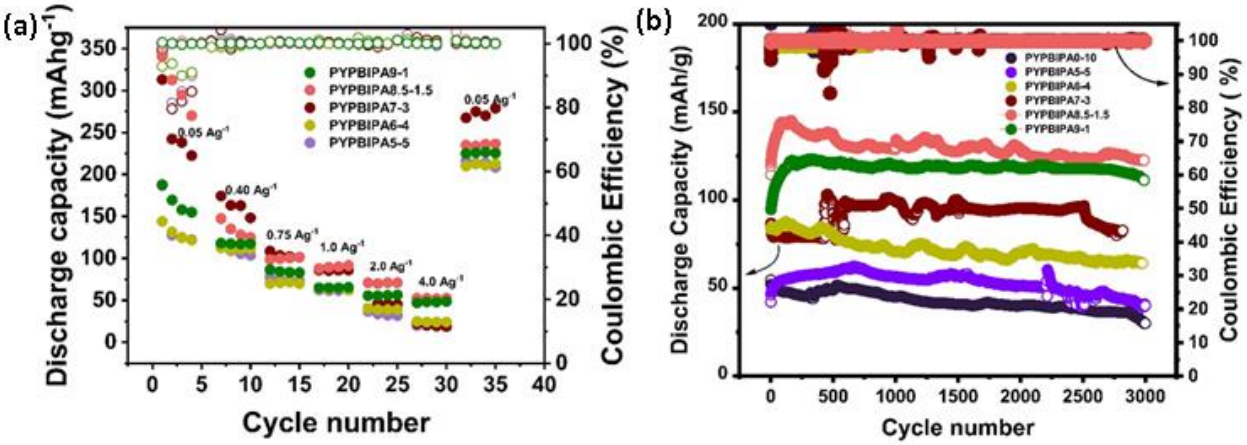

***Figure 21**: Comparison of (a) rate studies (b) long cycling of PYPBIPA9-1, 8.5-1.5, 7-3, 6-4 and 5-5*

active materials in LIBs. XPS analysis of these carbon materials is summarized in Fig. 20. The deconvoluted N1s, O1s, and C1s spectra of PYPBIPA9-1 and PYPBIPA6-4 are presented in Fig. 20 respectively. A comparison of rate studies and long cycling of these anode materials is shown in Fig. 21 (a) and Fig. 21(b) respectively. During rate studies, PYPBIPA9-1 exhibited discharge capacities of 316, 235, 167, 130, 111, and 94 mAh/g at current densities of 0.05 A/g, 0.40 A/g, 0.75 A/g, 1.00 A/g, 2.00 A/g, and 4.00 A/g, respectively. PYPBIPA6-4 showed discharge capacities of 262, 222, 140, 130, 80, and 48 mAh/g at current densities of 0.05 A/g, 0.40 A/g, 0.75 A/g, 1.00 A/g, 2.00 A/g, and 4.00 A/g. During long cycling studies at 4.0 A/g, PYPBIPA9-1 delivered a discharge capacity of 122 mAh/g with a capacity retention of 90%, whereas PYPBIPA6-4 delivered 74 mAh/g with a capacity retention of 76%. Furthermore, the difference in discharge capacities between PYPBIPA9-1 and PYPBIPA8.5-1.5 was observed to be minimal i.e. 13 mAh/g, attributed to similar capability, reversible capacity, and capacity retention was consistent even with the inclusion of 9-1 and 6-4 among 8.5-1.5, 7-3, and 5-5 compositions. These results underscore the critical role of optimizing nitrogen and oxygen doping levels, as

Table 9: *Comparison of rate studies of PYPBIPA10-0, 9-1, 8.5-1.5, 7-3, 6-4, 5-5 and 0-10*

Current density (A/g)	Capacity (mAh/g)						
	10-0	9-1	8.5-1.5	7-3	6-4	5-5	0-10
0.05	-	330	600	500	250	270	280
0.40	206	235	256	325	220	211	152
0.75	168	167	199	204	140	147	125
1.0	-	130	180	171	128	123	113
2.0	125	111	140	90	80	64	85
4.0	-	94	100	38	48	39	55

shown by PYPBIPA9-1 and PYPBIPA8.5-1.5, to achieve high performance, especially under high current rate conditions (Table 9). Following this, symmetric cells were fabricated using PYPBIPA5-5, PYPBIPA6-4, PYPBIPA7-3, PYPBIPA8.5-1.5 and PYPBIPA9-1 active materials. Electrochemical studies using symmetric cells enable the understanding of parasitic reactions which lead to capacity loss after cycling. In a typical anodic half-cell, lithium loss due to parasitic reactions does not necessarily translate into loss of capacity as the lithium inventory is high[22]. Further in full cells, due to the applied potential window, oxidative side reactions on the cathodic side affect the capacity retention. Hence in both cases of anodic half-cells and full cells, understanding of anode is difficult. In this regard, symmetric cells enable deeper understanding of the anode (or electrode of interest) as the lithium inventory is limited and there is very limited scope for parasitic reactions involving electrolyte in the potential window -/+ 0.5V[22]. The symmetric cell charge-discharge studies of PYPBIPA5-5, 7-3, 6-4, 8.5-1.5 and 9-1 were conducted and the results thereof

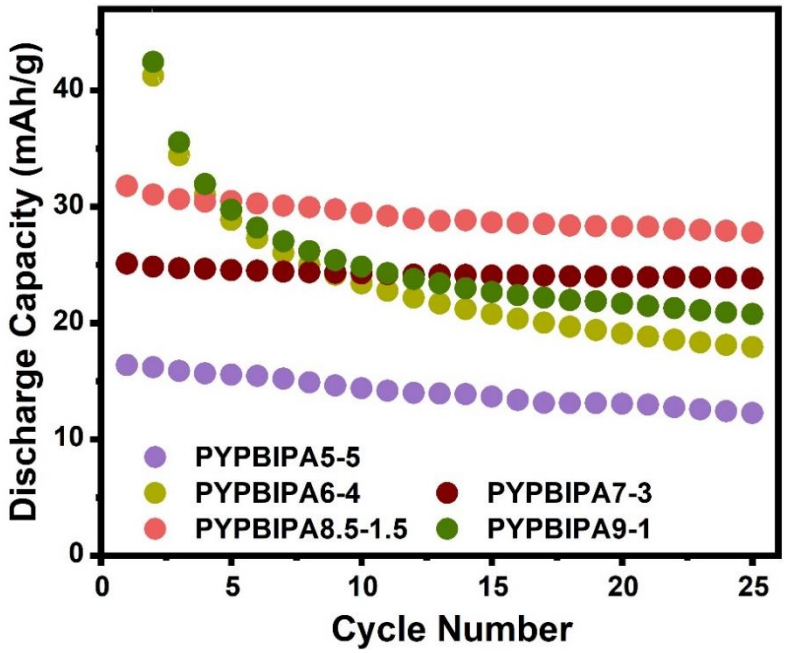

***Figure 22**: Long cycling plot for symmetric cells of PYPBIPA9-1, 8.5-1.5, 7-3, 6-4, and 5-5*

indicated that PYPAPBI8.5-1.5 exhibited stable cycling behaviour (Fig. 22) with the highest capacity retention of 91.3% after 25 cycles, amongst others. This is consistent with the stable cycling behaviour observed in the long cycling studies of the anodic half-cell. Hence, these results clearly indicate that PYPBIPA8.5-1.5 shows the best performance amongst others (Fig. 22). Furthermore, to gain detailed understanding on the effect of oxygen on charge-discharge performance, pyrolyzed polyamide homopolymer (henceforth referred to as PYPBIPA0-10) based anodes were also subjected to studies. The XPS analysis and charge-discharge performance (rate studies and long cycling) of PYPBIPA0-10 are shown in Fig. 20(c,f,i) and 24 respectively. The XPS analysis of PYPBIPA0-10 indicated the content of N to be 2.6 at% and O content to be 31.3 at% in comparison to 14.6 at% of nitrogen doping and 0.6 at% of oxygen doping in PYPBIPA10-0. The impact of N and O contents is directly reflected on the performance of the battery. As we can observe from rate studies

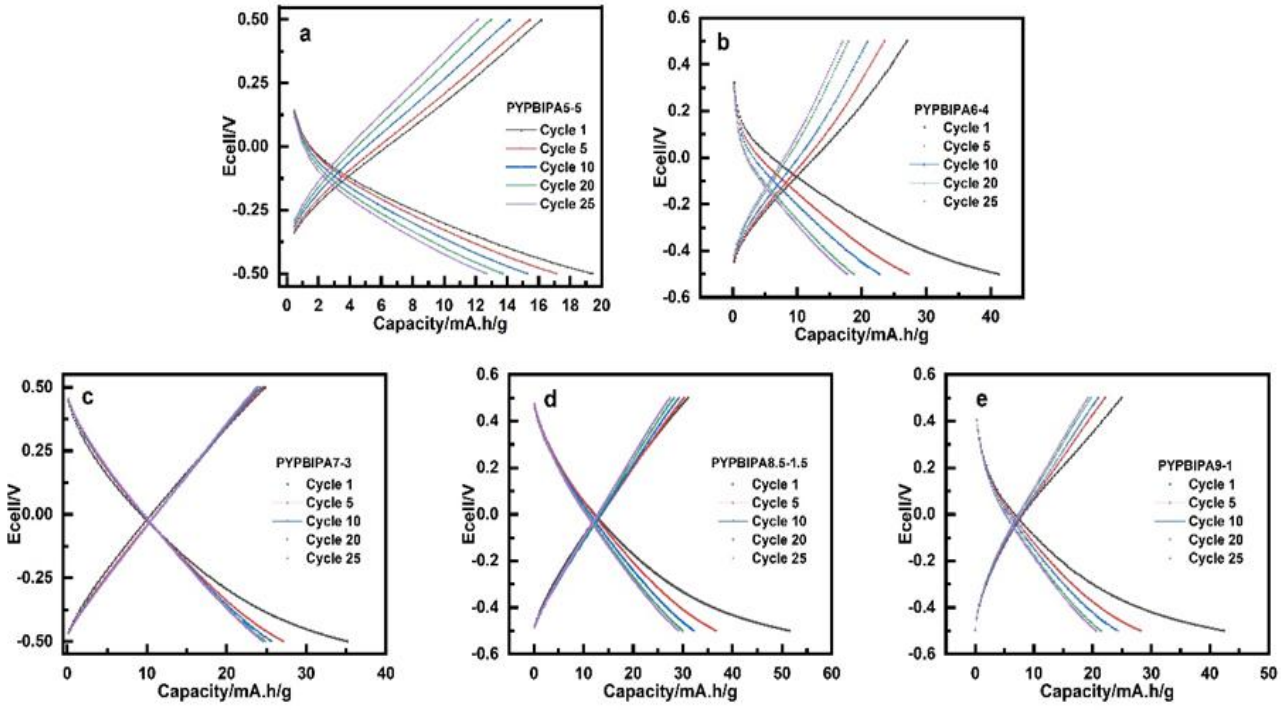

***Figure 23**: Voltage vs capacity plots for PYPBIPA (a)5-5 (b)6-4 (c)7-3 (d)8.5-1.5 and (e)9-1 symmetric cells*

in Fig.24(a), PYPBIPA0-10 delivered discharge capacities of 152, 125, 85 mAh/g in contrast to 206, 168 and 125 mAh/g for PYPBIPA10-0 at 0.4, 0.75 and 2.0 A/g (Table 10). Furthermore, long cycling at 4.0 A/g indicated a discharge capacity of 51 mAh/g in case of PYPBIPA0-10 whereas it was reported to be 86 mAh/g in case of PYPBIPA10-0. These results clearly indicated that PYPBIPA10-0 with maximum nitrogen doping shows better performance than PYPBIPA0-10 with maximum oxygen doping in terms of discharge capacity as well as long cycling ability. Compared to PYPBIPA8.5-1.5, 7-3, and 5-5, PYPBIPA0-10 exhibits inferior discharge capacity and unsatisfactory cycle performance (Fig. 24(b)). The reason could be excessive oxygen doping. An increase in oxygen content leads to disadvantages,

***Table 10**: Comparison of rate studies PYPBIPA10-0, 9-1, 8.5-1.5, 7-3, 6-4, 5-5, 0-10*

Carbon material	Discharge capacity (mAh/g)	Capacity retention (%)
PYPBIPA 9-1	122	90
PYPBIPA8.5-1.5	137	90
PYPBIPA7-3	100	83
PYPBIPA6-4	84	76
PYPBIPA5-5	60	65
PYPBIPA0-10	51	59

as it can result in irreversible capacity loss, leading to poor cycle performance, specifically low-capacity retention. This phenomenon is evident in the cases of PYPBIPA5-5 and 0-10. As mentioned earlier, PYPBIPA8.5-1.5 outperformed 10-0 due to the co-doping effect of oxygen alongside nitrogen. However, this favourable effect is not observed in the cases of PYPBI7-3, 5-5, and 0-10. It's noteworthy that PYPBIPA0-10, despite having a high level of oxygen doping, was unable to rival the

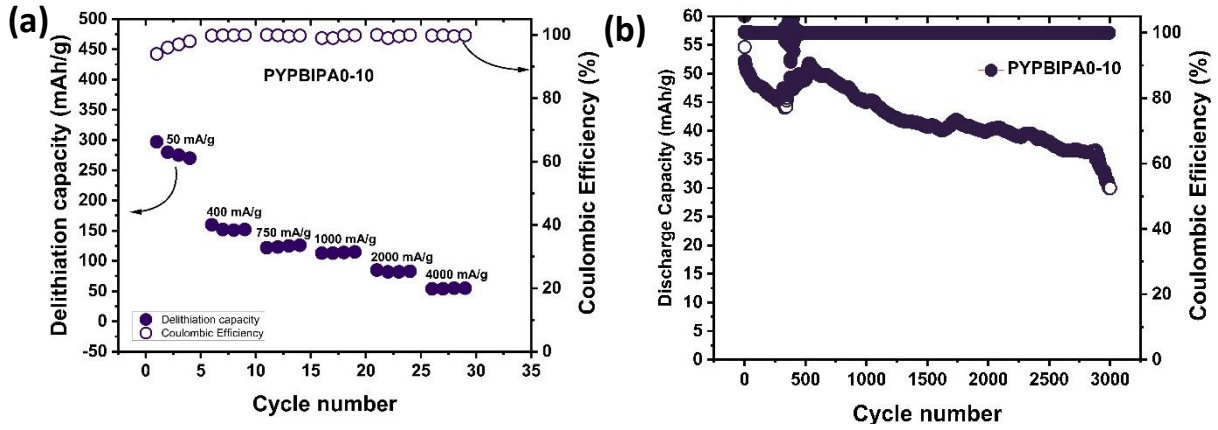

Figure 24: *(a) Rate studies (b) long cycling for PYPBIPA0-10*

performance of PYPBIPA10-0 and other carbon materials. While oxygen co-doping can offer advantages, this study noted that an increase in polyamide content beyond 15% for obtaining N, O co-doped carbons had a detrimental effect on battery performance. This is attributed to steric hindrance caused by the bulky oxygen groups, impeding the diffusion of lithium-ions and consequently, resulting in diminished electrochemical performance. These results clearly indicated PYPBIPA8.5-1.5 as the best-performing material amongst others, demonstrating both rapid charge-discharge capabilities and long cycling capability. In this context, it's crucial to highlight that while oxygen (O) co-doping contributes significantly to the fast-charging performance of batteries, achieving an optimal balance between both the elements is essential. Further, to understand the mechanism of charge storage, kinetic studies were conducted using cyclic voltammetry at scan rates of 0.1, 0.3, 0.5, 0.7, and 1.0 mV/s for all three samples. The cyclic voltammograms of all three samples are shown in Fig. 25 (a)(b) and (c). Power law

$$i = av^b \text{ ---------- equation } 1^{23}$$

was utilized wherein i signifies current, v signifies scan rate. The value of a and b are obtained from the intercept and slope of log i vs. log v plot respectively. The linear fit of the logarithmic plots of all three samples are shown in Fig. 25(d)(e) and (f).

The value of b determines whether a diffusion-controlled charge storage mechanism is dominant, or a capacitive controlled charge storage mechanism is dominant. When the value of b=0.5, a diffusion-controlled mechanism is known to

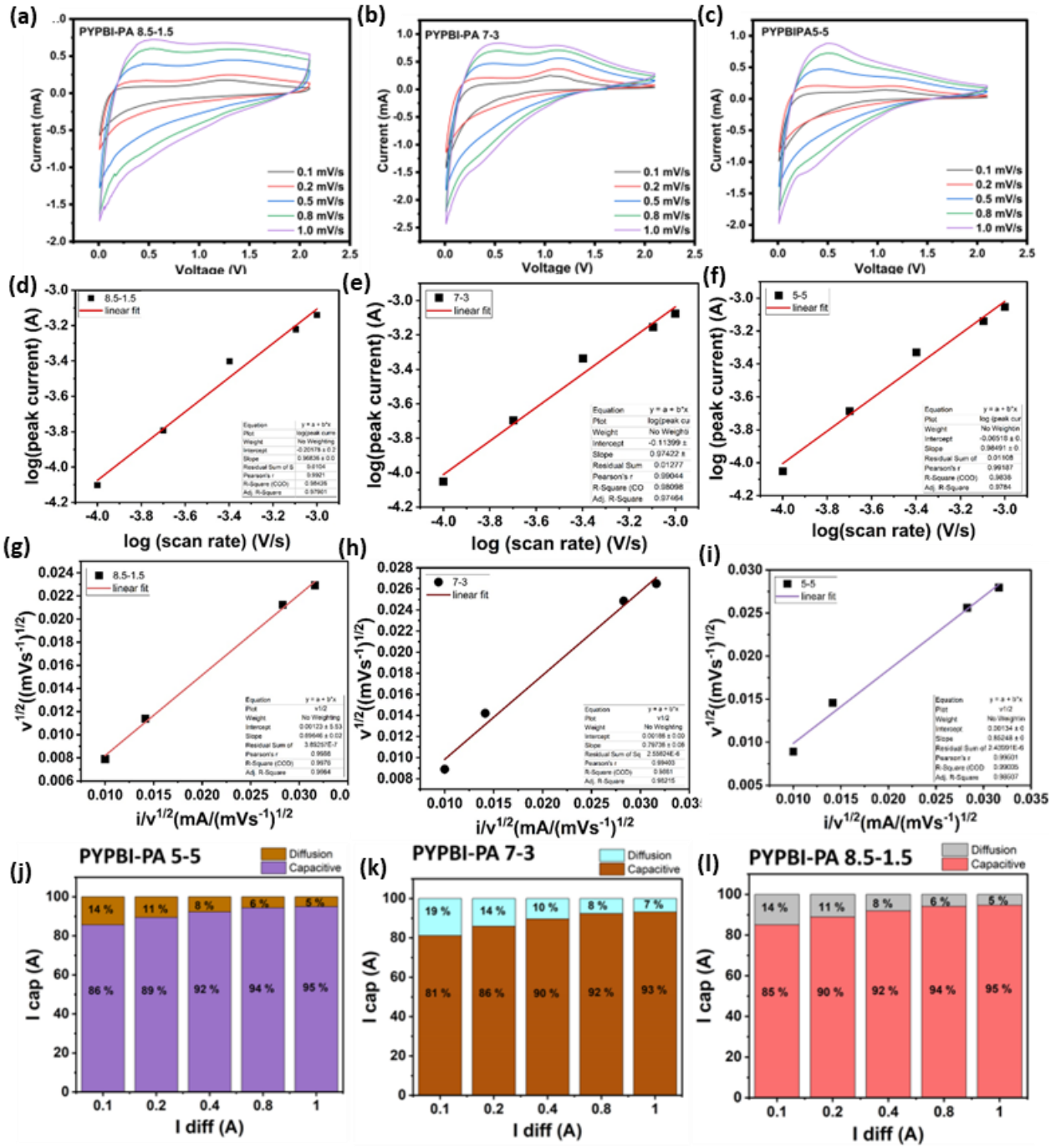

Figure 25: *(a,b,c) Cyclic voltammetry scan rate studies (d,e,f) linear fit of logi vs logv (g,h,i) linear fit of $i/v^{1/2}$ vs $v^{1/2}$ (j,k,l) percentage of diffusion based and capacitive based charge storage currents for PYPBIPA8.5-1.5, 7-3 and 5-5 respectively.*

happen whereas when the value of b=1.0, a surface controlled capacitive charge storage mechanism is known to happen. In case of PYPBIPA8.5-1.5, 7-3 and 5-5, the values of b were found to be 0.98, 0.97 and 0.97 respectively which was higher than the b value of 0.90 in case of 10-0. These results suggest that a substantial capacitive-controlled charge storage mechanism predominated over a diffusion-controlled mechanism for all the carbon samples. The value of b was constantly higher in all N and O co-doped carbons than purely N doped carbon which could be due to availability of large number of surface redox sites in N, O co-doped carbons. Furthermore, in order to quantitatively distinguish the capacitive and diffusion charge storage contributions,

$$i = k_1 v + k_2 v^{1/2} \text{----------equation } 2^{23}$$

was used wherein the redox current i is a cumulative measure of the capacitive based charge storage k_1v and diffusion-based charge storage $k_2v^{1/2}$ at each scan rate. k_1 and k_2 values were determined using a linear fit of $i/v^{1/2}$ vs $v^{1/2}$ as shown in Fig. 25 (g) (h) and (i) for all three carbon materials. Upon calculation of capacitive based current and diffusion based current contributions, it was found that all three samples show major contributions to capacitive based currents at all scan rates. The percentage contribution of capacitive current was found to be 85%, 90%, 92%, 94% and 95% for PYPBIPA8.5-1.5 whereas it was found to be 81%, 86%, 90%, 92%, and 93% in case of 7-3, and 86%, 89%, 92%, 94% and 95% in case of 5-5 at 0.1, 0.2, 0.4, 0.8, and 1.0 mV/s respectively as shown in Fig. 25 (j) (k) and (l). Capacitive current contributions were reported to be 78, 86, 89, 91 and 92% at 0.1, 0.2, 0.4, 0.8, and 1.0 mV/s respectively for 10-0. The above results clearly demonstrated that the capacitive current contribution was constantly higher in case of co-doped carbons than purely nitrogen doped carbon at all scan rates thus indicating that inclusion of

oxygen along with nitrogen led to increased number of surface redox sites. Although the contribution from diffusion-based charge storage was relatively low, it was still evident.

Though the O content was observed to be higher in PYPBIPA7-3 and 5-5 implying the presence of a greater number of active sites for surface redox reactions, they couldn't show higher delithiation capacities than PYPBIPA8.5-1.5 since the bulky O groups would have reduced Li-ion diffusion within the carbon planes. To validate this, lithium-ion diffusion coefficient was calculated using dynamic electrochemical

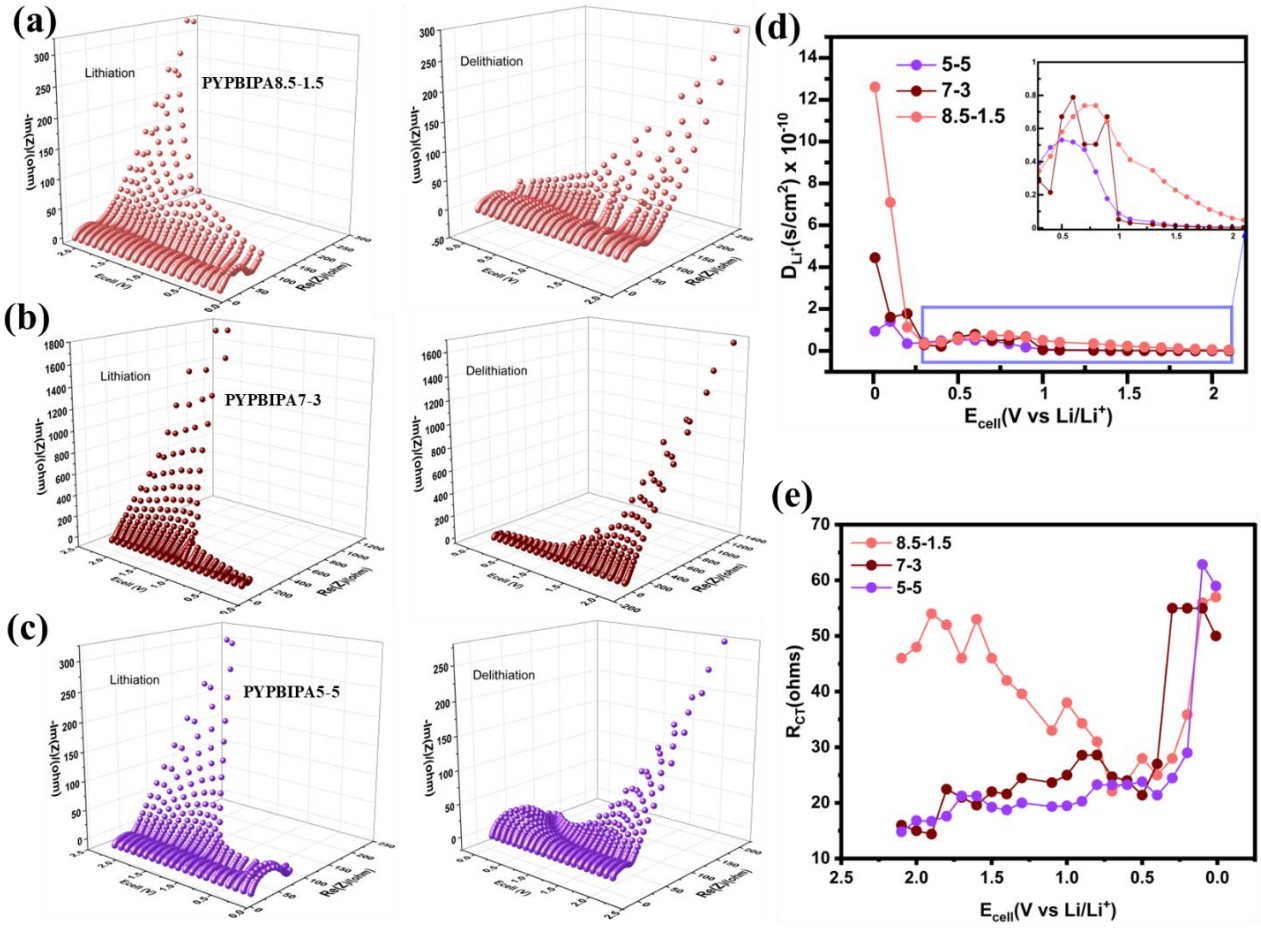

Figure 26: *DEIS plots for lithiation(left) and delithiation(right) for PYPBIPA (a)8.5-1.5 (b)7-3 (c) 5-5 (d) comparison of lithium-ion diffusion coefficient (e)comparison of charge transfer resistance for PYPBIPA8.5-1.5, 7-3 and 5-5 in voltage range of 2.1 to 0.01V during lithiation.*

impedance spectroscopy (DEIS) in the potential range of 0.01 V to 2.1 V for PYPBIPA8.5-1. 5, 7-3 and 5-5 as shown in Fig. 26. (a) (b) (c). The DEIS profiles of all three carbon materials show typical behaviour i.e., a semicircle in the high frequency region followed by a straight line in the low frequency region[24]. Lithium-ion diffusion coefficient(D_{Li^+}) was evaluated with the impedance data obtained at lower frequencies using the following Warburg equation,

$$D_{Li^+} = \frac{R^2T^2}{2A^2n^4F^4C^2\sigma^2} \quad \text{..... equation } 3^{25}$$

Where R is universal gas constant, T is temperature in kelvin, A is area of the electrode (cm^2), n is number of electrons transferred, F is faradays constant, C is concentration of electrolyte and σ is Warburg coefficient. Warburg coefficient is evaluated using the following equation,

$$Z_{real} = \left(R_{Electrolyte} + R_{CT}\right) + \sigma\omega^{-0.5} \text{..... equation } 4^{26}$$

Where Zreal is real impedance and ω is angular frequency. The angular frequency ω is calculated as 2πf where f corresponds to the values of frequency at the low frequency region. Fig. 26(d) provides a comprehensive comparison of the lithium-ion diffusion coefficient for all three samples during lithiation at each potential within the range of 0.01 to 2.1V. The lithium-ion diffusion coefficient was observed to be highest in the case of PYPBIPA8.5-1.5, following the order PYPBIPA8.5-1.5 > 7-3 > 5-5. As previously discussed, this data corroborates the impact of excessive oxygen doping, wherein the presence of bulky oxygen groups increased the steric hindrance and consequently, ion diffusion diminished in PYPBIPA7-3 and 5-5. At faster current rates, which is marked by a significant influx of Li-ions, the diminished lithium-ion diffusion translated into a lower Li-ion storage capability in PYPBIPA7-3 and 5-5. Furthermore, the comparison also clarified that there was no significant

difference in diffusion coefficients of PYPBIPA7-3 and 5-5 in between 1V and 2.1V. However, beyond 1V down to 0.01V, there was an increase in the lithium-ion diffusion coefficient for PYPBIPA7-3. This suggests that, in the case of PYPBIPA7-3, lithiation becomes more favourable within the range of 0.01 to 1V. In contrast, for PYPBIPA8.5-1.5, the lithium-ion diffusion coefficient remained significantly high across the entire potential range of 0.01 to 2.1V. This resulted in a notably elevated lithium-ion storage capability, even at a very high current density of 4.0 A/g. Further, upon fitting the EIS, the charge-transfer resistance which is generally observed at high frequencies were obtained for all three samples in the potential range of 0.01V to 2.1V during lithiation. Fig. 26(e) showcases plots on comparison of charge-transfer resistances for all three samples during lithiation. The charge transfer resistance was observed to be maximum for PYPBIPA8.5-1.5 followed by PYPBPA7-3 and PYPBI5-5. This could be due to differences in oxygen doping content. In general, oxygen being highly polar facilitates charge transfer. Hence, PYPBIPA5-5 containing maximum oxygen content faces relatively least resistance, whereas PYPBIPA8.5-1.5 with minimum oxygen content encounters relatively higher resistance, while PYPBIPA7-3 with an intermediate oxygen content faces intermediate resistance. Taking a holistic view, it becomes evident that while PYPBIPA8.5-1.5 exhibits a slightly higher charge transfer resistance owing to its lower oxygen content, this is effectively compensated for by faster lithium-ion diffusion rate. This compensation is clearly reflected in its superior fast-charging capability. Additionally, a slurry with increased acetylene black content was prepared using a composition ratio of 7:1:2 for the active material, binder, and acetylene black, respectively, compared to the previously used ratio of 8:1:1. The

slurry was coated onto copper foil, and the electrodes were calendared to a thickness of 0.1 mm. After punching and weighing, the electrodes were assembled into cells following the same fabrication procedure as previously described. The assembled batteries were subjected to long-term cycling tests (Fig. 27) at a current density of 4000 mA g^{-1}. An initial discharge capacity of 158 mAh g^{-1} was achieved, which was higher than that of cells with lower acetylene black content, likely due to enhanced electrical conductivity. However, the discharge capacity gradually decreased to 119 mAh g^{-1} after 513 cycles, corresponding to a capacity retention of 74% after 500 cycles. This decline may be attributed to the highly porous nature of acetylene black, which, despite improving conductivity, can trap lithium ions and lead to irreversible capacity loss over extended cycling. Further, the coin cells cycled for 3000 cycles were decrimped inside Ar filled glove box. X-rays can penetrate up to 10nm of material surface, hence they can easily detect the SEI components which are generally present within this limit. Thus, the cycled anodes were further subjected to XPS for understanding the various components of SEI. The initial XPS

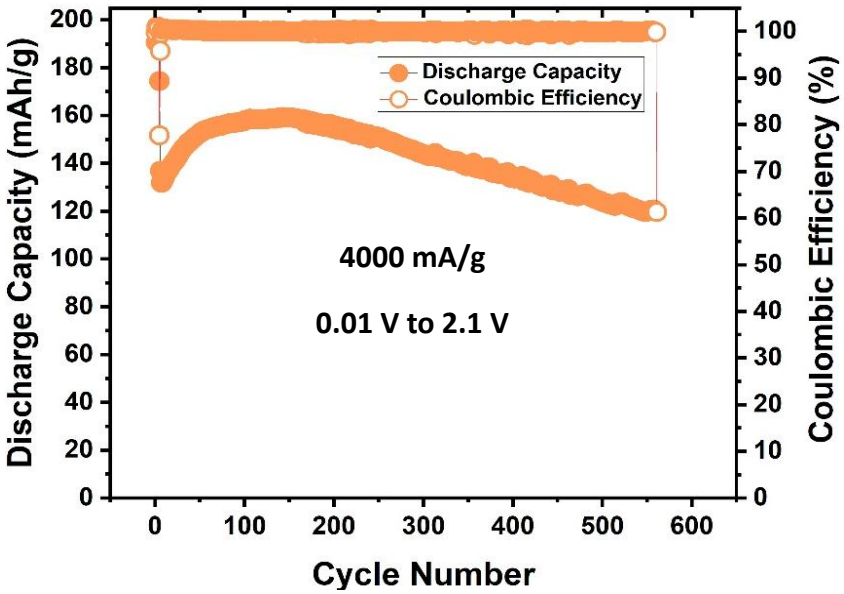

***Figure 27**: Long cycling studies of PYPBIPA8.5-1.5 with increased acetylene black ratio*

survey spectrum detected C, O and F in the case of all three cycled anodes. Further deconvolution was performed for understanding the various functional groups present. The deconvoluted C1s spectra of cycled PYPBIPA8.5-1.5 anode (Fig. 28(a)) showed peaks at 285.8 eV, 287.5 eV, 289.5 eV, and 290.8eV corresponding to C=C, C=O/C-O, Li_2CO_3 and C-F respectively[27]. The O 1s spectra (Fig. 28(b)) showed peaks at 532.7 eV, 533.3 eV corresponding to C=O, C-O-C. The F 1s spectra (Fig. 28(c)) showed peaks at 685.8, and 687.9 eV corresponding to LiF and Li_xPF_y[28,29]. The XPS

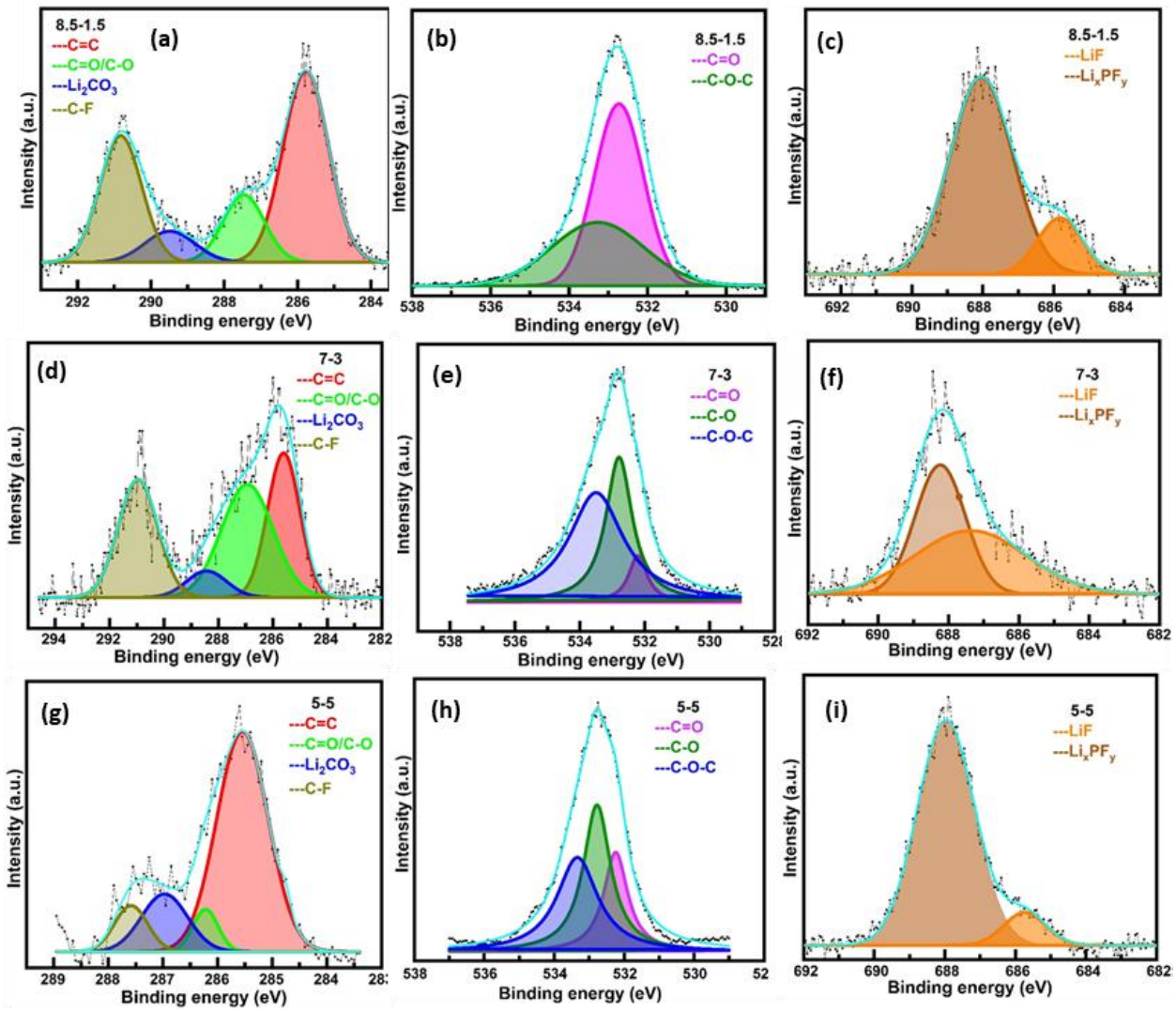

***Figure 28**: XPS of decrimped anode of PYPBIPA8.5-1.5 (a) C1s (b) O1s (c) F1s, of PYPBIPA7-3 (d) C1s (e) O1s (f) F1s, of PYPBIPA5-5 (g) C1s (h) O1s and (i) F1s*

results suggested that Li_2CO_3, LiF and Li_xPF_y were the major components of SEI in case of cycled PYPBIPA8.5-1.5 electrode. The C 1s spectra of cycled PYPBIPA7-3 anode displayed peaks at 285.6 eV, 284.6eV, 286.9eV, 284.4eV, 290.5eV corresponding to -C=C, -C=O/C-N, Li_2CO_3 and -C-F respectively (Fig. 28(d)). The O 1s spectra of cycled anode (Fig. 28(e)) had peaks at 532.2 eV, 532.7 eV and 533.4 eV corresponding to -C=O, -C-O, -C-O-C. The F 1s spectra of cycled anode (Fig. 28(f)) showed peaks at 687.3eV and 688.17eV corresponding to LiF and Li_xPF_y respectively. Further the deconvoluted C1s spectra of cycled PYPBIPA5-5 anode showed peaks at 285.5eV, 286.16 eV, 286.93 eV and 287.75 eV corresponding -C=C, -C=O/C-O, Li_2CO_3 and C-F respectively as given in Fig. 28(g).

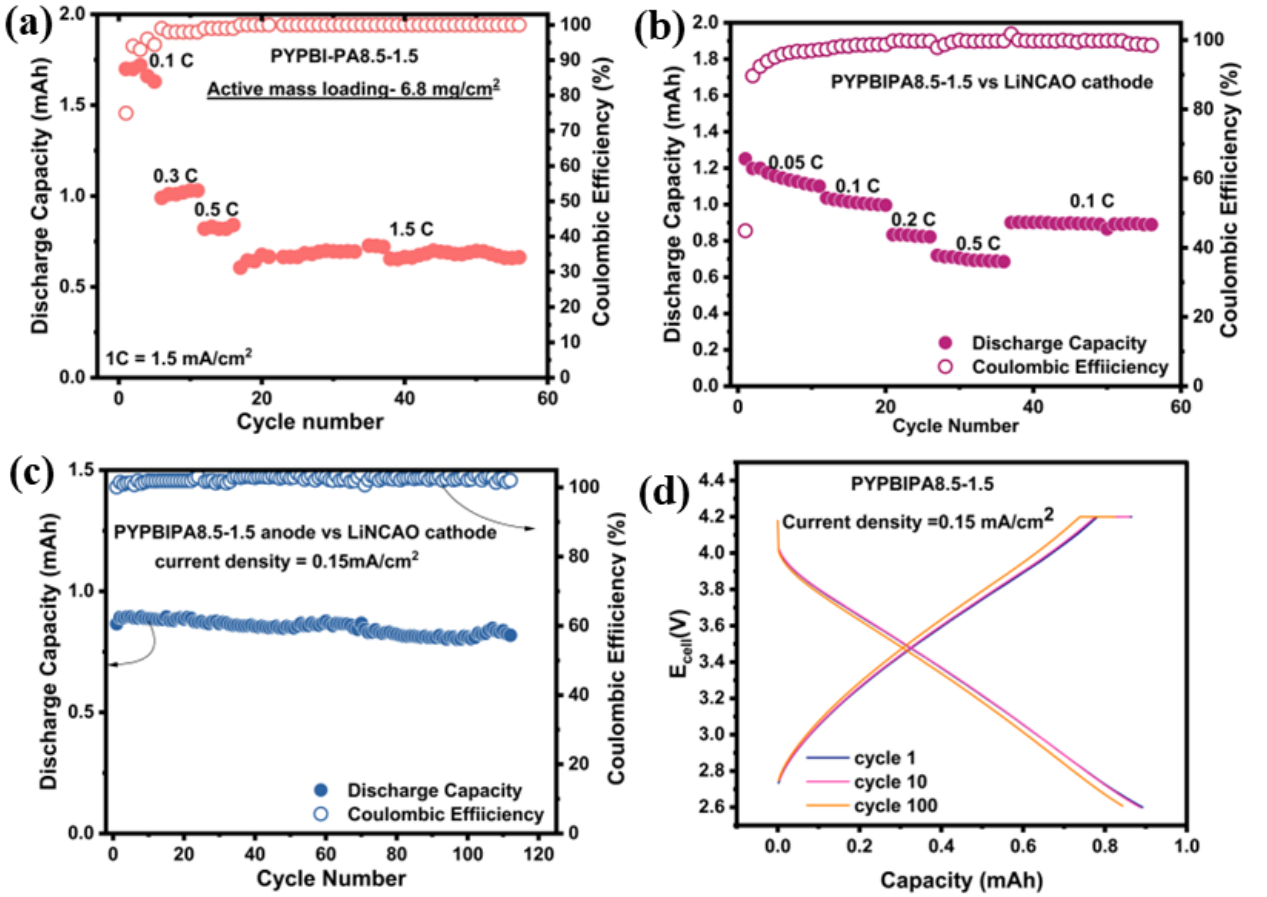

***Figure 29**: (a) Rate studies and long cycling of PYPBIPA8.5-1.5 based anodic half-cell at a high loading of 6.8mg/cm² (b) rate studies (c) long cycling (d) Charge discharge plots of PYPBIPA8.5-1.5 vs LiNCAO cathode full cell at 0.15mA/cm²*

The O 1s spectra of cycled anode (Fig. 28(h)) had peaks at 532.2 eV, 532.7 eV and 533.3 eV corresponding to -C=O, -C-O, C-O-C. The F 1s spectra of cycled anode (Fig. 28(i)) showed peaks at 685.7eV and 688.0eV corresponding to LiF and Li_xPF_y. Further, intrigued by the excellent performance of PYPBIPA8.5-1.5, anodic half cells were fabricated at a high mass loading ~6.8 mg/cm^2. The high loading anodic half-cell was cycled at various current densities of 0.1C, 0.3C, 0.5C, and 1.5C wherein 1.0C signifies 1.5 mA/cm^2. It showed a high initial capacity of 1.72 mAh followed by 1.0 mAh, 0.82 mAh and 0.7 mAh at 0.1C, 0.3C, 0.5C and 1.5C followed by 40 cycles at 1.5C (Fig. 29(a)). To gain a more comprehensive understanding of the full cell performance, coin cells were assembled utilizing anodes subjected to rate studies at high loading levels and cathodes from LiNCAO cycled for 5 cycles at 0.15 mA/cm^2. Charge-discharge studies of the full cell were performed in the voltage window of 2.6 to 4.2V in constant current constant voltage (CCCV) mode while maintaining constant voltage for 50 minutes. Initially rate studies were conducted for the full cell which indicated reversible capacities of 1.1, 1.0, 0.85, 0.72 mAh at 0.05, 0.1, 0.2, 0.5C (Fig. 29b). Further, when the cell was cycled back at 0.1C, a reversible capacity of 0.95mAh could be still obtained. Further long cycling studies of the full cell were performed as shown in Fig. 29(c). The long cycling studies were continued immediately after rate studies. During long cycling, an initial reversible capacity of 0.85 mAh was obtained which was retained up to 98% after 50 cycles and up to 95% after 100 cycles thus indicating the high stability of the material. Fig. 29(d) presents

the charge-discharge cycles of the full cell. These above results clearly indicated the commercial competence of PYPBI8.5-1.5.

2.5 Conclusions

In conclusion, this study presents a novel class of fast charging anodes for lithium-ion batteries, derived from bio-based polymers dually doped with nitrogen and oxygen. Three distinct copolymers PYPBIPA9-1, 8.5-1.5, 7-3, 6-4 and 5-5 were used to synthesize nitrogen and oxygen co-doped carbons wherein a progressive increase in oxygen content rising from 13.1 at% to 20 at% and further to 25 at% was observed, corresponding to an increase in the polyamide ratio in the copolymer from 1.5 to 3.0 to 5.0. PYPBIPA8.5-1.5 demonstrated impressive long cycling performance, delivering a delithiation capacity of 135 mAh/g over 3000 cycles with a capacity retention of 90%. Notably, it outperformed the purely nitrogen-doped carbon previously reported by our group [1]. This highlighted the clear advantage of incorporating oxygen alongside nitrogen to achieve optimal performance, especially in fast-charging applications. However, the observed variations in oxygen doping content had a significant impact on the final battery performance. The electrochemical investigations consistently identified PYPBIPA8.5-1.5, characterized by an optimal balance of nitrogen and oxygen doping, as the superior performer

amongst others. While the oxygen content was higher in PYPBIPA7-3 and 5-5, which have more surface redox sites for lithiation, they did not exhibit higher de-lithiation capacities compared to PYPBIPA8.5-1.5. This is due to the hindrance caused by the bulky oxygen groups, which impeded lithium-ion diffusion within the carbon planes. This phenomenon was confirmed through the evaluation of the lithium-ion diffusion coefficient which was found to be highest in the case of PYPBIPA8.5-1.5,

***Table 11**: Comparison of various bio derived carbons as anodes of lithium-ion batteries*

1	315 mAh g^{-1} at 100 mA g^{-1} current density with cycling stability over 100 cycles	*Waste Biomass-Derived Carbon Anode for Enhanced Lithium Storage*, ACS Omega, 2020, 5, 31, 19715–19720
2	272.1 $mAhg^{-1}$ at current density of 1000 mA g^{-1} beyond 500 cycles	*Pinecone-derived biomass carbons as anodes for lithium and sodium-ion batteries by template-assisted and chemically activated approaches,* Journal of Power Sources, Volume 580, 2023, 233329
3	444.8 mAh g^{-1} after 500 cycles at 1860 mAg^{-1}	*Natural biomass-derived porous carbons from buckwheat hulls used as anode for lithium-ion batteries,* Diamond and Related Materials, Volume 119, 2021, 108553
4	272 mAh g^{-1} at 74.4 mA/g after 200 cycles	*Biomass Porous Carbons Derived from Banana Peel Waste as Sustainable Anodes for Lithium-Ion Batteries,* Materials, 2021, 14(20), 5995
5	391 mAh g^{-1} at current density of 0.372 mA/g after 100 cycles	*Electrochemical Behavior of the Biomass Hard Carbon Derived from Waste Corncob as a Sodium-Ion Battery Anode,* Energy Fuels 2024, 38, 8, 7389–7398
6	170 mAh/g at 2000 mA/g in rate capability test	*Structural Analysis of Sucrose-Derived Hard Carbon and Correlation with the Electrochemical Properties for Lithium, Sodium, and Potassium Insertion,* Chem. Mater. 2020, 32, 7, 2961–2977

following the order PYPBIPA8.5-1.5 > 7-3 > 5-5. Further analysis of DEIS impedance data revealed that charge transfer resistance was highest in PYPBIPA8.5-1.5, intermediate in 7-3, and lowest in 5-5 which can be correlated to the oxygen doping contents in the final carbon materials. Given the polar nature of oxygen, PYPBIPA5-5, with maximum oxygen doping, facilitated easier charge transfer. Taking a holistic view, it was evident that while PYPBIPA8.5-1.5 exhibited a slightly higher charge transfer resistance owing to its lower oxygen content, this is effectively compensated for by faster lithium-ion diffusion rate. This was clearly reflected in its superior fast-charging capability. Hence, this study underscores the critical importance of balancing nitrogen and oxygen contents to achieve optimal electrochemical performance, especially during charge-discharge operations at higher current densities. Compared to previously reported bio-based hard carbons as shown in Table 11, this study also demonstrates the superior performance of hard carbon derived from bio-based poly(benzimidazole-co-amide) as an anode material for lithium-ion batteries (LIBs) than others.

References

1 X. Zeng, M. Li, D. Abd El-Hady, W. Alshitari, A. S. Al-Bogami, J. Lu and K. Amine, *Adv Energy Mater*, DOI:10.1002/AENM.201900161.

2 Q. Zhang, W. Cai, Y. X. Yao, G. L. Zhu, C. Yan, L. L. Jiang, C. He and J. Q. Huang, *Chem Soc Rev*, 2020, **49**, 3806–3833.

3 X. Wu, Y. Chen, Z. Xing, C. W. K. Lam, S. S. Pang, W. Zhang and Z. Ju, *Adv Energy Mater*, 2019, **9**, 1–46.

4 M. P. Bondarde, R. Jain, J. S. Sohn, K. D. Lokhande, M. A. Bhakare, P. S. Dhumal and S. Some, *Lithium-Sulfur Batteries: Materials, Challenges and Applications*, 2022, 521–545.

5 Y. Li, A. Vasileiadis, Q. Zhou, Y. Lu, Q. Meng, Y. Li, P. Ombrini, J. Zhao, Z. Chen, Y. Niu, X. Qi, F. Xie, R. van der Jagt, S. Ganapathy, M. M. Titirici, H. Li, L. Chen, M. Wagemaker and Y. S. Hu, *Nat Energy*, 2024, **9**, 134–142.

6 D. Chen, W. Zhang, K. Luo, Y. Song, Y. Zhong, Y. Liu, G. Wang, B. Zhong, Z. Wu and X. Guo, *Energy Environ Sci*, 2021, **14**, 2244–2262.

7 K. S. Patnaik, B. S. Mantripragada, S. Punyasloka and N. Matsumi, *Chemical Communications*, DOI:10.1039/D4CC04776A.

8 K. S. Patnaik, R. Badam, Y. Peng, K. Higashimine, T. Kaneko and N. Matsumi, *Chemical Communications*, 2021, **57**, 13704–13707.

9 C. P. Sandhya, B. John and C. Gouri, *Ionics (Kiel)*, 2014, **20**, 601–620.

10 C. Li, Z. Li, Y. He, H. Wang and Y. Xu, DOI:10.1021/acsaem.0c00946.

11 K. Kubota, S. Shimadzu, N. Yabuuchi, S. Tominaka, S. Shiraishi, M. Abreu-Sepulveda, A. Manivannan, K. Gotoh, M. Fukunishi, M. Dahbi and S. Komaba, *Cite This: Chem. Mater*, 2020, **32**, 2961–2977.

12 V. Simone, A. Boulineau, A. de Geyer, D. Rouchon, L. Simonin and S. Martinet, *Journal of Energy Chemistry*, 2016, **25**, 761–768.

13 A. Nag, M. A. Ali, H. Kawaguchi, S. Saito, Y. Kawasaki, S. Miyazaki, H. Kawamoto, D. T. N. Adi, K. Yoshihara, S. Masuo, Y. Katsuyama, A. Kondo, C.

Ogino, N. Takaya, T. Kaneko and Y. Ohnishi, *Adv Sustain Syst*, DOI:10.1002/adsu.202000193.

14 C. Zhou, A. Li, B. Cao, X. Chen, M. Jia and H. Song, *J Electrochem Soc*, 2018, **165**, A1447–A1454.

15 B. Srimitra Mantripragada, K. Sumala Patnaik, K. Higashimine, R. Badam and N. Matsumi, *Electrochem commun*, 2023, **157**, 107616.

16 K. S. Patnaik, B. S. Mantripragada, R. Badam, K. Higashimine, X. Zhong, T. Kaneko and N. Matsumi, *Nanoscale Adv*, 2024, **6**, 5181–5192.

17 H. Zhao, J. Ye, W. Song, D. Zhao, M. Kang, H. Shen and Z. Li, *ACS Applied Materials & Interfaces*, 2020, **12**, 6991–7000.

18 A. C. Lazanas and M. I. Prodromidis, *ACS Measurement Science Au*, DOI:10.1021/acsmeasuresciau.2c00070.

19 T. P. Jayakumar, R. Badam and N. Matsumi, *ACS Appl Energy Mater*, 2020, **3**, 3337–3346.

20 A. Patra and N. Matsumi, *ACS Appl Energy Mater*, DOI:10.1021/acsaem.3c02137.

21 F. Xie, Y. Niu, Q. Zhang, Z. Guo, Z. Hu, Q. Zhou, Z. Xu, Y. Li, R. Yan, Y. Lu, M. M. Titirici and Y. S. Hu, *Angewandte Chemie - International Edition*, DOI:10.1002/anie.202116394.

22 J. C. Burns, L. J. Krause, D.-B. Le, L. D. Jensen, A. J. Smith, D. Xiong and J. R. Dahn, *J Electrochem Soc*, 2011, **158**, A1417.

23 A. Varma, R. Badam, A. L. James, K. Higashimine, K. Jasuja and N. Matsumi, *ACS Appl Nano Mater*, 2022, **5**, 16154–16163.

24 T. Ramesh, R. Vedarajan, N. Rajalakshmi and L. R. G. Reddy, *Journal of Materials Science: Materials in Electronics*, 2020, **31**, 1681–1690.

25 S. Suriyakumar, A. Varma, V. Surendran, K. Jasuja and M. M. Shaijumon, *Batter Supercaps*, 2022, **5**, e202100243.

26 W. Choi, H. C. Shin, J. M. Kim, J. Y. Choi and W. S. Yoon, *Korean Electrochemical Society*, 2020, preprint, DOI: 10.33961/jecst.2019.00528.

27 A. Gupta, R. Badam and N. Matsumi, *ACS Appl Energy Mater*, 2022, **5**, 7977–7987.

28 B. Srimitra Mantripragada, R. Badam and N. Matsumi, *ACS Appl Energy Mater*, 2022, **5**, 6903–6912.

29 A. Gupta, R. Badam, A. Nag, T. Kaneko and N. Matsumi, *ACS Appl Energy Mater*, 2021, **4**, 2231–2240.

3. Bio-based poly(benzothiazole) derived N, S co-doped carbons as fast-charging anodes for sodium-ion batteries

3.1 Abstract

Sodium-ion batteries (SIBs) have emerged as a promising next-generation energy storage technology following the widespread success of lithium-ion batteries (LIBs). However, achieving fast-charging capability in SIBs remains a significant challenge, primarily due to the inherently sluggish diffusion kinetics of sodium ions. This limitation is often manifested as an extended low-potential plateau in the charge-discharge profiles. To address this issue, various strategies have been explored, among which heteroatom doping has gained considerable attention. Nitrogen doping has been extensively studied for its ability to enhance electronic conductivity and promote surface adsorption through pseudocapacitive behavior. Sulfur doping, particularly relevant to SIB anodes, offers additional advantages due to its larger atomic radius, which facilitates increased interlayer spacing and enables additional sodium-ion storage via non-faradaic reactions. In this study, we investigate a nitrogen and sulfur co-doped hard carbon material derived from the bio-based polybenzothiazole as an anode for SIBs. The hard carbon materials were synthesized at two different pyrolysis temperatures to systematically evaluate the impact of morphological and elemental characteristics on their fast-charging performance.

3.2 Introduction

Lithium-ion batteries (LIBs) have experienced rapid development and are now widely integrated into nearly all modern technological devices following their successful commercialization. However, the uneven global distribution of lithium and the high cost of cobalt have highlighted the need for alternative energy storage solutions[1]. In this context, sodium-ion batteries (SIBs) have emerged as promising next-generation technology, largely due to their lower material costs and the abundant availability of sodium. The cost-effectiveness of SIBs is further enhanced by the use of readily available and inexpensive materials such as iron and manganese in their cathodes, making them a viable option for large-scale and affordable energy storage[2]. However, the direct translation of technology from lithium-ion batteries (LIBs) to sodium-ion batteries (SIBs) presents significant technical challenges, primarily due to the larger ionic radius of Na^+ compared to Li^+ and the incompatibility of commonly used LIB materials—such as graphite anodes—which are not suitable for efficient sodium-ion intercalation[3]. Hard carbons- an alternative carbonaceous material has gained significant interest as an anode of SIBs. However, hard carbons (HCs) still face challenges related to poor rate capability and limited cyclability. Especially since Na^+-ions are 55% larger than Li^+-ions, and the diffusion kinetics of Na^+-ions is much more sluggish[4]. Their charge–discharge curves typically feature a sloping region at higher potentials and a plateau region at lower potentials. Most of the capacity improvement in HCs is attributed to the low-potential plateau region. However, this region is diffusion-controlled and exhibits slower kinetics, which limits the rate performance. Additionally, the extended low-potential plateau, being close to the sodium plating potential, poses safety concerns, particularly at high current rates. In contrast, the sloping region

offers faster kinetics and better rate capability, reducing the risk of sodium plating during cycling. Therefore, engineering HCs with a slope-dominated charge–discharge profile could enable the development of high-power and safer SIBs, making them well-suited for EVs and other fast-charging applications[5]. Heteroatom doping has emerged as one of the most promising strategies to enhance pseudocapacitive Na^+ ion adsorption, thereby effectively improving the capacity contribution from the sloping region. Among the various strategies explored to enhance Na^+ ion storage, heteroatom doping has emerged as a highly effective approach, as it enhances pseudocapacitive Na^+ adsorption and boosts capacity contributions from the sloping region of the voltage profile. While numerous materials have been studied for synthesizing hard carbon in SIBs, the use of bio-based polymers as a single source of both carbon and heteroatoms remains relatively rare. Hence, the objective of this research work was to utilize a bio-based polymer for obtaining a heteroatom doped HC which can enable high power applications in SIBs. Amongst the various types of heteroatoms, N-doping is one of the most highly investigated owing to the least difference in electronegativity between carbon (2.55) and nitrogen atoms (3.04)[6]. Sulfur doping can significantly expand the interlayer distance due to its larger atomic size, which is crucial for facilitating the movement of bulky Na^+ ions[7]. Additionally, sulfur can enhance sodium storage by participating in faradaic reactions with Na^+ ions. It also helps in tuning the electronic structure, leading to better conductivity and rate performance. Hence, based on these insights, we developed an N, S co-doped hard carbon material derived from a single polymer precursor, polybenzothiazole. In addition, the uniqueness of this polymer lies in its bio-derived origin, as it can be synthesized from precursors obtained from renewable, bio-based sources. Hence the objective

of this study was to utilize a bio-based polymer for synthesis of N,S cod-oped hard carbon for utilization in SIBs as well as to investigate the impact of carbonization temperature on the morphological and thereby the electrochemical properties of the resulting anodes.

3.3 Experimental Section

Materials

4-amino-3-mercaptobenzoic acid was obtained from ACHEMBLOCK. Sodium perchlorate ($NaClO_4$) was purchased from Sigma Aldrich. Ethylene carbonate and propylene carbonate were purchased from Tokyo Chemical Industry (TCI, Japan). Hard carbon was obtained from Kurranode type2 (5µm). Battery grade acetylene black was purchased from Denka Japan Private Co. Ltd. for usage as conductive material in the anode, poly(vinylidene fluoride) was purchased from Sigma Aldrich. N-Methyl 2-pyrrolidone (NMP), was purchased from FUJIFILM Wako Pure Chemical Corporation (Wako, Japan).

Synthesis:

The detailed synthetic procedure of the polymer was reported by Kaneko et.al[8]. Briefly, the polymers were synthesized using 4-amino-3-mercaptobenzoic acid as precursor (Scheme 2). Initially the solvent (PPA) was heated at 100°C for removing any moisture followed by addition of precursors and polymerization at 180°C for 4h

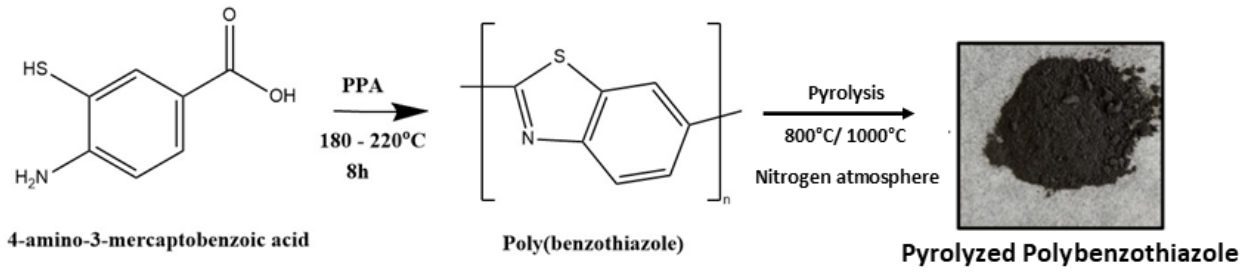

***Synthesis Scheme 2**: Synthetic procedure for poly(benzothiazole)*

followed by 200°C for 10h in nitrogen atmosphere. The obtained polymer was then cooled to room temperature and stirred in a beaker containing distilled water to wash off the unreacted precursors. The polymer was then crushed and dispersed in 10% KOH aq. solution and the mixture was continuously stirred at room temperature overnight before filtering and washing with water until neutral pH. The resulting polymer powders were then dried under vacuum at 80°C for 8h. The polymer was then pyrolyzed at 800°C and 1000°C for obtaining carbon materials which were named as PYPBT800 and PYPBT1000 respectively. The pyrolysis was conducted in two different steps. Initially the temperature was raised to 750°C at 5°C/min and later increased to 800°C at 1°C/min. Further, the temperature was maintained at 800°C for 1 hour. Similarly, the pyrolysis was conducted by raising the temperature to 950°C at 5°C/min and later increased to 1000°C at 1°C/min. The pyrolyzed materials were ultrasonicated in 10% HCl solution to remove any amorphous carbon or carbonate impurities in the samples. The ultrasonication was followed by filtration and drying at 80°C under vacuum for about 12 hours.

Instruments Used

X-ray photoelectron spectroscopy (XPS) measurements were conducted on a AXIS-ULTRA-DLD, Shimadzu Cratos Inc. instrument. Powder X-ray diffraction (XRD) studies were conducted on Smart Lab X-Ray Diffractometer, Rigaku with Cu Kα radiation (λ = 0.154 nm, over the 2θ range of 2°- 45° with a step size of 0.02°).

Electrode preparation and cell fabrication

The respective carbon materials, PVDF, and acetylene black were mixed in 8:1:1 ratio and rotated in Kakuhunter ball mill for preparing a uniform slurry. The obtained slurry was coated on copper foils using a doctor blade while maintaining

a thickness of 0.1 mm. The electrodes were then kept in vacuum oven at 80°C for about 12 hours. The dried electrodes were calendared to 0.06 mm thickness at 80°C. Electrodes of 17 mm diameter were punched out of the calendared sheets. CR2025 type coin cells were fabricated inside an argon filled glove box (O_2, H_2O, < 0.5 ppm) using PYPBT anodes, sodium foil as counter and reference electrode, glass fiber separator (Whatman) and 1.0M $NaClO_4$ (50:50) ethylene carbonate: propylene carbonate (EC: PC) as electrolyte.

3.4 Characterization and Electrochemical Studies

The XRD plots of PYPBT800 and 1000 are shown in Fig. 30 (a). The plots indicate a broad peak at 24.73 and 25.14° corresponding to 002 reflection. The d-spacing calculated using Bragg's law was found to be 3.60 and 3.54 Å respectively. This observation indicates that with increasing pyrolysis temperature, the interlayer d-spacing decreases, suggesting enhanced structural ordering as carbon planes progressively align and pack more closely which can be attributed to the thermal

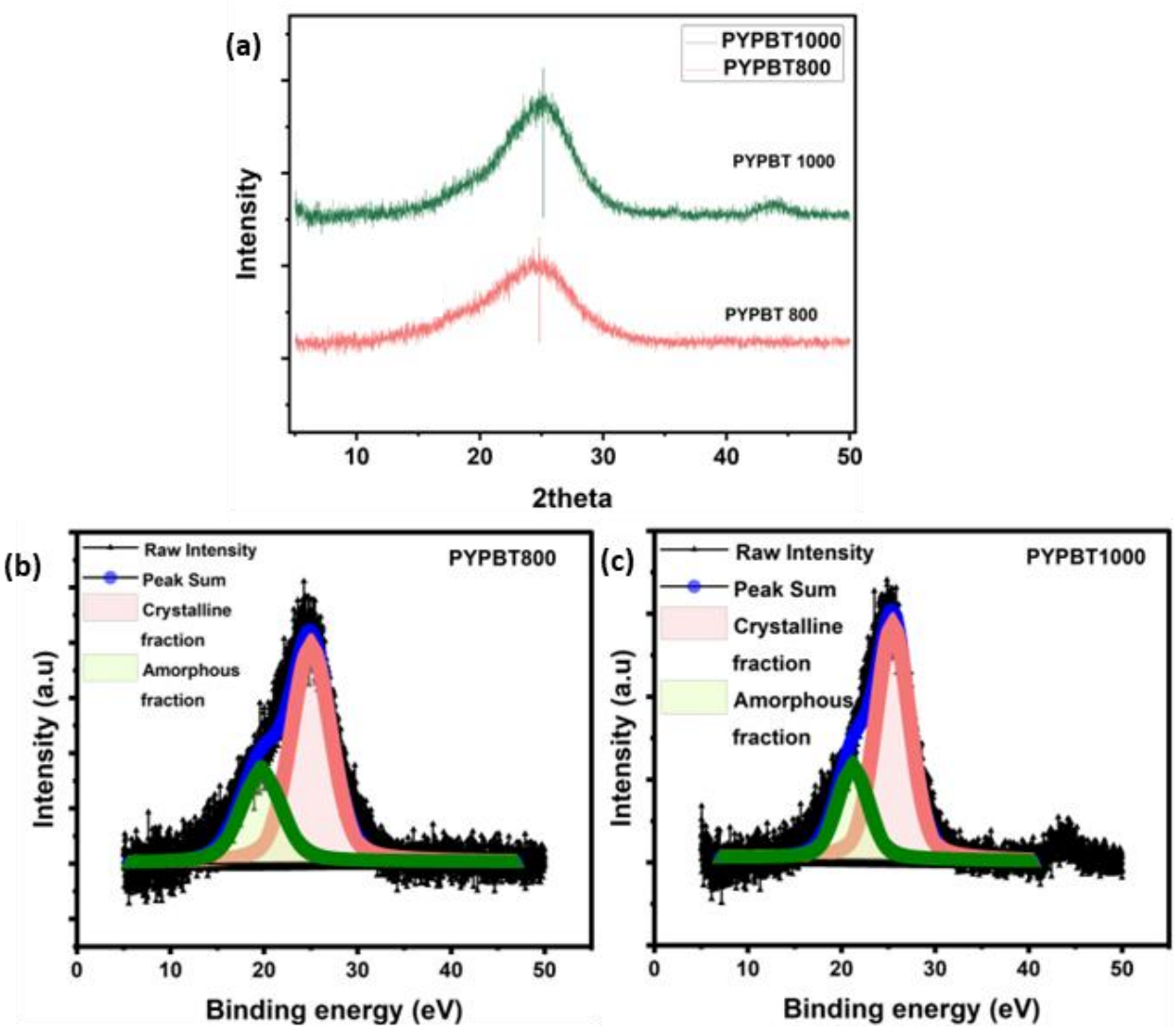

***Figure 30**: (a) Comparison of XRD plots of PYPBT800 and PYPBT1000, percentage distribution crystalline and amorphous fraction in (b)PYPBT800 (c)PYPBT1000*

decomposition of the surface functional groups and heteroatoms that reduce the interplanar distance and facilitate formation of graphitic domains by atomic rearrangement. Furthermore, the XRD plots were deconvoluted which indicated two peaks in each case corresponding to amorphous fraction and crystalline fraction. In case of PYPBT800, the amorphous fraction was found to be 31.70% whereas the crystalline fraction was found to be 68.30% as shown in Fig. 30(a). Furthermore, in the case of PYPBT1000 as shown in Fig. 30(b), the amorphous fraction was determined to be 28.27%, while the crystalline fraction was 71.72% as shown in Table 1. These results suggest that with increasing pyrolysis temperature, the amorphous content decreases while the crystalline content in the carbon material increases. To further investigate the structural ordering, the R-factor—an indicator of the relative number of carbon sheets stacked parallel within a given crystal—was calculated. The R-factor was obtained by dividing the background to the signal ratio and was found to be 2.97 and 3.62 for PYPBT800, and PYPBT1000, respectively as shown in Fig. 31(a) and (b). This trend (PYPBT800 < PYPBT1000) indicates a progressive increase in the stacking of carbon sheets with increasing pyrolysis temperature. Thus, these findings further confirm that higher pyrolysis temperatures promote greater stacking of carbon planes, thereby enhancing the

graphitic domains in the carbon structure. In order to gain deeper understanding of the morphological structure of these carbons, Raman spectroscopy was conducted

***Table 1**: Percentage distribution of crystalline and amorphous fraction*

	PYPBT800	PYPBT1000
% crystalline	68.30 %	71.72 %
% amorphous	31.70 %	28.27 %

which indicated two conventional peaks at similar Raman shifts of ~1350 cm^{-1} and ~1570 cm^{-1}, that can be identified as the D-band (defect-induced mode) and G-band (E_{2g} mode), respectively. The I_d/I_g ratio which is the ratio of D band to G band was found by dividing the intensity of D peak to G peak. The I_d/I_g ratios were found to be 1.05 and 0.87 for PYPBT800 and PYPBT1000 respectively. This clearly indicates that the defect density within the carbon planes decreases with increasing pyrolysis temperature, likely due to thermally induced structural rearrangement that minimizes vacancies, edge sites, and heteroatom-induced disruptions, thereby promoting enhanced graphitization[9]. To further analyse the elemental composition, XPS was performed, and the survey spectra are shown in Fig. 31 (e) and (f). The spectra displayed characteristic peaks[10] at 165.0 ± 0.5, 230.0 ± 0.5, 284.6 ± 0.5, 400.0 ± 0.5, 532.0 ± 0.5, corresponding to S2s, S2p, C1s, N1s and O1s in the samples[10]. The at% for each element in PYPBT800 and PYPBT1000 was calculated by integrating the area under the curves for respective XPS spectrum followed by normalizing with respective sensitivity factors as shown in equation (1).

$$\text{At.}\,\% = \frac{\frac{A_i}{SF_i}}{\Sigma_i \frac{A_i}{SF_i}} \times 100 \quad \ldots\ldots\ldots\ldots\ldots\ldots(1)$$

where i= Carbon/Nitrogen/Oxygen/Sulphur.

The atomic percentages of C1s, N1s, O1s, and S2p for PYPBT800 were observed to be 80.02%, 3.02%, 15.45%, and 1.48%, while it was found to be 83.46%, 1.12%, 14.72%, and 0.70% in PYPBT1000, respectively. These results clearly indicate that with increasing pyrolysis temperature, the contents of nitrogen and sulfur decrease. The deconvolution of XPS spectra for the PYPBT samples revealed detailed

information about the bonding environments present in each. For PYPBT800, the C1s spectrum exhibited five distinct peaks[10] at 284.0, 284.5, 285.1, 286.1, and 288.6

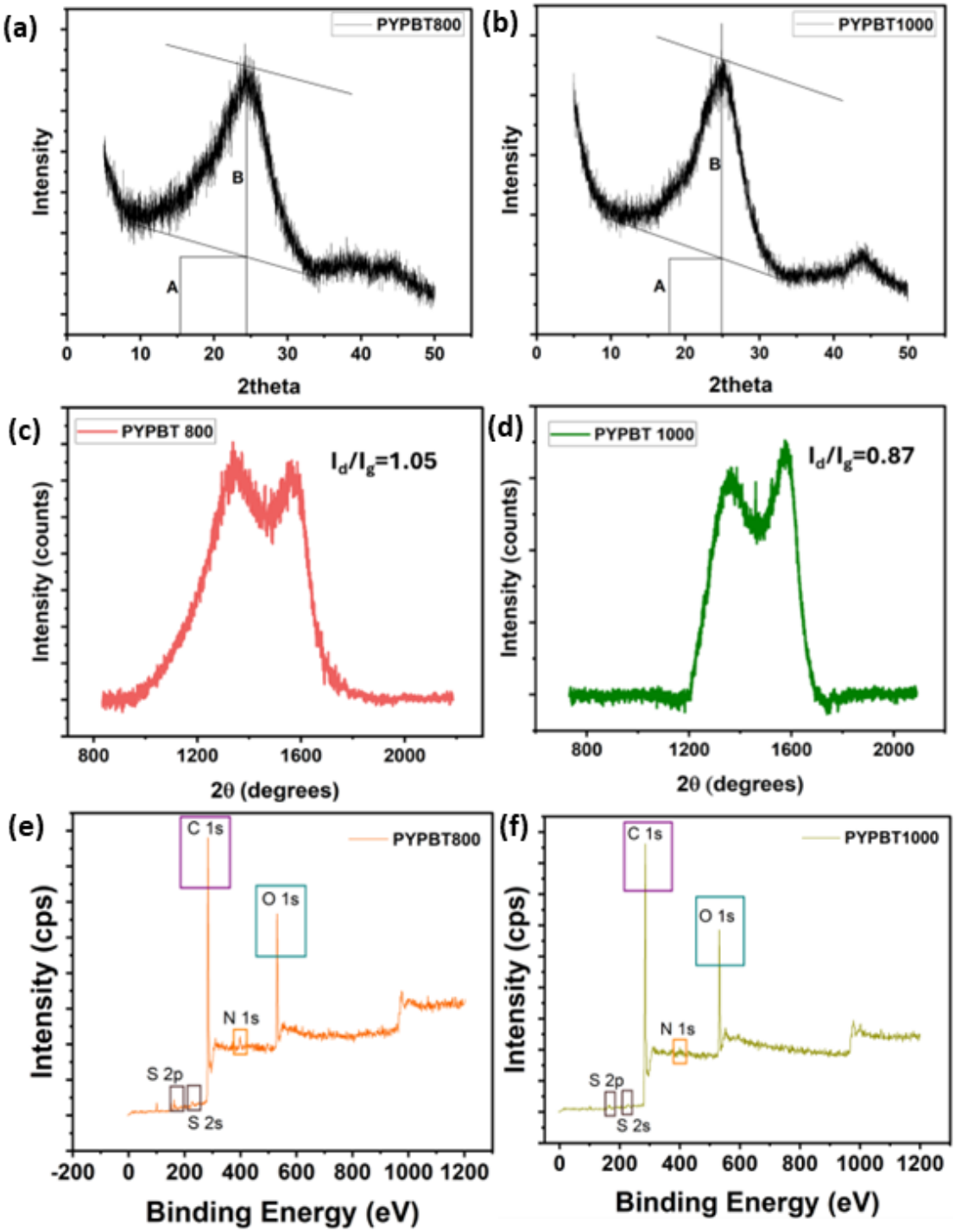

***Figure 31**: Calculation of R-factor of (a)PYPBT800 (b) PYPBT1000, Raman spectrum of (c)PYPBT800 (d)PYPBT1000 and XPS survey spectrum of (e) PYPBT800 (f) PYPBT1000*

eV corresponding to C–C/C–H, C=C, C–N, C–O, and C–S bonds, respectively as displayed in Fig. 32(a). The N1s spectrum showed three peaks[10] at 398.0, 400.0, and 402.6 eV, attributed to pyridinic nitrogen, graphitic nitrogen, and N-oxide as shown in Fig. 32(b). The O1s peaks[10] at 530.5, 531.9, and 533.2 eV corresponded to O–C, O–N, and O–S while the S2p spectrum showed peaks[10] at 163.6, 164.9, 167.8, and 169.3 eV, assigned to S-C2p$^{1/2}$, S-C2p$^{3/2}$, S-O2p$^{1/2}$ and S-O2p$^{3/2}$ indicated in Fig. 32(c) and Fig. 32(d) respectively. For PYPBT1000, the C1s region exhibited five peaks at 284.26, 284.96, 285.6, 286.6, and 289.1 eV, corresponding to C–C/C–H, C=C, C–N,

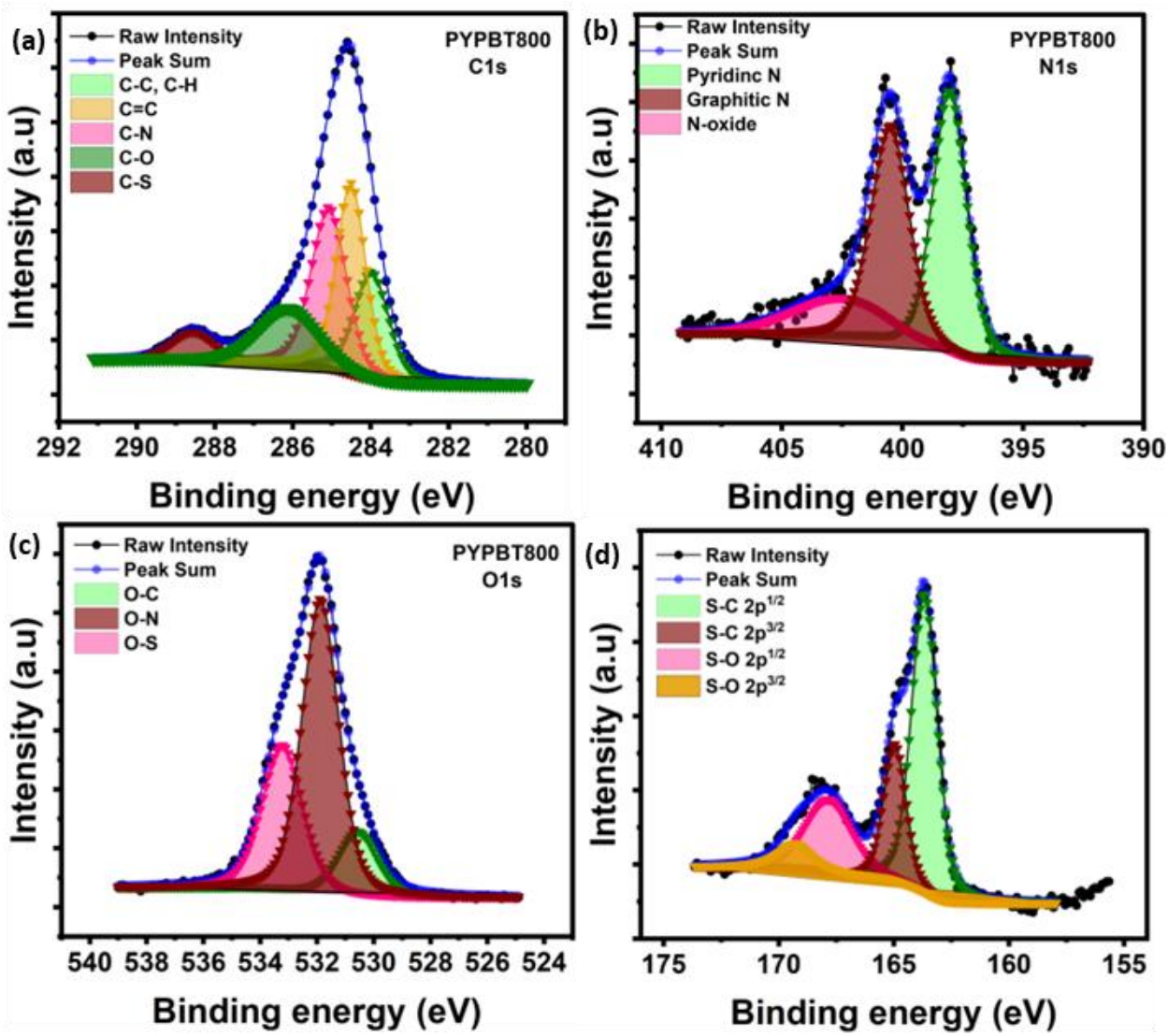

***Figure 32**: Deconvoluted XPS spectra of (a) C1s (b) N1s (c) O1s and (d) S2p in PYPBT800*

C–O, C-S respectively as displayed in Fig. 33(a). N1s showed three peaks at 398.2, 400.8, and 402.5 eV for pyridinic nitrogen, graphitic nitrogen, and N-oxide[10], respectively as displayed in Fig. 33(b). The O1s peaks[10] displayed in Fig. 33(c) at 530.6, 532.4, and 533.9 eV corresponded to O–C, O–N, and O–S whereas the S2p peaks as shown in Fig. 33(d) at 163.9, 165.1, 168.4, and 169.2 eV indicated the presence of S-C2p$^{1/2}$, S-C2p$^{3/2}$, S-O2p$^{1/2}$ and S-O2p$^{3/2}$. These results provide clear evidence of the bonding structures and heteroatom functionalities evolving with pyrolysis temperature. The corresponding area contribution in percentage was

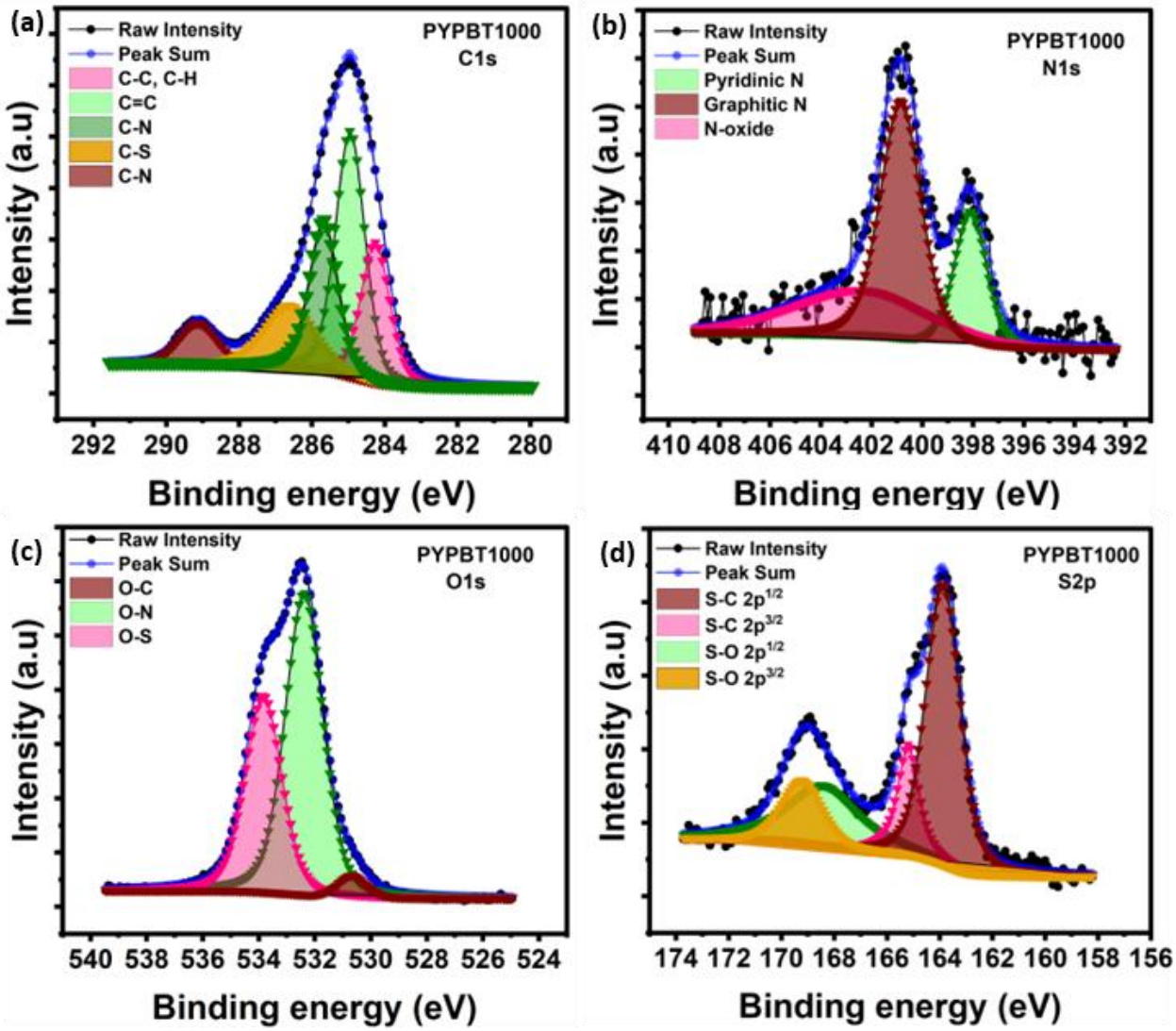

***Figure 33**: Deconvoluted XPS spectra of (a) C1s (b) N1s (c) O1s and (d) S2p in PYPBT1000*

calculated for each functionality. In case of PYPBT800, the area corresponding to pyridinic nitrogen was found to be 42.40% for pyridinic nitrogen whereas it was found to be 39.62% for graphitic nitrogen and 17.97% for N-oxide. In PYPBT1000, the percentage area corresponding to pyridinic nitrogen was found to be 21.60% compared to 47.78% for graphitic nitrogen and 30.60% for N-oxide. From the above data it can be observed that the content of pyridinic nitrogen decreases with pyrolysis temperature whereas the content of graphitic nitrogen increases. This could be because pyridinic nitrogen is generally located at the edges or the defective sites of the graphene layers bonded to two carbon atoms. With increasing pyrolysis temperature, as observed from I_d/I_g values as well, the edge sites and defect sites become less stable because of which pyridinic nitrogen becomes less favorable due to its lower thermal stability as the structure becomes more crystalline and ordered with higher graphitic nitrogen content[11]. Nitrogen doping can markedly enhance the electronic conductivity of carbon layers and facilitate the adsorption of sodium ions through surface interactions[12]. Meanwhile, the incorporation of sulfur helps expand the interlayer spacing within the carbon structure, thereby promoting greater ion mobility and improved diffusion of sodium ions[10]. Additionally, sulfur contributes to sodium storage through non-faradaic reactions, further boosting the material's electrochemical performance. Following this, electrochemical studies were conducted using CR2025 type coin cells fabricated under Ar atmosphere (O_2 andH_2O < 0.5ppm). Initially, the batteries were subjected to cyclic voltammetry at a scan rate of 0.1mV/s as shown in Fig. 34. The cyclic voltammogram of PYPBT800 shown in Fig. 34(a) indicated a broad peak which is typical of HCs due to the disordered arrangement of carbon layers that allows sodiation and de-sodiation in wide range of potentials[13]. However, in case of

PYPBT1000, the sodiation peak was observed to be sharper as shown in Fig. 34(b) than PYPBT800 which could be due to more ordered arrangement of carbon layers than PYPBT800 as observed from morphological studies. A peak at 0.65V was observed in the reduction half corresponding to reduction of solvent that can be called as solid electrolyte interphase (SEI). Following this, electrochemical impedance spectroscopy (EIS) was conducted in order to compare the resistance before and after CV. After CV, the resistance was observed to decrease drastically from 139 ohms to 20 ohms, and 277 ohms to 30 ohms in the case of PYPBT800 and PYPBT1000, respectively (Fig. 34(c, d). The decrease in resistance observed in both the samples after CV can be ascribed to the development of SEI at the

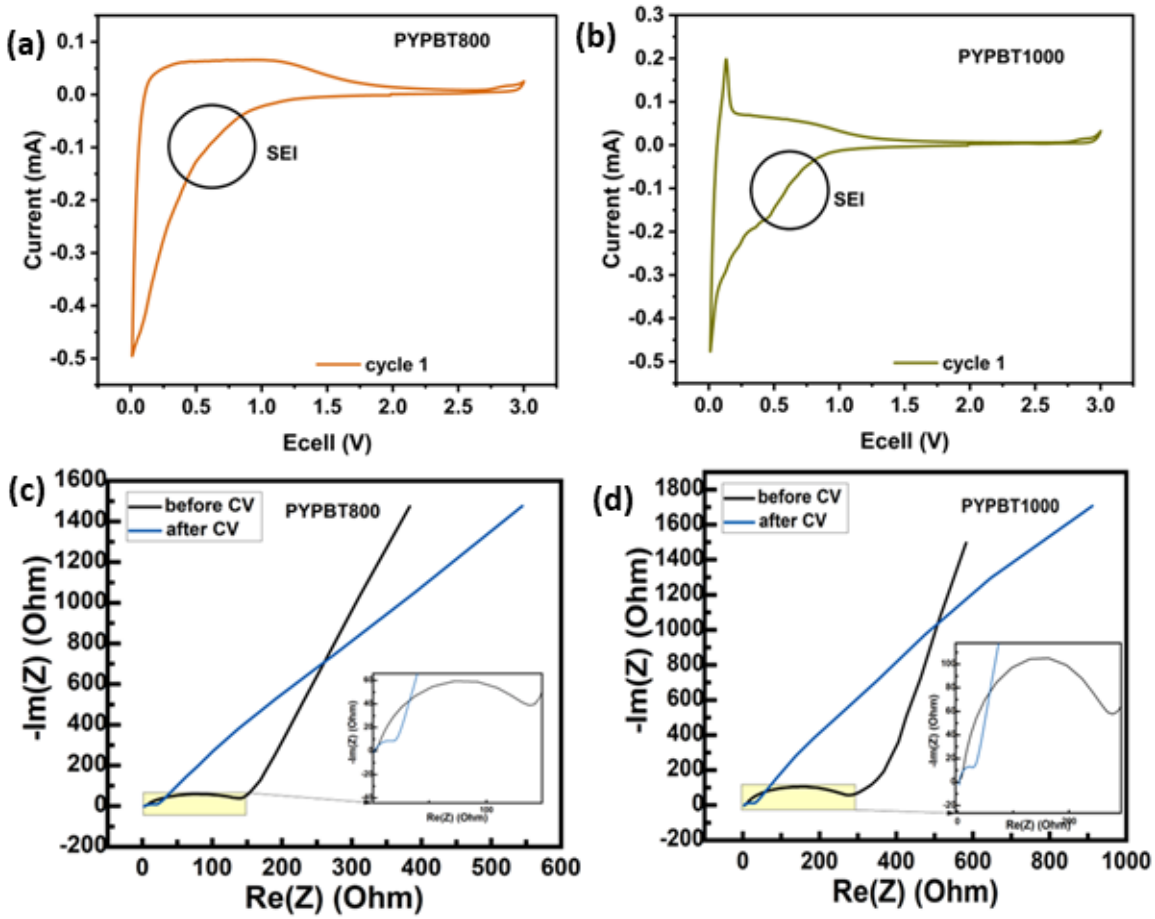

***Figure 34**: Cyclic voltammograms of (a) PYPBT800 (b) PYPBT1000 and EIS plot of (c) PYPBT800 and (d) PYPBT1000*

electrode/electrolyte interface during cycling[14]. An SEI prevents further decomposition by creating a protective barrier between the electrode and the electrolyte. The SEI formation consumes Na-ions however, once formed, the SEI allows Na^+ ions to pass through, but blocks electrons[15]. This prevents further electrolyte breakdown, which is key for long-term electrochemical stability. Following this, galvanostatic charge–discharge studies were conducted at varying current densities to evaluate the rate capability of the samples. For all measurements, the same current densities were applied during both sodiation and sodiation processes to ensure consistency. When tested at current densities of 50, 100, 200, 500, 1000, and 2000 mA/g, PYPBT800 demonstrated higher capacities of 200, 175, 165, 135, 120, and 100 mAh/g with coulombic efficiencies of 90.8, 95.9, 98.0, 99.3, 99.8 and 99.9% under the same conditions whereas PYPBT1000 showed capacities of 175, 145, 75, 95, 85, and 55 mAh/g with coulombic efficiencies of 86.6, 93.6, 95.1. 98.7, 99.8 and 99.8% respectively. When the current density was reverted to 50 mA/g after high-rate cycling, the capacities recovered to 175 mAh/g and 150 mAh/g with coulombic efficiencies of 96.3% and 92.5% for PYPBT800 and PYPBT1000 respectively (Fig. 35(a)). This recovery highlights the excellent structural stability and reversibility of the materials, even after being subjected to high-rate cycling. The rate studies clearly indicated that PYPBT800 shows better performance than PYPBT1000 at all current densities. When long cycling was conducted at low current density of 200 mA/g, PYPBT800 outperformed PYPBT1000 exhibiting a de-sodiation capacity of 158 mAh/g compared to 123 mAh/g with nearly 98.8% retention compared to and ~96.1% retention respectively. Furthermore, long cycling was conducted at 2000 mA/g to understand the long cycling capability at high current density wherein the de-sodiation capacity was observed to be 79 mAh/g

and 54 mAh/g after 50 cycles and, 71 mAh/g and 51 mAh/g after 1000 cycles for PYPBT800 and PYPBT1000 respectively. Hence, the capacity retention was observed to be 83% and 91% after 500 cycles respectively (Fig. 35(c)). Therefore, long-term cycling and rate capability studies confirm that PYPBT800 outperforms PYPBT1000, especially in terms of ion storage capability. Even for applications requiring lower current densities and enhanced stability, PYPBT800 with larger number of defect sites, higher nitrogen and sulphur content and enlarged interlayer spacing remains the more favourable choice. However, for applications prioritizing long-term cycling stability along with fast-charging capability, PYPBT1000 with its more ordered carbon layer structure may be the more suitable choice with compromise on

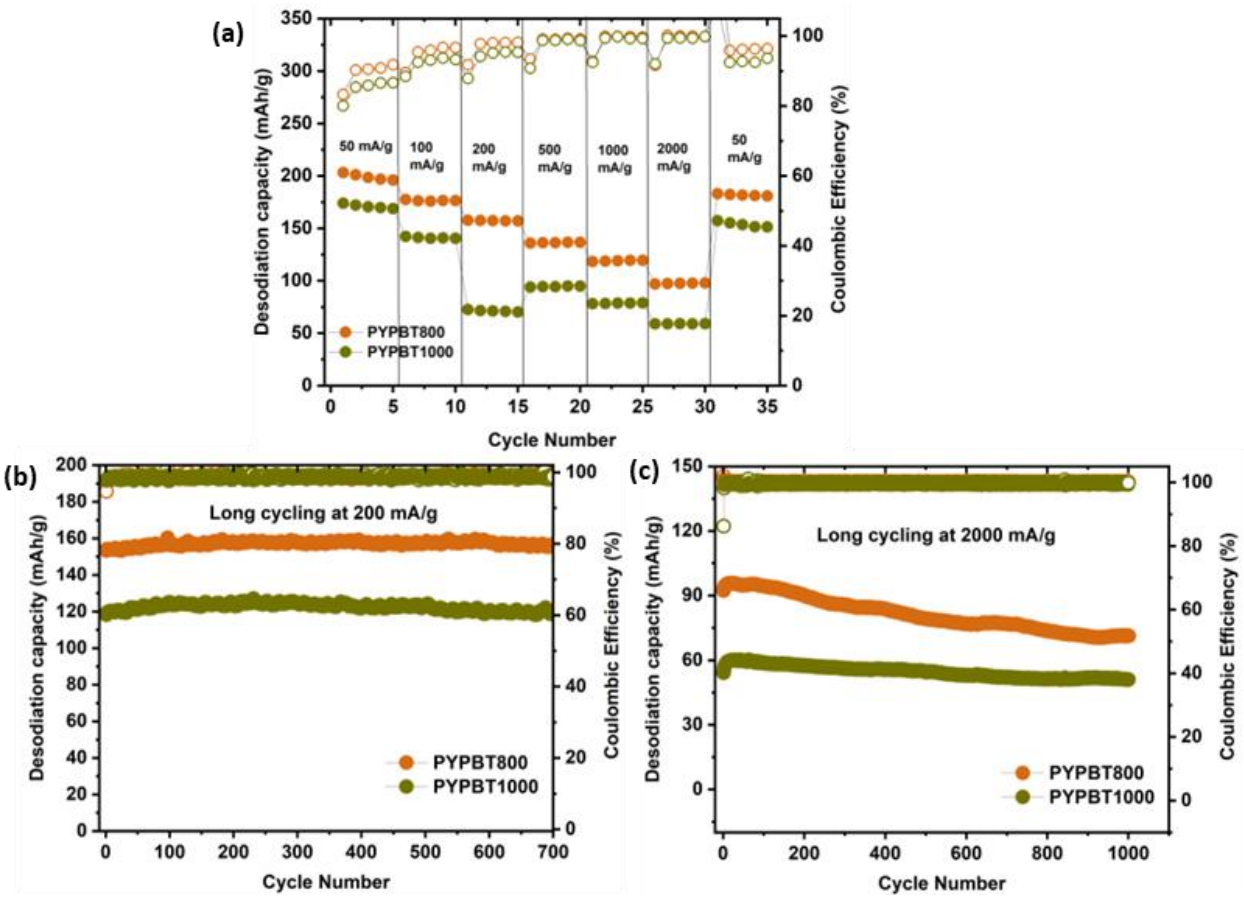

***Figure 35**: Comparison of (a) rate studies (b) long cycling at 200 mA/g and (c) long cycling at 2000 mA/g for PYPBT800 and PYPBT1000*

capacity. In particular, PYPBT800 showed a remarkable discharge capacity of 79 mAh/g with a capacity retention of 83% even after 500 cycles even at a high current density of 2000 mA/g. Overall, bio-based polymers allow for molecular-level design towards eco-friendly route to functional carbon materials. To understand the Na-ion kinetics governing the fast-charging behaviour in PYPBT800, cyclic voltammetry scan rate studies were conducted at 0.1, 0.3, 0.5, 0.7, and 1.0 mV/s to understand the Na-ion kinetics as shown in Fig. 36[16]. Power law,

$$i = av^b \text{..... equation (1)}$$

was utilized wherein i signifies current, v signifies scan rate. Typically, the value of a is interpreted from the intercept and the value of b is interpreted from the slope of the plot log i vs. log v. The value of b indicates the dominant charge storage mechanism, distinguishing between diffusion-controlled and capacitive-controlled processes. The linear fit of the logarithmic plot of log i vs log v for PYPBT800 and PYPBT1000 is shown in Fig. 36 (c) and (d) respectively. The value of b calculated using this method indicated it to be 1.00 and 0.52 respectively. Further, the contribution of diffusion and capacitive based currents was calculated using the equation 2[17]

$$i = k_1 v + k_2 v^{1/2} \text{..... equation 2}$$

wherein the redox current i is a cumulative measure of the capacitive based charge storage k_1v and diffusion-based charge storage $k_2v^{1/2}$ at each scan rate. k_1 and k_2 values were determined using a linear fit of $i/v^{1/2}$ vs $v^{1/2}$. The calculations indicated that the percentage contribution of capacitive based current at 0.1, 0.3, 0.5, 0.7,

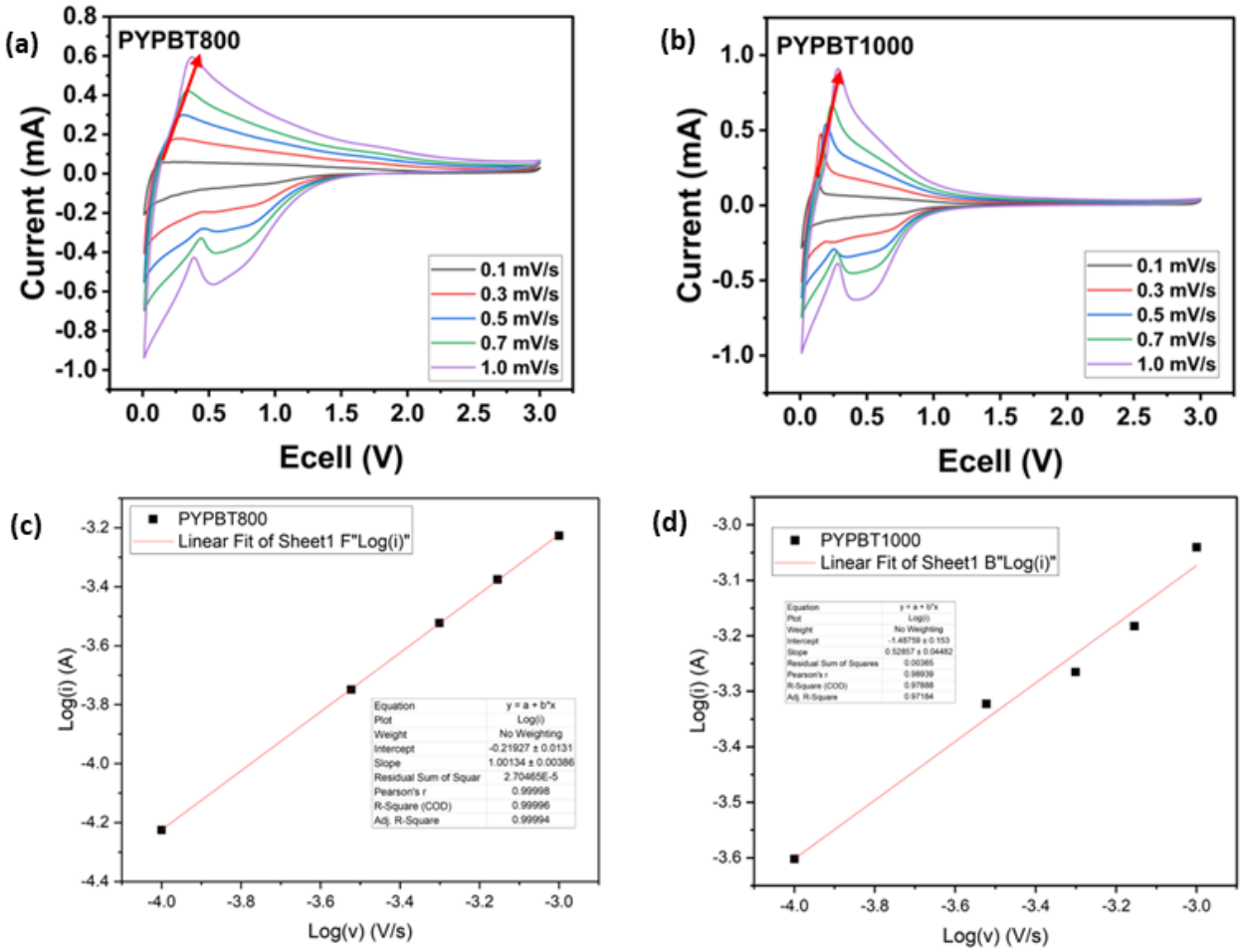

***Figure 36**: CV at different scan rates for (a)PYPBT800 (b) PYPBT1000 (c) log(i) vs log(v) for PYPBT800 and (d) log(i) vs log(v) for PYPBT1000*

and 1.0 mV/s was 95.70, 97.47, 98.02, 98.33 and 98.60% for PYPBT800 whereas it was found to be 28.29, 40.60, 46.87, 51.07, 55.50 % for PYPBT1000. Similarly, the percentage contribution of diffusion-based currents was found to be 4.30, 2.53, 1.97, 1.67, 1.40% for PYPBT800 whereas it was found to be 71.71, 59.40, 53.13. 48.90. 44.50 % at 0.1, 0.3, 0.5, 0.7, and 1.0 mV/s respectively for PYPBT1000. These results have been displayed in Fig. 37(a) and (b). The results clearly indicate that with increasing pyrolysis temperature accompanied by reduced heteroatom doping and enhanced crystallinity, the contribution from capacitive ion storage diminishes, while diffusion-controlled charge storage becomes more dominant[9]. Ion diffusion

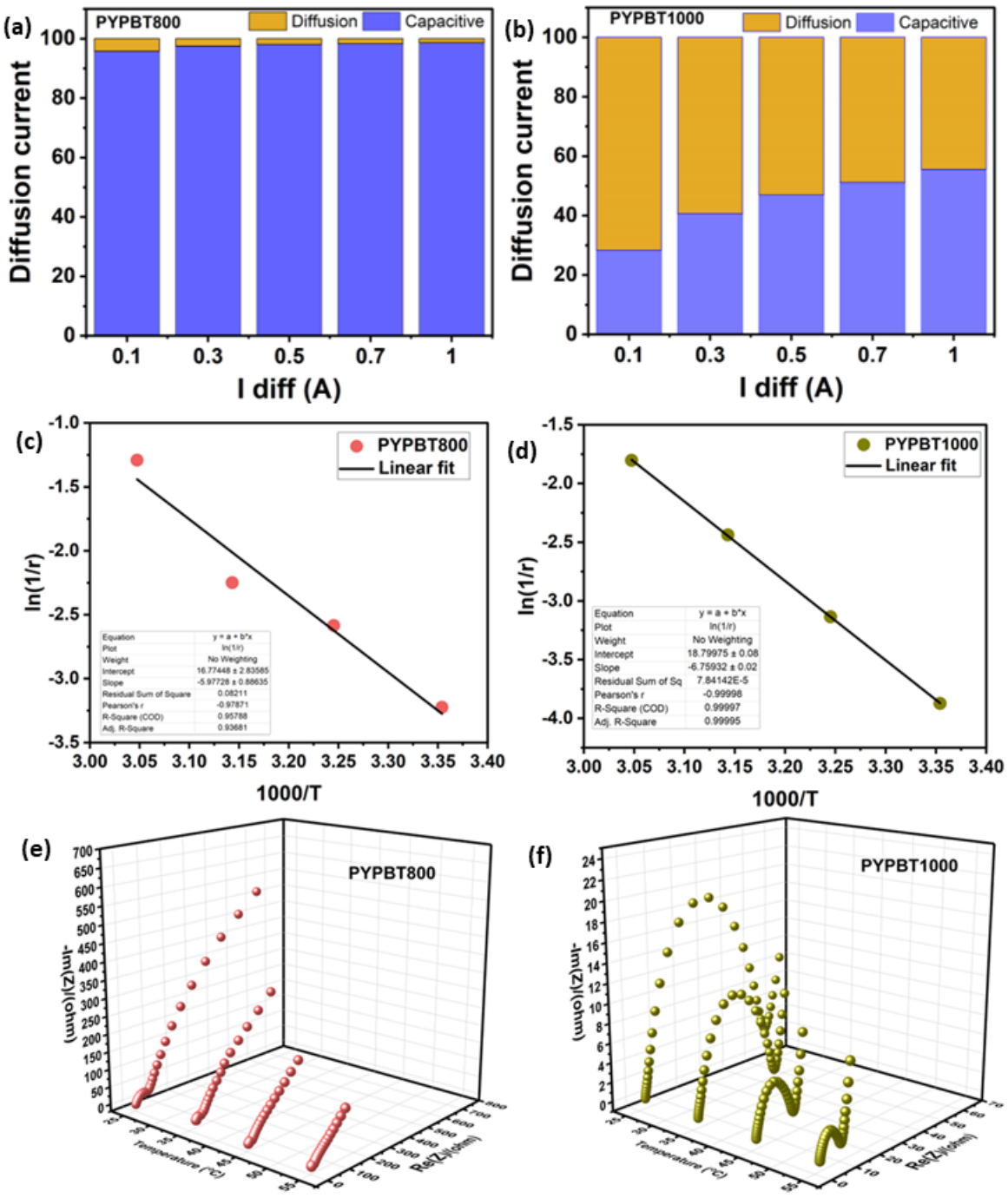

***Figure 37**: (a) Contribution of diffusion and capacitive based charge storage in PYPBT800 and PYPBT1000 based anodic half cell (c, d) ln(1/r) vs 1000/T plot for PYBT800 and PYPBT1000 (e, f) EIS plots at various temperatures for PYPBT800 and PYPBT1000 respectively*

typically involves several sequential steps: (1) diffusion of solvated ions through the electrolyte, (2) desolvation, where the solvation shell is stripped from the ions, (3)

diffusion of de-solvated ions across the SEI (4) electron transport within the anode material and across the anode–current collector interface, and (5) intercalation of de-solvated ions into the graphitic layers, primarily via edge planes. Among these, desolvation at the electrode–electrolyte interface is considered the most energy-intensive step. To evaluate this process, Electrochemical Impedance Spectroscopy (EIS) is conducted at various temperatures to determine the charge transfer resistance (R_{ct}). The temperature dependence of R_{ct} is then analysed using the Arrhenius equation, allowing for the calculation of the activation energy associated with ion desolvation and charge transfer[18].

$$\frac{1}{R_{ct}} = A exp\left(-\frac{E_a}{RT}\right) \quad \text{.....(3)}$$

R represents gas constant, A represents Arrhenius factor and R_{ct} is charge-transfer resistance, T represents absolute temperature (in Kelvin), Ea is activation energy for the charge transfer process[18]. This equation highlights that as pyrolysis temperature increases, R_{ct} decreases facilitating facile charge transfer. The activation energy can be calculated by plotting $ln(1/R_{ct})$ vs $1/T$. The activation energy was observed to be 49.70 kJ/mol and 56.20 kJ/mol for PYPBT800 and PYPBT1000 respectively, indicating a lower activation energy for desolvation in case of PYPBT800 than PYPBT1000 (Fig. 37(e) (f)). The lower activation energy in case of PYPBT800 could be due to the morphological and elemental features of PYPBT800 that enabled facile de-solvation[19]. Following this, dynamic electrochemical impedance spectroscopy (DEIS) was conducted which showed typical profiles of a semicircle in the high frequency region followed by a straight line in the low frequency region[20]. The DEIS was conducted in the voltage range of 0.01V to 3.0V. Further, upon fitting the EIS, the charge-transfer resistance which is generally observed at high

frequencies was obtained in the potential range of 0.01V to 3.0V during sodiation to find insights into charge-transfer behavior under charging conditions. The charge

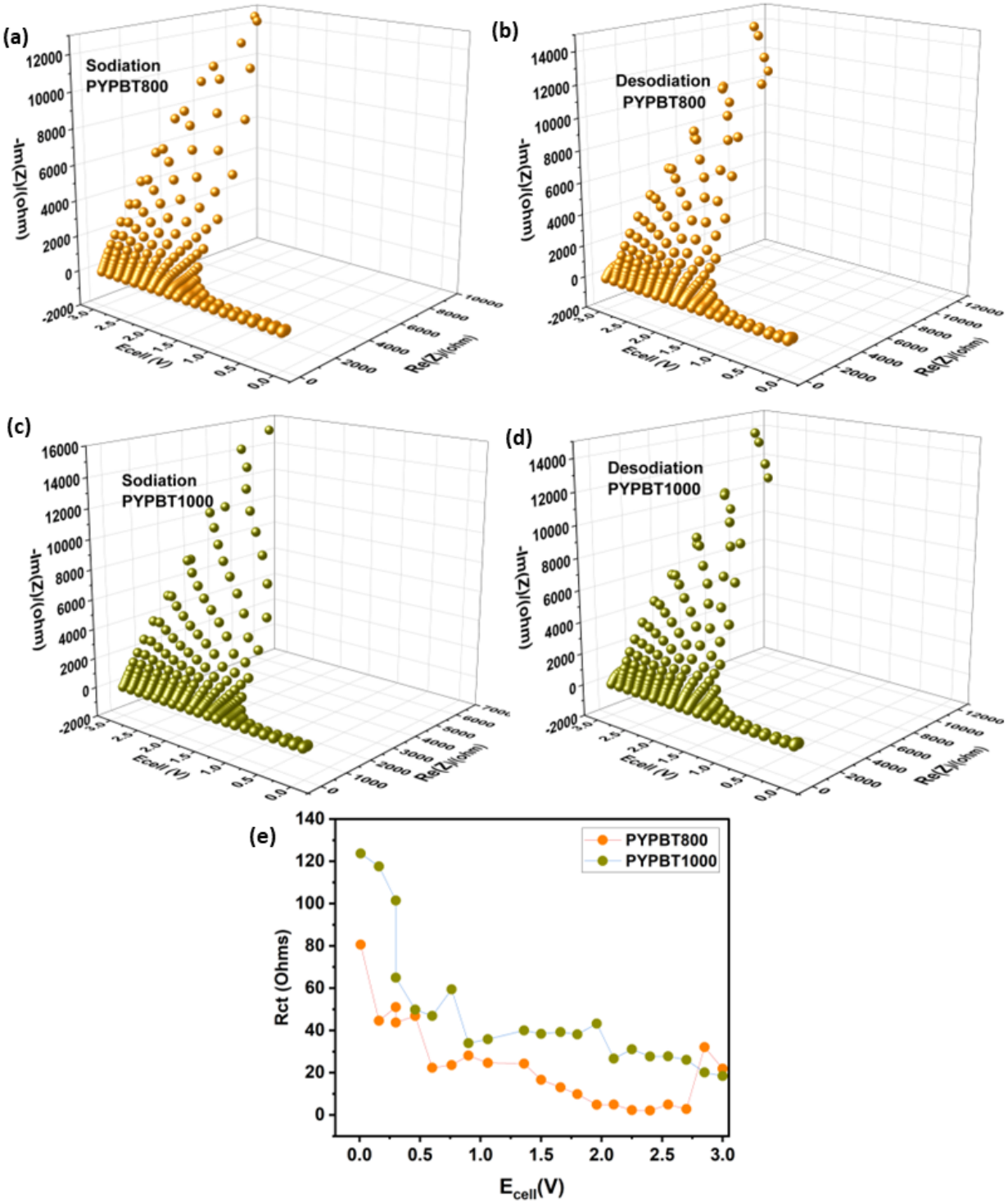

***Figure 38**: DEIS sodiation and desodiation plots of (a,b) PYPBT800 (c,d) PYPBT1000 respectively(e) comparison of charge-transfer resistance of PYPBT800 and PYPBT1000*

transfer resistance was observed to be consistently lower for PYPBT800 compared to PYPBT1000 as shown in Fig. 38, indicating that ion desolvation occurred more readily in PYPBT800. This enhanced desolvation ability can be attributed to the relatively more amorphous structure of PYPBT800, which possesses a higher density of defect sites. These defects likely provide a greater number of active sites, facilitating easier desolvation and more efficient ion transfer across the electrode–electrolyte interface[19]. Further, the cycled coin cells were decrimped in an Argon filled glove box. Generally, X-rays can penetrate up to 10 nm depth on the surface

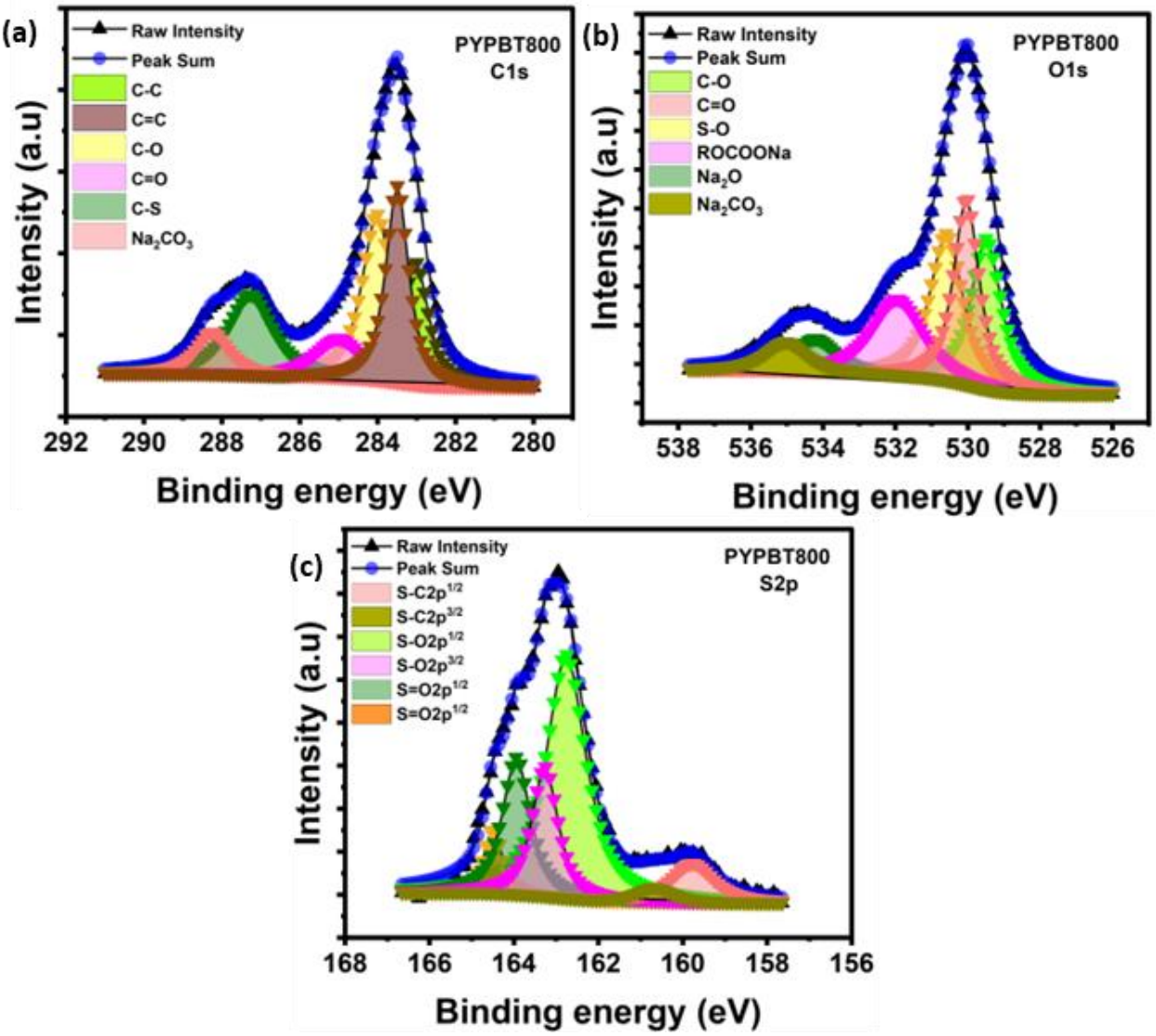

***Figure 39**: Deconvoluted XPS peaks for (a) C1s (b) O1s and (c) S2p for PYPBT800*

of the material. Hence SEI can be easily detected using the XPS. XPS was conducted for cycled anodes to understand the various components of SEI. The deconvolution of various elements such as C1s, O1s and S2p indicated various functional groups as shown in Fig. 39. The C1s spectrum upon deconvolution indicated peaks[21] at 284.0, 284.5, 285.0, 286.0, 288.3, 289.4 eV corresponding to C-C, C=C, C-O, C=O, C-S and Na_2CO_3. The O1s spectrum upon deconvolution indicated peaks[21] at 530.5, 531.0, 531.6, 532.9, 535.2, 536.0 corresponding to C-O, C=O, S-O, ROCOONa, Na_2O

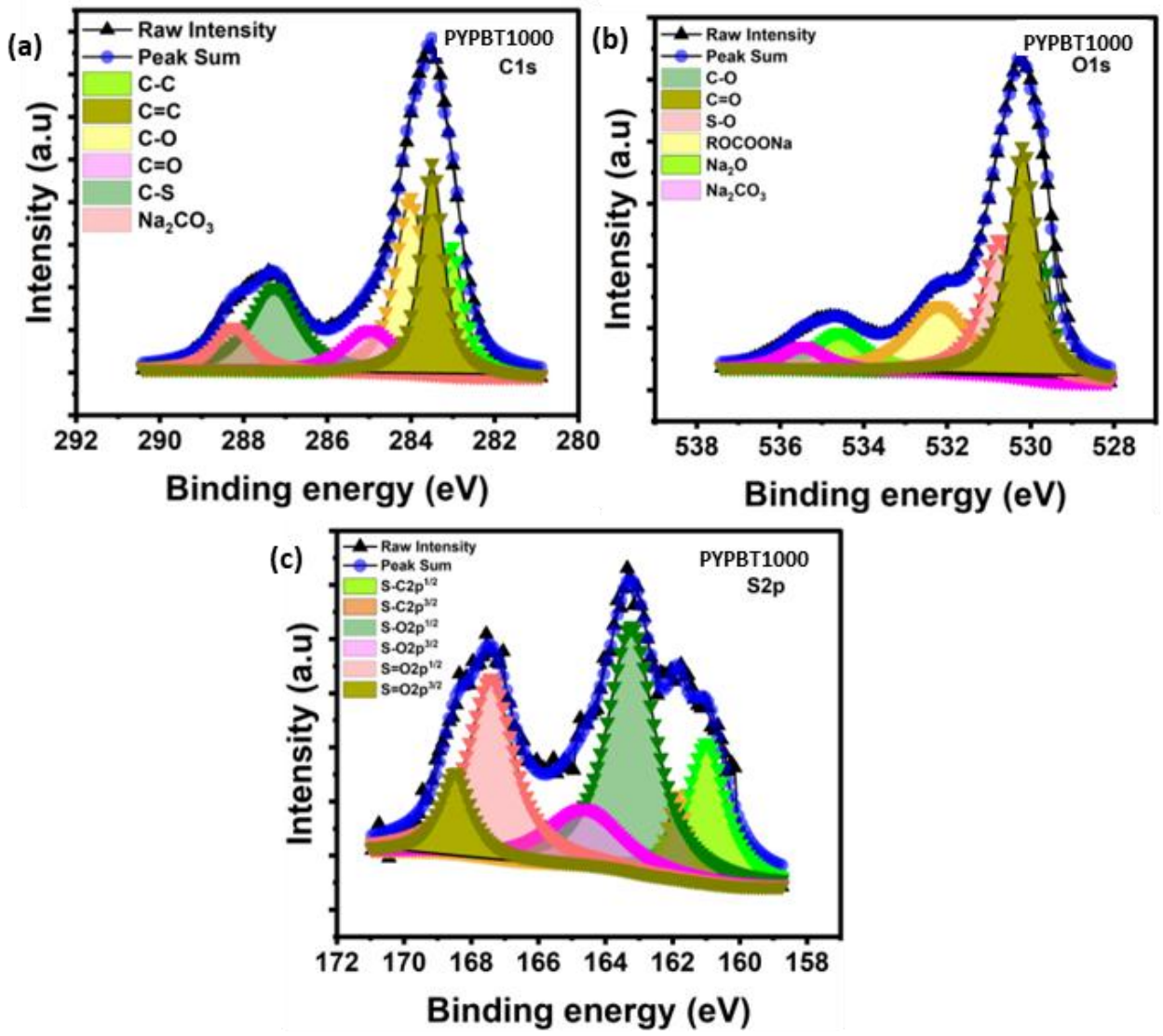

***Figure 40**: Deconvoluted XPS peaks for (a) C1s (b) O1s and (c) S2p for PYPBT1000*

and Na_2CO_3. The S2p XPS peak upon deconvolution indicated peaks[7] at 160.7, 161.6, 163.7, 164.2, 164.9, 165.5 eV corresponding to S-C2p$^{1/2}$, S-C2p$^{3/2}$, S-O2p$^{1/2}$, S-O2p$^{3/2}$, S=O2p$^{1/2}$ and S=O2p$^{3/2}$ respectively. Similarly, in case of PYPBT1000 based electrodes displayed in Fig. 40 the deconvolution was performed for each of the elements. Upon deconvolution, peaks[21] were observed at various positions such as 284.0, 284.5, 285.0, 285.9, 288.3, 289.3 eV corresponding to C-C, C=C, C-O, C=O, C-S, Na_2CO_3. The O1s spectrum upon deconvolution indicated peaks[22] at 530.8, 531.2, 531.7, 533.3, 535.6, 536.5 corresponding to C-O, C=O, S-O, ROCOONa, Na_2O and Na_2CO_3. The S2p XPS peak upon deconvolution indicated peaks[23] at 162.0, 163.0, 164.2, 165.6, 168.4, 169.5 eV corresponding to S-C2p$^{1/2}$, S-C2p$^{3/2}$, S-O2p$^{1/2}$, S-O2p$^{3/2}$, S=O2p$^{1/2}$ and S=O2p$^{3/2}$. These results collectively provide detailed insights into the composition of the SEI layers formed on both anodes.

3.6 Conclusions

In conclusion, this study presents a novel N, S co-doped hard carbon (HC) material derived from a bio-based poly(benzothiazole) polymer. The HCs were prepared via pyrolysis at two different temperatures—800°C and 1000°C. Electrochemical analysis demonstrated that PYPBT800 consistently outperformed PYPBT1000 in terms of desodiation capacity across all current densities during rate capability tests. In long-term cycling as well PYPBT800 maintained superior capacity retention delivering 160 mAh/g at 200 mA/g over extended cycling with nearly 100% retention, compared to 120 mAh/g and ~95% retention for PYPBT1000. At a high current density of 2000 mA/g, PYPBT800 still achieved a capacity of 90 mAh/g, significantly surpassing the 60 mAh/g observed for PYPBT1000 hence showing that PYPBT800 outperformed PYPBT1000 at both low and higher current densities. The enhanced performance of PYPBT800 is primarily attributed to its stronger

pseudocapacitive behaviour, which enables more effective surface adsorption of Na^+ ions. Moreover, the desolvation process was more efficient in PYPBT800, as evidenced by its lower desolvation energy barrier observed in activation energy studies. DEIS measurements further revealed a reduced charge transfer resistance

***Table 12**: Comparison of various bio derived carbons as anodes of sodium-ion batteries*

1	Discharge capacity of approximately 250 $mAhg^{-1}$ over 100 cycles at 30 mA/g	*Electrochemical Behavior of the Biomass Hard Carbon Derived from Waste Corncob as a Sodium-Ion Battery Anode*, Energy Fuels, 2024, 38, 8, 7389–7398
2	131.5 mAh/g after 500 cycles at 500 mAg^{-1} with a retention rate of 89.8%[1]	*Expanded biomass-derived hard carbon with ultra-stable performance for sodium-ion batteries*, Z. Zhu, F. Liang, Z. Zhou, X. Zeng, D. Wang, P. Dong, J. Zhao, S. Sun, Y. Zhang and X. Li,J. Mater. Chem. A, 2018,**6**, 1513-1522
3	At 100 mAg^{-1} the anode maintained a capacity of 330 $mAhg^{-1}$ after 450 cycles	*Research Progress and Commercialization of Biologically Derived Hard Carbon Anode Materials for Sodium-Ion Batteries,* Zeng Zeng, Yuanyin Mao, Zhihua Hu, Kai Chen, Qingke Huang, Yang Song, Zhenguo Wu, Pan Zhang, Ting Cheng, Xiadong Guo, Ind. Eng. Chem. Res. 2023, 62, 38, 15343–15359
4	Evaluated at 1000 mAg^{-1} delivered 241.8 $mAhg^{-1}$ with a 87.2% capacity retention for 2000 cycles	*Sustainable and scalable fabrication of high-performance hard carbon anode for Na-ion battery*, Yang Chen, Feng Li, Zhenyu Guo, Ziqing Song, Yueying Lin, Wei Lin, Lituo Zheng, Zhigao Huang, Zhensheng Hong, Maia-Magdalena Titirici, Journal of Power Sources, 557, 2023, 232534
5	20 mAh/g at 1000 mAg^{-1} after 1000 cycles with capacity retention of 97%	*Vine Shoots-Derived Hard Carbons as Anodes for Sodium-Ion Batteries: Role of Annealing Temperature in Regulating Their Structure and Morphology*, Darío Alvira, Daniel Antorán, Mariano Vidal, Victor Sebastian,and Joan J. Manyà, Batteries & Supercaps, 2023, 6, e202300233
6	250 mAh/g at 37.2 mA/g for 500 cycles with 0.047%/cycle average capacity loss	*Hard carbon derived from cellulose as anode for sodium ion batteries: Dependence of electrochemical properties on structure,* V. Simone, A. Boulineau, A. de Geyer, D. Rouchon, L. Simonin, S. Martinet, Journal of Energy Chemistry, 25, 2016, 761-768

for PYPBT800, indicating faster Na^+ ion transport across the SEI. This can be linked to the material's morphological features—namely, a higher density of defect sites and greater incorporation of nitrogen and sulphur—which facilitate improved ion and electron transport. Collectively, these properties make PYPBT800 a promising candidate for high-performance, fast-charging anodes in sodium-ion batteries. Compared to previously reported bio-based hard carbons as shown in Table 12, this study demonstrates a superior performance of bio-based polymer derived hard carbon derived from bio-based poly(benzothiazole) as an anode material for sodium-ion batteries.

References

1 N. Yabuuchi, K. Kubota, M. Dahbi and S. Komaba, *Chem Rev*, 2014, **114**, 11636–11682.

2 M. He, S. Liu, J. Wu and J. Zhu, *Progress in Solid State Chemistry*, 2024, **74**, 100452.

3 G. Yasin, S. Ibraheem, S. Ibrahim, A. Kumar, M. A. Mushtaq and R. Pathak, *Advanced Nanomaterials and Their Applications in Renewable Energy*, 2022, 251–272.

4 S. Komaba, W. Murata, T. Ishikawa, N. Yabuuchi, T. Ozeki, T. Nakayama, A. Ogata, K. Gotoh and K. Fujiwara, 2011, preprint, DOI: 10.1002/adfm.201100854.

5 A. Meintz, J. Zhang, R. Vijayagopal, C. Kreutzer, S. Ahmed, I. Bloom, A. Burnham, R. B. Carlson, F. Dias, E. J. Dufek, J. Francfort, K. Hardy, A. N. Jansen, M. Keyser, A. Markel, C. Michelbacher, M. Mohanpurkar, A. Pesaran,

D. Scoffield, M. Shirk, T. Stephens and T. Tanim, *J Power Sources*, 2017, **367**, 216–227.

6 H. Wang, Y. Shao, S. Mei, Y. Lu, M. Zhang, J. K. Sun, K. Matyjaszewski, M. Antonietti and J. Yuan, *Chem Rev*, 2020, **120**, 9363–9419.

7 H. Wan, X. Ju, T. He, T. Chen, Y. Zhou, C. Zhang, J. Wang, Y. Xu, B. Yao, W. Zhuang and X. Du, *J Alloys Compd*, 2021, **863**, 158078.

8 Y. Imai, I. Taoka, K. Uno and Y. Iwakura, *Die Makromolekulare Chemie*, 1965, **83**, 167–178.

9 K. Kubota, S. Shimadzu, N. Yabuuchi, S. Tominaka, S. Shiraishi, M. Abreu-Sepulveda, A. Manivannan, K. Gotoh, M. Fukunishi, M. Dahbi and S. Komaba, *Cite This: Chem. Mater*, 2020, **32**, 2961–2977.

10 S. Punyasloka, K. S. Patnaik, K. Higashimine and N. Matsumi, *Electrochim Acta*, 2025, **513**, 145578.

11 Z. Li, W. Cui, Q. Wu, X. Zhu, Y. Wei, W. Liu, N. Wang, Z. A. Wang, B. Liu and L. Gan, *Journal of Physical Chemistry C*, DOI:10.1021/ACS.JPCC.4C05906/ASSET/IMAGES/LARGE/JP4C05906_0005.JPEG.

12 H. Liu, M. Jia, N. Sun, B. Cao, R. Chen, Q. Zhu, F. Wu, N. Qiao and B. Xu, DOI:10.1021/acsami.5b06898.

13 K. S. Patnaik, B. S. Mantripragada, R. Badam, K. Higashimine, X. Zhong, T. Kaneko and N. Matsumi, *Nanoscale Adv*, 2024, **6**, 5181–5192.

14 B. Srimitra Mantripragada, K. Sumala Patnaik, K. Higashimine, R. Badam and N. Matsumi, *Electrochem commun*, 2023, **157**, 107616.

15 K. Xu, *J Power Sources*, 2023, **559**, 232652.

16 S. N. Mishra, S. Punyasloka, B. S. Mantripragada, A. Pradhan and N. Matsumi, *ACS Appl Energy Mater*, 2023, **6**, 11954–11962.

17 K. S. Patnaik, R. Badam, Y. Peng, K. Higashimine, T. Kaneko and N. Matsumi, *Chemical Communications*, 2021, **57**, 13704–13707.

18 A. Pradhan, R. Badam, R. Miyairi, N. Takamori and N. Matsumi, *ACS Mater Lett*, 2023, **5**, 413–420.

19 B. S. Mantripragada, M. K. S. Patnaik, K. Higashimine, R. Badam and N. Matsumi, *Batter Supercaps*, 2024, **7**, e202300515.

20 T. P. Jayakumar, R. Badam and N. Matsumi, *ACS Appl Energy Mater*, 2020, **3**, 3337–3346.

21 A. Patra and N. Matsumi, *ACS Appl Energy Mater*, DOI:10.1021/acsaem.3c02137.

22 R. Nandan, N. Takamori, K. Higashimine, R. Badam and N. Matsumi, *J Mater Chem A Mater*, 2022, **10**, 5230–5243.

23 T. Wu, M. Jing, L. Yang, G. Zou, H. Hou, Y. Zhang, Y. Zhang, X. Cao, X. Ji, T. Wu, M. Jing, L. Yang, G. Zou, H. Hou, Y. Zhang, X. Ji and X. Cao, *Adv Energy Mater*, 2019, **9**, 1803478.

4. Conclusions

Chapter 1

Chapter 1 provides a general introduction to the various types of energy storage systems. Energy storage devices have become increasingly important in addressing today's rising energy demands. With growing concerns about climate change and the depletion of fossil fuel resources, renewable energy sources like wind and solar are gaining significant attention. However, the intermittent nature of these sources—due to seasonal and weather-related variations—means they cannot provide a constant power supply. Therefore, energy storage systems are essential, as they enable the storage of excess energy when production is high and ensure a reliable energy supply when generation is low. This chapter explores various types of electrochemical energy storage devices, including fuel cells, capacitors, supercapacitors, and batteries. It begins with an overview of the key components of fuel cells, followed by a discussion on the distinctive features of different types such as polymer electrolyte membrane fuel cells, alkaline fuel cells, solid oxide fuel cells, phosphoric acid fuel cells, and molten carbonate fuel cells. Subsequently, the chapter delves into capacitors, explaining their structure and operating mechanisms in detail. Subsequently, a brief introduction to supercapacitors is presented, accompanied by detailed discussions on electric double-layer capacitors, pseudocapacitors, and hybrid capacitors. Amongst the various electrochemical energy storage devices, LIBs currently dominate the commercial market due to their lightweight nature, high energy density and long cycle life as well as the possibility of fast charging that can help in electric vehicles charging. Although LIBs are the most widely used storage technology today, the limited availability of lithium

resources has prompted growing research interest in sodium-ion batteries (SIBs) as a sustainable alternative. The chapter discusses the working mechanism and major components of LIBs, including the cathode, anode, separator, and electrolyte, with special emphasis on anode materials followed by outlines on the working principles and components of SIBs, again focusing on anode materials. Various types of anodes—such as conversion-type, alloy-type, and intercalation-type—are examined. The discussion begins with the staging mechanism of lithiation in graphite, followed by the limitations of graphite during fast charging in LIBs and its unsuitability as an anode in SIBs. Hard carbon is then introduced as a promising anode material for LIBs, offering morphological advantages that support fast charging. Finally, the potential of hard carbon for SIBs is discussed, highlighting its superior sodium storage capacity and structural stability.

Chapter 2

Chapter 2 delves into a relatively less explored area i.e nitrogen and oxygen dual-doped carbons derived from bio-based copolymers, specifically poly(benzimidazole-co-amide). It begins by emphasizing the growing need for fast-charging anodes, highlighting heteroatom-doped hard carbons as promising candidates due to their potential to enhance charge transport and surface reactivity. The synthesis of PYPBIPA based anodes was presented followed by characterization using various techniques such as XRD, HRTEM, Raman Spectroscopy, X-ray photoelectron spectroscopy. Subsequently, the electrochemical performance of the PYPBIPA-based anodes was evaluated using CR2025-type coin cells, with detailed results and discussions on rate capability and long-term cycling behavior. This was followed by an analysis of lithium-ion storage mechanisms and the associated

kinetics within the system. X-ray photoelectron spectroscopy (XPS) of the cycled anodes further revealed the composition of the solid electrolyte interphase (SEI). The chapter concludes with a summary highlighting how the morphological and elemental characteristics of the PYPBIPA-derived anodes influence their overall electrochemical performance.

Chapter 3

Chapter 3 focuses on the design and application of a novel nitrogen and sulfur (N, S) co-doped hard carbon material as an anode for sodium-ion batteries (SIBs). The chapter begins by emphasizing the increasing need for SIBs as a viable alternative to commercially dominant lithium-ion batteries (LIBs), particularly in light of lithium resource limitations and the push for more sustainable energy storage solutions. It details the development of the N,S co-doped hard carbon, synthesized from a single polymer precursor—polybenzothiazole. To examine the influence of carbonization temperature on the morphology and electrochemical behavior of the anode material, two variants were prepared: PYPBT800 and PYPBT1000. The synthesis and electrode fabrication procedures for both materials are described, followed by their structural and compositional characterization using X-ray diffraction (XRD), Raman spectroscopy, and X-ray photoelectron spectroscopy (XPS). Subsequently, the electrochemical performance of the materials in SIBs is evaluated through techniques such as cyclic voltammetry (CV), electrochemical impedance spectroscopy (EIS), and galvanostatic charge–discharge testing. Detailed rate capability and long-term cycling data are presented, along with an investigation of sodium-ion storage kinetics using power-law analysis. The findings show that as pyrolysis temperature increases, resulting in lower heteroatom content and higher

crystallinity, the capacitive contribution to sodium storage decreases, while diffusion-controlled mechanisms become more dominant. Further insights into charge transfer behavior at the solid electrolyte interphase (SEI) are provided through activation energy measurements and dynamic electrochemical impedance spectroscopy (DEIS). The chapter concludes with XPS analysis of the SEI layers formed on decrimped anodes, offering a comparative view of interfacial composition for both PYPBT800 and PYPBT1000.

Future Scope

Heteroatom-doped hard carbons (HCs) derived from bio-based polymers have shown significant promise as efficient anode materials for both LIBs) and sodium-ion batteries SIBs, as demonstrated in this thesis. While various carbon-based anodes have been extensively explored in the past—and hard carbons have even been tested for commercial use, their unique properties have not received sufficient attention in the context of enabling fast-charging capabilities. The inherently disordered structure of hard carbons offers multiple diffusion pathways and a high density of active sites, both of which facilitate rapid ion transport and enhanced ion storage. Moreover, the incorporation of heteroatoms into hard carbon structures introduces additional functionalities that can further improve performance. Heteroatom doping, particularly with electronegative elements, can expand the interlayer spacing, enhance electrical conductivity, and contribute to pseudocapacitive charge storage, thereby improving overall electrochemical behavior. When such HCs are synthesized from bio-based polymers, the materials benefit not only from these structural and electrochemical advantages but also from enhanced environmental sustainability. Bio-based polymers sourced from

renewable precursors make the entire process eco-friendlier and more scalable. Given these advantages, heteroatom-doped hard carbons derived from bio-based polymers represent a highly promising area of research, especially for developing next-generation, fast-charging anodes for future batteries as well as other energy storage devices such as supercapacitors.

Publications and conferences attended

1. *(**Research article**)* Extremely fast charging lithium-ion battery using bio-based polymer-derived heavily nitrogen doped carbon, *K. Patnaik, R. Badam, Y. Peng, K. Higashimine, T. Kaneko, N. Matsumi, Chem. Commun., 2021, 57, 13704-1370*
2. *(**Research Article**)* Bio-based poly(benzimidazole-co-amide)-derived N, O co-doped carbons as fast-charging anodes for lithium-ion batteries*, Kottisa Sumala Patnaik, Bharat Srimitra Mantripragada, Rajashekar Badam, Koichi Higashimine, Xianzhu Zhong, Tatsuo Kaneko and Noriyoshi Matsumi, Nanoscale Adv., 2024, 6, 5181*
3. *(**Feature review article**)* Advancing lithium-ion battery performance with heteroatom-based anode architectures for fast charging and high capacity*, Kottisa Sumala Patnaik, Bharat Srimitra Mantripragada, Saibrata Punyasloka and Noriyoshi Matsumi, Chem. Commun., 2025,61, 1282-1302*
4. *(**Research article**)* Energy efficient and fast charging nitrogen doped carbon anodes derived from BIAN-melamine based porous organic polymer for lithium-ion batteries, *Mantripragada, B. S., Patnaik K. S., Higashimine, K., Badam, R., & Matsumi, N. Batteries & Supercaps, Chemistry Europe, 7(4), 515-527, 2023*.
5. *(**Research article**)* POP based nitrogen containing anodic materials for high capacity and fast Charge-Discharge applications in LIB*. Mantripragada, B. S.,*

Patnaik, K. S., Higashimine, K., Badam, R., & Matsumi, N, Electrochemistry Communications, Elsevier, 157, 107616-628, 2023

6. *(**Research article**)* $CoFe_2O_4$ Nanoparticles on Bio-Based Polymer Derived Nitrogen Doped Carbon as Bifunctional Electrocatalyst for Li-Air Battery, *Pirapath Arkasalerks, Amarshi Patra, Kottisa Sumala Patnaik, Koichi Higashimine and Noriyoshi Matsumi, 2024, J. Electrochem. Soc., 171 080538*
7. *(**Research article**)* Exploiting Innate Porosity and Surface Area of Conjugated Porous Polymer to Derive N, S Co-doped Hierarchical Micro/Mesoporous Carbon with Improved Lithium/Sodium Ion Storage, *Saibrata Punyasloka, Kottisa Sumala Patnaik, Koichi Higashimine, Noriyoshi Matsumi, Electrochemica Acta, 2025, 145578*
8. *(**Textbook Chapter**)* Chapter 13- Nano-engineering strategies for high-performance batteries and capacitors, *Bharat Srimitra Mantripragada, Sumala Patnaik Kottisa, Amarshi Patra, Saibrata Punyasloka, Noriyoshi Matsumi, Elsevier, 2025, 311-337.*
9. *(**Research article**)* Pectic Acid-Derived Biobased Poly(ionic liquid) Binder for High-Performance Lithium-Ion Battery Anodes*, Ze Li, Zhaohan Liu, Amarshi Patra, Bharat Srimitra Mantripragada, Sameer Nirupam Mishra, Kottisa Sumala Patnaik, Noriyoshi Matsumi ACS Appl. Polym. Mater. 2025, 7, 11, 7589–7599*

Conferences attended:

1. Kottisa Sumala Patnaik, Yueying Peng, Rajashekar Badam, Tatsuo Kaneko, Noriyoshi Matsumi, Bio-derived Lithium-ion Battery Anode Material for Fast Charging and Long-cycle Life, 239th ECS Meeting, Chicago, May 2021 (Oral presentation)

2. Kottisa Sumala Patnaik, Rajashekar Badam, Yueying Peng, Tatsuo Kaneko, Noriyoshi Matsumi, Bio Based Polymer Derived Anode Material for Fast Charging and Long Cycle Life of Lithium-ion Battery, 70th Annual Meeting of the Society of Polymer Science, Japan, May 2021 (Poster Presentation).
3. Kottisa Sumala Patnaik, Yueying Peng, Rajashekar Badam, Tatsuo Kaneko, Noriyoshi Matsumi, Fast Charging Lithium-ion Batteries using Bio-based Polymer Derived Hard Carbon, 70th Symposium on Macromolecules, Tokyo, Japan, September 2021 (Poster Presentation).
4. Kottisa Sumala Patnaik, Yueying Peng, Rajashekar Badam, Tatsuo Kaneko, Noriyoshi Matsumi, Extreme Fast Charging Lithium-ion Battery Using Bio-Based Polymer Derived Heavily Nitrogen Doped Carbon, 62nd Battery Symposium, Yokohama, Japan, December 2021 (Oral Presentation).
5. Kottisa Sumala Patnaik, Yueying Peng, Rajashekar Badam, Tatsuo Kaneko, Noriyoshi Matsumi, Fast charging lithium-ion full cell using polymer derived heavily nitrogen doped carbon, 71st Annual Meeting of the Society of Polymer Science, Japan, May 2022 (Poster presentation).
6. Kottisa Sumala Patnaik, Yueying Peng, Rajashekar Badam, Tatsuo Kaneko, Noriyoshi Matsumi, Extremely Fast Charging Lithium-ion Battery Using Bio-Based Polymer Derived Heavily Nitrogen-Doped Carbon, 21st International Meeting on Lithium Batteries, Australia, May 2022 (Poster presentation)
7. Kottisa Sumala Patnaik, Yueying Peng, Rajashekar Badam, Tatsuo Kaneko, Noriyoshi Matsumi, Pyrolysis temperature dependency on fast charge-discharge capability of PBI-based Li-ion secondary batteries, 71st Symposium on Macromolecules, Japan, September 2022 (Oral Presentation).

8. Kottisa Sumala Patnaik, Rajashekar Badam, Yueying Peng, Tatsuo Kaneko, Noriyoshi Matsumi, Fast Charging Li-ion full cell using a bio-based anode material, 63rd Battery Symposium, Kyoto, Japan, December 2022 (Oral Presentation)
9. Kottisa Sumala Patnaik, Bharat Srimitra, Rajashekar Badam, Tatsuo Kaneko and Noriyoshi Matsumi, Preparation of Anodic Active Materials Suitable for High-Rate Charge-Discharge by calcination of Poly(benzimidazole/amide) Copolymers, 72nd Annual Meeting of the Society of Polymer Science, Japan, May 2023 (Poster Presentation)
10. Kottisa Sumala Patnaik, Bharat Srimitra Mantripragada, Rajashekar Badam, Tatsuo Kaneko, Noriyoshi Matsumi, 6th Clean Energy and Technology Conference, Malaysia, June 2023 (Oral Presentation)
11. Kottisa Sumala Patnaik, Bharat Srimitra, Rajashekar Badam, Tatsuo Kaneko and Noriyoshi Matsumi, Bio-based Poly(benzimidazole-co-polyamide) Derived Carbon Material as Fast Charging Anode for Lithium-ion Batteries, 73rd Symposium on Macromolecules, Japan, September 2023 (Oral presentation)
12. Kottisa Sumala Patnaik, Bharat Srimitra, Rajashekar Badam, Tatsuo Kaneko and Noriyoshi Matsumi, Optimising N and doping O contents for achieving fast charging in lithium-ion batteries, 64th Battery Symposium, Japan, November 2023 (Oral Presentation)
13. Kottisa Sumala Patnaik, Kottisa Sumala Patnaik, Yuuki Tanaka, Kenji Takada, Tatsuo Kaneko and Noriyoshi Matsumi, Fast charging performance of Li-ion secondary batteries fabricated using caffeic acid-based polymer binder and bio-based hard carbon, 73rd Annual Meeting of the Society of Polymer Science, Japan, June 2024 (Poster Presentation)

14. Kottisa Sumala Patnaik, Kottisa Sumala Patnaik, Yuuki Tanaka, Kenji Takada, Tatsuo Kaneko and Noriyoshi Matsumi, Bio-based Dimerized Caffeic Acid-Based Binder for Enhancing the Fast-Charging Performance in Secondary Ion Batteries, 74th Symposium on Macromolecules, Japan, September 2024 (Poster Presentation)
15. Kottisa Sumala Patnaik, Anusha Pradhan, Yuuki Tanaka, Kenji Takada, Tatsuo Kaneko and Noriyoshi Matsumi, Bio-Derived Boronated Dimerized Caffeic Acid Polymer: A Water-Soluble Binder for Carbonaceous Battery Anodes, 65th Battery Symposium, Kyoto, Japan, November 2024 (Oral Presentation)

Awards and fellowships received:

1. Best Poster Award in 70th Annual Meeting of the Society of Polymer Science, Japan, May 2021
2. Best presenter award in 6th Clean Energy and Technology Conference, Malaysia, June 2023
3. Excellent student Award in Masters of Materials Science academic session 2020-2022
4. MEXT (Ministry of Education, Culture, Sports, Science and Technology) fellowship from October 2022 to April 2025
5. Fellowship received in DC2 category of Japan Society for Promotion of Sciences from April 2025 年度受付番号 202517022